Univerzita Karlova v Praze
Přírodovědecká fakulta

Studijní program a obor: Geologie

Bc. Tereza Jandová

Differentiation and crystallization of evolved granitic melts, the Říčany pluton, central Bohemian Massif

Diferenciace a krystalizace vyvinutých granitových tavenin, říčanský pluton, Český masiv

Diplomová práce

Vedoucí závěrečné práce:
doc. Mgr. David Dolejš, Ph.D.
Konzultant:
RNDr. Jakub Trubač

Praha, 2013

Prohlášení:

Prohlašuji, že jsem závěrečnou práci zpracovala samostatně a že jsem uvedla všechny použité informační zdroje a literaturu. Tato práce ani její podstatná část nebyla předložena k získání jiného nebo stejného akademického titulu.

V Praze, 08.08.2013

Bc. Tereza Jandová

Abstract

Evolved silicic rocks display a variety of igneous textures, which can provide important information on crystallization kinetics and rheology in natural magma chambers. Individual kinetic effects such as diffusion rate, nucleation rate, growth rate and post-solidification modifications are likely to be reflected in the modal and textural appearance of the resulting rock. This work focuses on characterization and interpretation of solidification textures in a 600 m wide and 5 km long body of highly evolved, boron-rich aplites and pegmatites at the southern endocontact of the Říčany granite pluton (Central Bohemian Plutonic Complex). This rock suite is associated with biotite Říčany granite, hosting microgranite and aplite dyke swarm, and it is built up by massive tourmaline aplites, layered aplites with tourmaline-rich or locally garnet-rich bands, pegmatite pockets, pegmatite layers with unidirectional solidification textures (comb layers), megacryst zones (analogous to stockscheider), and late pegmatite dykes discordant to layering. Textural as well as modal variations are usually sharp and observable megascopically as well as on the microscale. All aplites and pegmatites usually contain similar proportions of quartz, albite-rich plagioclase, K-feldspar, various proportions of tourmaline (up to ~15 vol. %), muscovite, garnet, and accessory biotite, cassiterite, rutile, zircon, apatite, columbite-tantalite, ilmenite, xenotime, monazite, beryl and/or topaz. The anorthite component in plagioclase, *mg#* (molar $Mg/[Mg+Fe^{2+}]$) in tourmaline, muscovite or biotite (when present) decreases, whereas *mn#* (molar $Mn/[Mn+Fe^{2+}]$) in garnet and fluorine abundance in various hydrous minerals increases with progressive differentiation, from massive aplites and their megacryst zones through layered aplites and pegmatite layers to pegmatite dykes, which may represent products of *in-situ* fractionation. The aplites and pegmatites are classified as syenogranites or alkali feldspar granites, they are high-K calc-alkaline and strongly peraluminous (alumina saturation index = 1.43-1.68), and enriched in Si, Na, B, Be, Sn, W, Ta and Pb relative to the Říčany granite. They have flat REE-patterns with a pronounced negative Eu-anomaly (Eu/Eu^{*} = 0.04-0.39). The H_2O- and B-rich aplite-pegmatite melt is inferred to have evolved during solidification of the Říčany pluton or its parental magma chamber. Textures of the aplite-pegmatite suite indicate rapid crystallization from an increasingly viscous and undercooled melt. An evolved boundary layer developed ahead of a dense solidification front due to the inhibited diffusion of components in the viscous melt and rapid crystallization rate. This allowed the layered aplites to crystallize by a mechanism known as diffusion-controlled oscillatory nucleation. Crystal-size variations arose due to accumulation of fluxes (e.g. B, H_2O) in the boundary-layer melt, which reduced the viscosity of the melt, enhanced the diffusion rate and inhibited nucleation locally, thus allowing large crystals to form by constitutional zone-refining.

České shrnutí

Magmatické textury, které se vyskytují ve vyvinutých granitických horninách, představují důležitý zdroj informací o krystalizační kinetice a reologii v magmatických krbech. Textury i modální složení výsledné horniny jsou odrazem kinetických efektů jako je rychlost difúze, nukleace, růstu krystalů a postsolidifikačních procesů. Tato práce se zabývá charakterizací a interpretací solidifikačních textur bórem bohatých aplitů a pegmatitů, které tvoří asi 600 m široké a 5 km dlouhé těleso v jižním endokontaktu říčanského granitového plutonu ve středočeském plutonickém komplexu. Toto těleso se skládá z masívních turmalinických aplitů, páskovaných aplitů s pásky bohatými turmalínem nebo granátem, pegmatitových kapes, pegmatitových vrstev s texturami dokazujícími jednosměrný růst, megakrystových zón a pozdních pegmatitových žil diskordantních k páskování. Přímou souvislost s pásem aplitů a pegmatitů mají četné mikrogranitové a aplitové žilky v říčanském plutonu. Texturní a modální variace jsou většinou ostře ohraničené a vyskytují se jak v makro-, tak i v mikroměřítku. Všechny aplity a pegmatity většinou obsahují podobný poměr křemene, albitem bohatého plagioklasu a K-živce, a mohou dále obsahovat turmalín (až ~15 obj. %), muskovit, granát a akcesoricky biotit, kasiterit, rutil, zirkon, apatit, kolumbit-tantalit, ilmenit, xenotim, monazit, beryl a/nebo topaz. Podíl anortitové složky v plagioklasu a *mg#* hodnota (molární $Mg/[Mg+Fe^{2+}]$) v turmalínu, muskovitu, nebo biotitu (pokud je přítomen) klesá, zatímco *mn#* hodnota (molární $Mn/[Mn+Fe^{2+}]$) v granátu a obsah fluoru v různých minerálech stoupá s postupující diferenciací, což je od masívních aplitů a megakrystových zón přes páskované aplity a pegmatitové vrstvy k diskordantním pegmatitovým žilám, které by mohly představovat produkt *in-situ* frakcionace. Aplity a pegmatity jsou klasifikovány jako syenogranity až alkalicko-živcové granity, mají vysokodraselnou vápenato-alkalickou povahu, jsou vysoce peraluminické (hliníkový saturační index, ASI = 1.43-1.68) a obohacené Si, Na, B, Be, Sn, W, Ta a Pb vzhledem k říčanskému granitu, mají ploché distribuce REE prvků a výraznou negativní europiovou anomálii (Eu/Eu^{*} = 0.04-0.39). Vodou a bórem bohatá aplito-pegmatitová tavenina se pravděpodobně vyvinula během solidifikace říčanského plutonu, nebo jeho mateřského magmatického krbu. Textury aplitů a pegmatitů indikují rychlou krystalizaci z velmi viskózní a podchlazené taveniny. Díky zpomalené difuzi prvků ve viskózní tavenině a velké růstové rychlosti se před hustou solidifikační frontou vyvinula obohacená vrstva taveniny, což dalo vzniknout páskovaným aplitům mechanismem difuzně-kontrolované oscilační nukleace. Variace ve velikosti krystalů vznikly díky akumulaci volatilií (např. B, H_2O) v obohacené vrstvě taveniny před solidifikační frontou, což mělo za následek snížení viskozity taveniny a nukleační hustoty, zrychlení difuze a tudíž zvětšení velikosti krystalů.

Table of Contents

1 Introduction

1.1 Nature and properties of silicic melts

Natural melts and magmas are molten polymerized silicates, whose short-range structure has profound effects on their physical and chemical properties, phase equilibria, volatile solubilities and element partitioning. It is useful to review some of these features before proceeding to the main discussion of equilibria and crystallization in highly evolved granitic and pegmatitic magmas.

1.1.1 Melt structure

Properties of silicate melts are closely related to their structure, which is mainly governed by composition, temperature and pressure. Silicate melts are of amorphous nature, but despite the lack of periodicity and long-range order, they have a characteristic short-range order, which obeys basic crystal-chemical rules. They may be viewed as mixtures of structural entities that, at least at a local scale, resemble those of crystalline phases existing at or near their liquidus (Mysen and Richet, 2005). These entities are expressed as so called Q^n structural units, where *n* is the number of bridging oxygen atoms (discussed later), that means that Q^0 are monomers, Q^1 dimers, Q^2 chains, Q^3 sheets and Q^4 are three-dimensional network units. Bond strength, bond angle, and the amount of network-formers and network-modifiers have the basic influence on the structure of the melt. Bond strength depends on the type of the bond and on the valence and coordination number of the ion as well. The type of bond is defined by electronegativity of the components and ionization potential in the case of metals. In the case of oxygen-metal bonds, for a given oxygen coordination number, the bond strength is positively correlated with the ionization potential of the metal cation and for a given metal cation, the bond strength decreases as the oxygen coordination number increases (Smyth and Bish, 1988). Bond strength is a systematic function of bond distance too – the shorter the bond, the greater is its strength (Pauling, 1960). Metal-oxygen bond distances are a positive function of the oxygen coordination number. In crystalline silicate structures, where the basic building block is the oxygen tetrahedron, bond length variation is accommodated by changes in intertetrahedral angle. Bond length is more sensitive to bond angle at high than at ambient pressure (Fig. 1.1). The greater flexibility of molten and glassy silicates compared with their crystalline equivalents (Levien et al., 1980; Seifert et al., 1983) may result from greater flexibility of the intertetrahedral, Si-O-Si, angle and, therefore, of the Si-O bond length (Seifert et al., 1983; Kubicki and Lasaga, 1987). Variations in intertetrahedral angles may also be driven by changes in the number of oxygen bridges between the tetrahedral (Soules, 1979; Furukawa et al., 1981). While the proportion of oxygen bridges decreases, the intertetrahedral angle becomes larger.

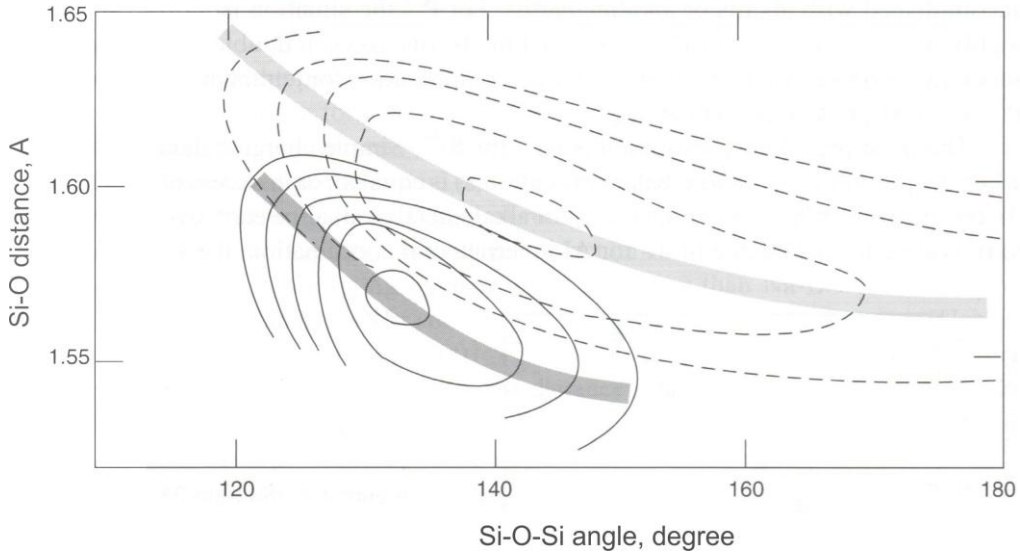

Fig. 1.1 Relationships between bond distance, Si-O, and intertetrahedral bond angle, Si-O-Si, calculated for $H_6Si_2O_7$ clusters at ambient pressure (dashed lines) and at 1 GPa (solid lines) (Meagher et al., 1980; Ross and Meagher, 1984).

The Si^{4+} ion in the SiO_4 tetrahedron may be replaced by other cations, which are referred to as network-formers. Bond lengths and bond angles (and therefore bond strength) depend not only on pressure and temperature but also on the nature of these tetrahedrally coordinated cations (T), network-formers. The most common network-formers are Al^{3+}, Fe^{3+}, B^{3+} and P^{5+}, but the substitution of these cations for Si^{4+} requires charge compensation *via* coupled substitution or close association with other cations to obtain a formal charge near 4+ at the tetrahedral site. Alkalies and alkali earths often play the role of "charge compensators". When there is an excess of alkali metal or alkaline earth over that required to provide a formal charge of 4+ for Al in tetrahedral coordination, the system is called peralkaline, when the proportion of alkali metal or alkali earth is exactly equal to that required to charge-compensate Al, the system is called subaluminous, and when the proportion of Al exceeds that of available cations for charge-compensation, the system is called peraluminous. The oxygen tetrahedra with the network-forming cations in the centre can be linked by bridging oxygen, or linked to different groups of oxygen polyhedra with a network-modifying cation *via* a nonbridging oxygen. Other cations in tetrahedral coordination, like P^{5+} and possibly B^{3+} and Ti^{4+}, likely form separate tetrahedral clusters. Alkali metals and alkaline earths also play the role of network-modifying cations, possibly together with Fe^{2+}. They are bonded to nonbridging oxygens, and these bonds are affected by the properties of the network-modifying cation and by the melt composition, because the proportion of the Q^n structural units changes with composition, and therefore the degree of polymerization. There is ordering of the network-modifying cations in mixed melts among energetically non-equivalent nonbridging oxygens. The most electronegative network-modifying cation tends to form

oxygen polyhedra with nonbridging oxygen in the most depolymerized from the coexisting Q^n structural units (Lee et al., 2002; Lee and Stebbins, 2003).

An important parameter, which can be used as a structural monitor at least at low pressures, and which is correlated with a variety of melt properties, is the NBO/T value (number of nonbridging oxygens, NBO, per tetrahedrally coordinated cation, T) and it can be calculated from melt composition. The T includes Si + Al + Fe^{3+} charge-compensated with alkalies and alkali earths and NBO = (2O – 4T), where O is oxygen (Mysen and Richet, 2005). It expresses the degree of polymerization of a silicate melt, like the Q^n units but the scale has an opposite sence (NBO/T = 4 are monomer units, NBO/T = 3 dimers, and so on).

1.1.2 Rheological properties and the role of volatiles in evolved granitic melts

Rheological properties of silicate liquids are mainly governed by composition of the liquid and temperature. As an example, melt viscosity decreases as temperature increases for a given composition, and it increases as silica content of the melt increases at a given temperature (e.g. Zhang and Jahanshahi, 1998; Giordano et al., 2008). Pressure dependence of viscosity is only significant over wide range of pressures (e.g. Whittington et al., 2009). The temperature dependence of viscosity was described by the Vogel-Fulcher-Tamman (VFT) equation (Vogel, 1921; Fulcher, 1925):

$$\log\eta = A + B/(T-C), \qquad (1\text{-}1)$$

where η is viscosity in Pa.s, T is temperature in Kelvins, A, B, and C are adjustable parameters, including the preexponential factor, pseudo-activation energy, and the VFT-temperature, respectively. The compositional controls on viscosity reside only in B and C (A is an unknown constant) (Giordano et al., 2008).

The composition dependence of the viscosity of silicate melts relates proportionally to the degree of melt polymerization, which can be quantified by the NBO/T or any similar chemical parameter (e.g. Mysen and Richet, 2005; Giordano et al., 2008). Granitic melts are nominally polymerized, due to their high silica content, with the low NBO/T values. The viscosity of evolved granitic melts is expected to be very high, because of their very high silica content and low liquidus temperatures. The viscosity of water-free peraluminous granite at 700 °C and 2-3 kbar is ~10^{12} Pa.s according to the model of Whittington et al. (2009), and this value is commonly considered to represent the onset of glass transition.

Addition of H_2O or other volatiles significantly reduces the melt viscosity to less than 10^6 Pa.s for a peraluminous granite at 700 °C, 2-3 kbar and 6 wt. % H_2O (Whittington et al., 2009), because they substantially depolymerize the melt structure. For example the addition of 1 wt. % B_2O_3 at temperatures corresponding to the crystallization of B-rich granitic and pegmatitic systems decreases the viscosity by two orders of magnitude (Dingwell et al., 1992). The effect of B_2O_3 on viscosity increases strongly with decreasing temperature and the strongest viscosity decrease is exhibited at low B_2O_3 concentrations.

The underlying principle for the viscosity decrease is the interaction of volatiles with silicate melt network. The H_2O dissolves in silicate melts in two forms – as molecular H_2O and as OH groups (first described by Scholze, 1956). The solubility of H_2O in silicate melts is mainly function of pressure (or water pressure, fugacity, fH_2O; Goranson, 1931; Tomlinson, 1956; Burnham and Jahns, 1962), and with increasing pressure increase the water solubility (for example up to ~6 wt. % H_2O can be dissolved in a granitic melt at 2 kbar, and up to ~9 wt. % H_2O can be dissolved in a granitic melt at 4 kbar at ~700-1100 °C according to the model of Zhang et al., 2007). The relative abundance of OH groups and molecular H_2O is predominantly function of the total water content of the melt (Stolper, 1982) (Fig. 1.2), but the proportion of water dissolved as molecular H_2O increases with increasing silica content (Silver et al., 1990) (Fig. 1.2), and *in-situ* experimental measurements indicate that the OH/H_2O ratio increases with increasing temperature (Fig. 1.3; Nowak and Behrens, 1995; Behrens and Nowak, 2003). This homogeneous speciation mechanism accounts for the contrast between the distinct, nonlinear *vs.* linear structure-property relationships that change at about 2 wt. % H_2O dissolved in the melt (nonlinear below 2 wt. % H_2O and linear over 2 wt. % H_2O). Interesting influence on the OH/H_2O ratio in the melt has the B_2O_3 content, which strongly increases the fraction of water dissolved as hydroxyl groups (Romano et al., 1995).

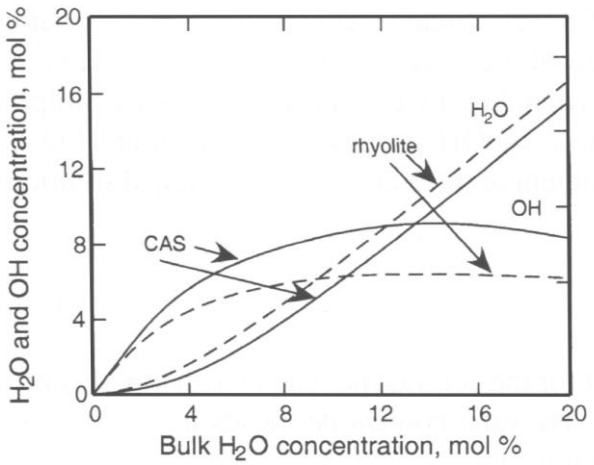

Fig. 1.2 Proportion of water dissolved as OH and as molecular H_2O in CaO-Al_2O_3-SiO_2 (CAS) glass and rhyolite glass (Newman et al., 1986; Silver et al., 1990).

As a consequence of hydroxyl formation in the melt structure, water has a depolymerizing effect on silicate melts because the oxygen bridges in a three-dimensionally interconnected network of SiO_2 are replaced by terminal OH groups (Moulson and Roberts, 1961):

$$Si\text{-}O\text{-}Si + H_2O \leftrightarrow Si\text{-}OH \mid HO\text{-}Si. \quad (1\text{-}2)$$

When a metal oxide is added into the system, the metal/silicon ratio affects the water solubility and, at a fixed metal/silicon ratio, the H_2O solubility is negatively correlated with the ionization potential (or ionic radius) of the alkali metal. This indicates that, in addition to Eq. (1-2), alkali metal-proton coupling becomes important. There is also a negative correlation between the water solubility and the Al_2O_3 content in the melt (e.g. Mysen, 2002). Thus, water solubility is a function of temperature, pressure, and a complex function of composition (Moore, 2008).

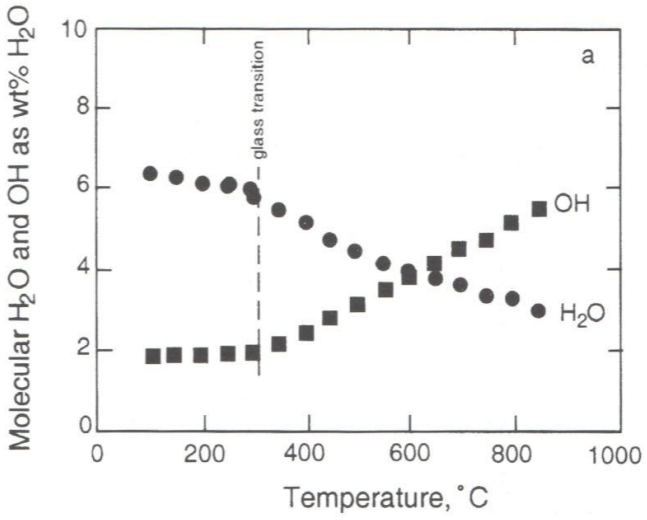

Fig. 1.3 Concentration of water as molecular H_2O and OH in $NaAlSi_3O_8$-$KAlSi_3O_8$-SiO_2 melt as a function of temperature (Nowak and Behrens, 1995).

1.2 Crystallization of highly evolved granitic melts

Solidification of a melt is governed by the relevant phase equilibria as well as kinetic effects. In highly evolved granitic melts the kinetic effects often play often an equally important role (London, 2008; Nabelek et al., 2010).

1.2.1 Phase equilibria

Phase equilibria including a melt, mineral phases and aqueous fluids are function of melt composition, temperature and pressure and other intensive variables such as fluid fugacities or redox conditions.

The minimum solidus temperature of a haplogranite system (Qz-Or-Ab) at 1 kbar and fluid-saturated conditions is close to 720 °C as is the minimum liquidus temperature at this pressure (Tuttle and Bowen, 1958). Decreasing content of water shifts the liquidus toward significantly higher temperatures; liquidus temperature of a water-free haplogranite system is ~970 and 1040 °C at 1 and 4 kbar, respectively (Holtz et al., 2001). By contrast, the solidus of a haplogranite melt toward lower temperatures (significant only at pressures ~2 kbar and lower - ~690 °C for a haplogranite melt at 2 kbar) (Holtz et al., 2001). The addition of B_2O_3 into the melt lowers the solidus as well as liquidus temperatures and increases the isobaric

solubility of H_2O in the melt. Under fluid-saturated conditions, the minimum solidus temperature of a haplogranite melt at 1 kbar is reduced down to ~600 °C (from 720 °C) upon addition of 4.5 wt. % B_2O_3 (Chorlton and Martin, 1978), and the minimum liquidus temperature of the same melt at 1 kbar is reduced down to ~640 °C (Pichavant, 1987). Similar reducing effects on the solidus and liquidus temperatures as well as isobaric solubility of H_2O in the melt like B_2O_3 have also F_2O and P_2O_5 (Dolejs and Baker, 2007; London et al., 1993) (the addition of 5 wt. % F to a haplogranitic, H_2O-saturated melt at 1 kbar reduces the liquidus temperature in the order of ~120 °C, and the addition of 2-4 wt. % F to the same melt reduces the solidus temperature down to 640 °C; Dolejs and Baker, 2007).

Crystallization and melting experiments were carried out at 4 kbar on tourmaline-muscovite leucogranite (73 wt. % SiO_2, 16 wt. % Al_2O_3, 4.6 wt. % Na_2O, 4.1 wt. % K_2O, 0.89 wt. % B_2O_3, and other components less than 1 wt. %) under variable H_2O concentration by Scaillet et al. (1995). The crystallization sequence of minerals remains roughly the same for various water contents, only the temperatures of the stability fields change. Plagioclase is the first liquidus phase up to ~8 wt. % H_2O in the melt, and it is replaced by biotite for ~8-9.5 wt. % H_2O in the melt, followed by tourmaline, and quartz with alkali feldspar (alkali feldspar crystallizes first at lower temperatures and fluid-saturated conditions only). The last phase to appear near the solidus is muscovite. If we assume crystallization with 6 wt. % H_2O in the melt, the plagioclase stability field starts at ~820 °C, tourmaline, alkali feldspar, and quartz stability fields start all at ~750 °C, biotite stability field starts at ~730 °C and muscovite stability field at ~680 °C. At greater water contents in the melt and at lower pressure all stability fields are shifted to lower temperatures. However, the stability of individual phases is dependent also on the composition of the melt.

Generally, tourmaline is stable over a wide temperature-pressure range up to ~900 °C and ultra-high pressures (e.g. Benard et al., 1985; Ertl et al., 2010), which suggests that temperature and pressure are not the critical factors governing the tourmaline stability. The crystallization of tourmaline in granitic melts depends on the availability of essential structural components, that is, B, Mg, Fe and Al. If a melt crystallizes one or more mafic phases, the tourmaline saturation reduces to availability of B and the activity of excess (or peraluminous) Al (London, 1999). Tourmaline should be stable only in strongly peraluminous magmas (ASI > 1.2; ASI is defined as molecular Al_2O_3 / ($CaO - 1.67P_2O_5 + Na_2O + K_2O$, Shand, 1943) with over 2 wt. % B_2O_3 (Wolf and London, 1997). The lower limit of activity of water (aH_2O; water pressure in the liquid divided by that of pure water at the same temperature) in the melt required to stabilize tourmaline is not known, but it should be very low and reached only at very undersaturated environments (London, 1999). Low activities of ferromagnesian components tend to severely limit the amount of crystallized tourmaline (e.g. London and Manning, 1995), but tourmaline can still form in small quantities when the ferromagnesian content of the melt is exceedingly low, if the activities of B and excess Al are sufficiently high (Wolf and London, 1997). Overall, there is an antipathetic relationship

between tourmaline and biotite in granitic systems as a consequence of competition for the ferromagnesian components (Pesquera et al., 2013; Wolf and London, 1997).

1.2.2 Kinetic effects on crystallization

Phase equilibria define the evolutionary scenario if the kinetics of equilibrium reactions is sufficiently fast. A contrary situation is, however, quite common and numerous magmas start to crystallize after significant undercooling only (undercooling means a disequilibrium state, in which the temperature of the melt sinked below the liquidus, or even solidus temperature, but crystallization has not begun yet – there is some nucleation delay).

Other kinetic effects include finite nucleation and growth rates of minerals, both are zero at equilibrium liquidus temperature, remain finite functions of undercooling, and often decrease at very high undercooling or near the glass-transition temperature (e.g. Swanson, 1977; Fenn, 1977; Muncill and Lasaga, 1988). The maximum of the nucleation density as well as of the growth rate in a synthetic granite with 3.5 wt. % H_2O occurs at undercooling of ~200 °C below the liquidus temperature, but the growth rate curves typically have wide peak and a more smooth shape, not speaking of their smaller range of values (Swanson, 1977). The shape of growth rate and especially of the nucleation rate (or nucleation density) function and their relative relationships have a critical influence on the resulting igneous texture (crystal size and morphology) (Brandeis and Jaupart, 1987a). According to Brandeis and Jaupart (1987a,b), the range of growth and nucleation rates in the interior of large intrusions at low undercoolings should be 10^{-12} to 10^{-10} $m.s^{-1}$ and 10^{-3} to 10^{-7} $cm^{-3}.s^{-1}$ respectively; but at high undercoolings, the growth and nucleation rates may reach 10^{-9} $m.s^{-1}$ and 1 $cm^{-3}.s^{-1}$ respectively. The thermal conduction models indicate that the growth rates in thin pegmatite-aplite dykes in California could be as high as 10^{-7}-10^{-8} $m.s^{-1}$ (Webber et al. 1999). Nucleation density is expected to vary in granitic systems from zero to greater than 10^8 sites cm^{-3} (Swanson, 1977). The growth and nucleation rates are different for different minerals in a melt at distinct temperature and pressure conditions (e.g. Swanson, 1977). For example in the undercooling region, that maximizes growth rates for albite, quartz, and K-feldspar, the nucleation densities of albite and quartz are higher than those of K-feldspar (Fenn, 1977; Swanson and Fenn, 1986; London et al., 1989). In granite systems, maximum growth rates and nucleation densities coincide for quartz and plagioclase but the growth rate of alkali-feldspar is two orders of magnitude greater while the nucleation density for this phase is relatively low (Swanson, 1977). As a result, occasional big flaring (fan-like) megacrysts of K-feldspar are found in pegmatites. In highly evolved melts, additional volatile constituents (e.g., B, P and F) inhibit nucleation because of their depolymerizing effect on the melt structure. The maximum nucleation density by a factor of four in hydrous melts and it is shifted toward lower undercooling by ~100 °C (Fenn, 1977).

Crystal growth rates are dependent on diffusion and advection rates, and they affect the resulting crystal shape. The diffusion rate, related to the diffusivity of components in the melt, is directly proportional to temperature and inversely proportional to viscosity of the melt and

the radius of the species (Stokes-Einstein equation; Einstein, 1905). The diffusion rate thus becomes function of the melt viscosity as discussed above. Complicating factors are local-charge coupling, for instance, alkali migration is often related to movement of other oxide components (e.g., Al), and they diffuse at least as rapidly as the fastest-moving component in the system, and their migration is therefore independent of viscosity (Acosta-Vigil et al., 2005). However, the diffusion coefficient for boron in a haplogranite melt at 800 °C and 2 kbar H_2O is $5.6 \cdot 10^{-12}$ $m^2.s^{-1}$ (London, 2009), which is three orders of magnitude faster than that of Al in B-absent melt at similar conditions, probably due to the effect of boron on the reduction of melt viscosity (Acosta-Vigil et al., 2006). The diffusivity of Si in the volatile-rich hydrous silicate melt increases by about three orders of magnitude over that in simple hydrous haplogranitic liquid at the same pressure and temperature , because of the viscosity-reducing effect of fluxes (Acosta-Vigil et al., 2006).

The crystal morphology is a function of the *D/Y* ratio, where *D* is the mobility of the slowest crystal-forming component in the melt, and *Y* is the growth rate (Kirkpatrick, 1975). The *D/Y* ratio decreases with increasing undercooling; indicating that, at small undercoolings, *D/Y* is relatively large and crystals are expected to have smooth planar surfaces. As the *D/Y* ratio decreases, however, dendritic, skeletal, fibrous or spherulitic spherulitic morphologies develop. The elongation of crystals should be a function of undercooling, nature of nucleation and temperature gradient in the melt body – the fast-growth direction must predominate over others that lie at some other angle to it (London, 2009; Nabelek et al., 2010).

1.2.3 Solidification fronts

Magmatic bodies frequently cool from the margins to the interior and their solidification usually proceeds in solidification or crystallization fronts, which grow from the chilled margins inward (Marsch, 1996, 2002). The crystallization front is defined as a transient space interval between the solidus and liquidus temperatures in a cooling igneous body. The smaller the temperature gradient in the melt, the wider the crystallization front should be and the proportions of crystals should slowly increase, with the probability of nucleation being random in a relatively wide area. Nucleation can be homogeneous (without the aid of foreign material), or heterogeneous (the crystals nucleate on some foreign substrate, for example on the walls of body, earlier phenocrysts or fluid bubbles), which is usually more favourable (Flemmings, 1974). At undercooled conditions the probability of crystal nucleation is highly localized along the margins of the melt body, where undercooling is the greatest (London, 2009). The margins of the body could be undercooled even under the solidus temperature before the onset of crystallization, and then even if the temperature gradient in the melt is high, the solidification front tend to be wide, because the liquidus temperature is far in the space. However, it should be very dense, because nucleation is highly localized and probably heterogenous on the walls of the body and later on the tip of the dense solidification front. Therefore the crystallization and the kinetic effects affecting it are restricted to a narrow part of melt in the igneous body. The main most rapid direction of growth (with the greatest

crystallization potential) is perpendicular to the solidification front along the greatest gradient in the temperature toward the liquidus temperature. Crystals that grow in another angle to the growth front may lack essential components because they loose contact with the melt (London, 2009). Than the smaller is the temperature gradient in the melt, the longer can become the crystals, because their length is limited by the distance between the site of nucleation and the position of the mineral's liquidus temperature (Nabelek et al., 2010).

1.3 Geological framework

The Říčany pluton is a part of the Central Bohemian Plutonic Complex, which is a composite batholith comprising a great number of various plutonic and dyke rocks, situated along the boundary between two major tectonic units in the Bohemian Massif, the Barrandian (= Bohemicum) and Moldanubian blocks. It covers about 3200 km^2 in the Czech Republic near Prague. The rocks in the Central Bohemian Plutonic Complex can be divided into several compositional groups and even more petrographic types (Holub et al., 1997b). The Říčany type of granite, which falls into KMgG (high-K and high-Mg granites) compositional group, is in respect to other granitoids of the Central Bohemian Plutonic Complex much richer in fluorine, and has highly magnesian biotite (*mg#* = 53-59; *mg#* = $100Mg/(Mg+Fe_{tot})$) (Fiala and Vejnar, 1976). The Říčany type of granite is represented by the Říčany pluton, which is situated at the northernmost apex of the Central Bohemian Plutonic Complex.

1.3.1 Petrography

The Říčany pluton consists of one rock type – the muscovite-biotite Říčany granite, which is monotonous mineralogically but variable structurally and chemically (concerning trace elements). It was characterized in greater detail by Holečková and Šmejkalová, 1958. The Říčany pluton forms a rough circle in map view, with the eastern margin concealed beneath Permian clastic sequences, and it is concentrically zonal. The core forms equigranular medium-grained or weakly porphyritic granite, whereas the rim strongly porphyritic granite, with abundant K-feldspar phenocrysts (approximnately 4-7 cm in size). The boundary between this two types of granite is wide and unsharp, the content and size of the K-feldspar phenocrysts decrease gradually from the margin to the center of the pluton. The average modal composition of the core and of the rim is almost identical (vol %): Quartz 26 and 29, K-feldspar 31 and 27, plagioclase (16 % An) 36 and 35, biotite 6 and 7, respectively (unpublished data of Steinocher, 1950-1958, cited in Němec, 1978). Along the southern roof contact of the pluton, between Jevany and Černé Voděrady, stretches an aplite margin about 300-400 m in width, and the massif is transacted by numerous aplite dykes whose widths range from few centimetres to some meters. The aplite dykes are extremely rare in the Paleozoic roof of the massif. This aplites are mineralogically identical, but the dyke ones are homogenous, whereas the marginal display banded structure with abundant tourmaline. The modal composition of the aplites is as follows (vol %): Quartz 37, K-feldspar 27, plagioclase (9 % An) 31, and tourmaline, muscovite and biotite in variable amounts (unpublished data of

Steinocher, 1950-1958, cited in Němec, 1978). In the eastern part of the massif the Jevany leucogranite crops out, forming a separate intrusion not related genetically with the Říčany granite or its aplites (Němec, 1978). It was characterized by Šmejkalová, 1960. It is finer and poorer in femic minerals than the Říčany granite, it lacks tourmaline, and its plagioclase is acid.

1.3.2 Geochemistry

Within the Central Bohemian Plutonic Complex, the Říčany granite together with the Sedlčany granite and the Zbonín granite falls into the group of K-Mg-rich granites, which has an affinity to the ultrapotassic rocks of the Central Bohemian Plutonic Complex (Holub et al., 1997b). The granites of this group are K-rich and Ca-poor, with high *mg#* and Cr, rich in hygromagmatophile elements and highly radioactive. The Říčany granite is among them characterized by relatively lower K_2O/Na_2O, higher SiO_2, and increased fluorine content (Holub et al., 1997b). It has the strongest LREE enrichment amongst the granitoid types within the Central Bohemian Plutonic Complex, and the lowest total content of HREE (Janoušek et al., 1997). In general, however, it is a fairly fractionated, peraluminous (A/CNK = 1.01-1.13; Trubač et al., 2009), S- to A-type granite (Trubač, 2008; Jakeš, 1977; Janoušek, 1991), with a high and restricted SiO_2 range (c. 69-72 %; Janoušek et al., 1997). It displays elevated contents of Sn, Be, F, B, W and Nb (Vejnar, 1973), very low contents of Ba and Mo (Němec, 1978), and variable and negative Eu anomaly (Eu/Eu^*=0.8-0.9; Janoušek et al., 1997). According to Janoušek et al. (1995b), the Říčany granite has a transitional character between high-K calc-alkaline and shoshonitic suites, with some affinities to the subalkaline group of Barbarin (1990), which develops typically in an environment transitional between late orogenic compressional and extensional regimes. The Sr–Nd isotopic signature of the Říčany granite is similar to that of the metasediments of the Moldanubian unit, which combined with the generally peraluminous nature of the granite, is consistent with the magma derivation from the paragneisses or leucocratic granulites of the Moldanubian unit, or from a mixture of metasedimentary material from the Moldanubian and Teplá–Barrandian units (Janoušek et al., 1995b).

The major-element compositions do not vary greatly between the two varieties of the Říčany granite, but certain trace elements show significant ranges in concentration, which is typical for fractionated granites. The degree of fractionation decreases from the pluton margin inward: the outer granite is more evolved than the central, and the pluton thus shows a reverse zoning, reflected nearly exclusively in the trace element compositions (Janoušek et al., 1997; Janoušek, 1991). Ba, Sr, Th and Zr increase, and Rb decreases progressively from the margin to the center of the pluton, moreover SiO_2 slightly decrease and K_2O, Na_2O and CaO slightly increase towards the center (Janoušek et al., 1997). According to Němec (1978), F and Be display no areal variation, whereas Sn and B strongly increase towards the margin of the pluton, and are highest in the marginal aplites (especially for the case of boron). Besides that, the aplites are characterized by high Be and low F content. In the mantle of the pluton, near

Tehov, there is a pneumatolitic-hydrothermal phase, cassiterite-bearing tourmaline-quartz formation, which points to a volatile loss from the pluton. According to analyses in Němec (1978), only B was supplied into the rock.

1.3.3 Intrusion age and emplacement

The Central Bohemian Plutonic Complex was emplaced in a relative short time span of about 10 Ma in Lower Carboniferous (approximately 351 – 340 Ma) (Holub et al., 1997a). The Říčany pluton was dated by a $^{40}Ar/^{39}Ar$ biotite age of 336 ± 3.5 Ma (unpublished data of H. Maluski, cited in Janoušek et al., 1997). It is one of the youngest and most evolved units of the Central Bohemian Plutonic Complex, and it is a post-tectonic, shallow-level intrusion (peak pressure estimated at approximately 0.2 GPa from contact metamorphic mineral assemblages; Kachlík, 1992). Its contact relationships against the surrounding units are intrusive, transgressive, or faulted: (1) to the northwest, it stands in an steep intrusive contact with the Neoproterozoik (Ediacaran) siltstones and shales of the Teplá-Barrandian unit, which plunges 70-80° under the pluton (Kodym, 1925); (2) to the southwest, it contacts with the 354 Ma old Sázava tonalite (Janoušek et al., 2004) and a Lower Paleozoic metasedimentary roof pendant (metamorphic "islet"), and the contact was modified by late, post-emplacement brittle faults and cataclastic zones; and (3) in the east, the pluton is transgressively overlain by Permian clastic sequences, of which contact has also been reactivated by younger brittle faults. Janoušek et al. (1995a), and Trubač et al. (2009), discovered a highly unusual fabric pattern in the Říčany pluton, which together with the reverse zoning of the pluton indicates the flow mechanism during its emplacement. They observed a steep concentrical margin-parallel magmatic foliation (defined by K-feldspar phenocrysts and biotite) and magnetic foliation carried by biotite in the both varieties of granite in the pluton, but a shallowly-plunging magnetic lineation (0-25°) parallel to the circumference of the pluton margin in the outer strongly porphyritic variation of the Říčany granite, and a steep magnetic lineation (60-80°) in the equigranular pluton center (Fig. 1.4). The proposed mechanism of magma ascent is a viscosity-partitioned right-handed helical flow in a steep-sided conduit, in which the low-viscosity phenocryst-poor center flowed vertically and faster, and the high-viscosity phenocryst-rich outer margin flowed helically subhorizontally and slower. The two varieties of the Říčany granite may represent two closely-related magma batches ascending through the steep-sided conduit from an underlying, stratified magma chamber to a volcanic feeder at the surface, as indicates the cryptic trace-element reverse zoning (Janoušek et al., 1997). At depth and to the east of the Říčany pluton, there is a major negative gravity anomaly indicative of granite mass about 40 km across (Tomek, 1974; Orel, 1975).

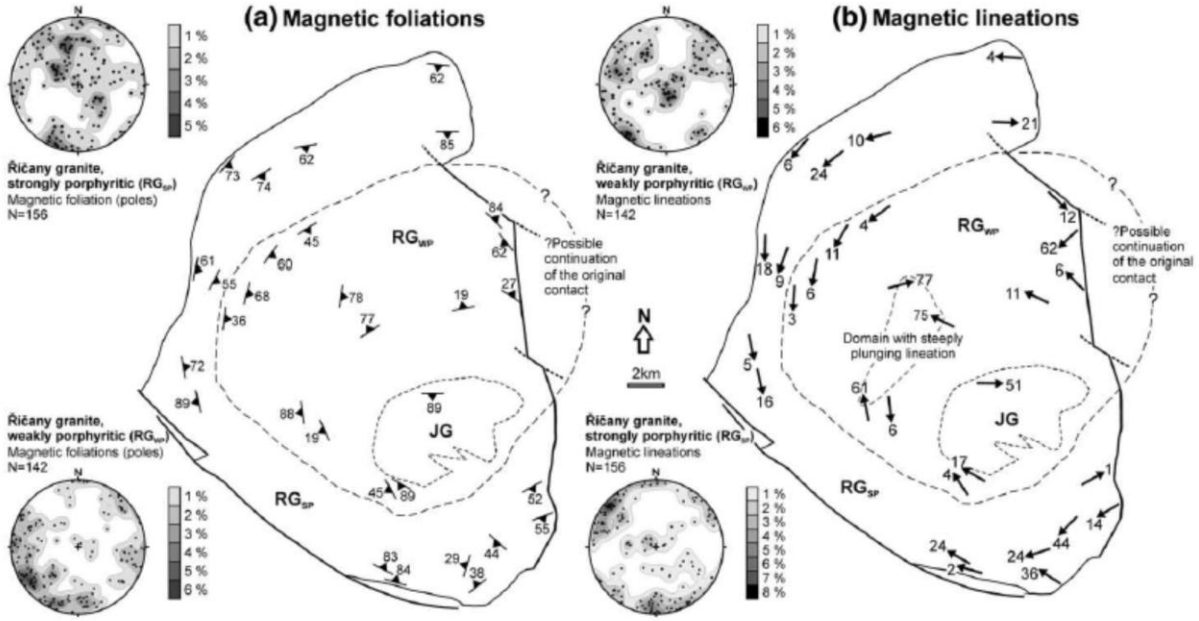

Fig. 1.4 Map of magnetic foliations (a) and lineations (b) in the Říčany pluton (AMS); Trubač et al., 2009.

1.4 Research objectives and structure of the thesis

The focus of this work is the aplite margin of the Říčany pluton, or more precisely a belt of aplito-pegmatitic, modally and texturally layered rocks. Such layered aplites known as "line rock" and alternating aplitic and pegmatitic textures, occur often in evolved pegmatite-aplite dykes or bodies. Excellent examples are studied in California (Ramona, Pala, and Mesa Grande Pegmatite Districts) (Morgan and London, 1999; London et al., 2012; Webber et al., 1997; Webber et al., 1999), Namibia (Frindt and Haapala, 2004), but also in Czech Republic (Brno Batholith – Hönig et al., 2010, Podlesí stock – Breiter et al., 2005). Tourmaline as well as garnet, or even biotite layered line rock is a typical part of the thin, sheet-like composite pegmatite-aplite dykes in California. It is usually part of the lower portion of the dykes (if subhorizontal), which are typically zoned (massive aplite or graphic pegmatite at the margins of the dyke, line rock in the lower middle part, graphic pegmatite in the upper middle part, and blocky pegmatitic core with miarolitic pockets). Similar dykes cut the Gross Spitzkoppe granite stock in Namibia, but layered aplites and pegmatites are also at the margin of the stock itself (that is called "stockscheider"), and there is also one dyke of orbicular granite cutting the stock. Very similar features with our rocks have the dykes of Hlína granitic suite in Brno Batholith in Czech Republic. Fine-grained aplite with pronounced garnet layering alternate with coarse-grained pegmatitic units, where unidirectional solidification textures (comb crystals) occur. The Podlesí granite stock is a peraluminous, F- Li-, and P-rich, Sn, W, Nb, Ta-bearing granite system, where occurred some processes typical of intrusions related to porphyry type deposits. Layering and unidirectional solidification textures are evolved in stockscheider along its margin as well as in dykes. All the authors think, that this textures are

the result of boundary-layer crystallization in an undercooled melt (constitutional zone-refining for coarse-grained parts and oscillatory diffusion-controlled nucleation for line rock), combined to various degree with changes in the temperature and pressure conditions (that could function for example as a trigger for line-rock crystallization, because of changes in undercooling), but it is still an issue for discussion. These rocks very probably represent an excellent and interesting example of magmatic textures, which provide an ideal opportunity to study crystallization kinetics and rheology in natural magma chambers, which are the key parameters for dynamics of magmatic reservoirs and differentiation of magmas. However, igneous textures are often underappreciated and rarely used for studying this petroogic field, which could be used not only in science, but also for example in material engineering.

The aim of this work is (1) to document these unique rocks, (2) to try to interpret the textures and reevaluate the possible hypotheses available to explain the layering of these rocks. This will be achieved by macroscopic as well as microscopic study and documentation of the textures and the geologic situation (summarised in the chapters 2: Geological setting and sample description, and 3: Petrography), as well as by mineral chemistry study (chapter 4), which will be used to learn about possible chemical evolution and differentiation within the bands, or to learn about the thermal evolution of the melt. The origin and evolution of the melt will be studied by whole-rock geochemistry (chapter 5). To interpret all the obtained data, an exploration of current knowledge about the theme will be done (chapter 1: Introduction), which will be applied to and compared with our data in the chapter 6: Interpretation and discussion. Finally, petrogenetic model will be proposed (chapter 7).

2 Geological setting and sample description

This study focuses on a ~500-600 m wide and ~5 km long belt of granitic tourmaline-bearing aplites and pegmatites along the southern margin of the Říčany pluton. The true thickness of the aplite-pegmatite body is unknown. The unit neighbours with the marginal strongly porphyritic Říčany granite to the north, with the Sázava tonalite to the southwest and with the Lower Paleozoic metasedimentary roof pendant (metamorphic "islet") to the south and southeast (Fig. 2.1). It is transacted by northwest-southeast oriented gabbro dykes, as well as the Sázava tonalite. There is plenty of blocky petrographic studying material, but *in situ* outcrops are rare. Spatial distribution of the material and sporadic direct observations of the contact relationships indicate sharp intrusive contacts against all the surrounding units. Studies of anisotropy of magnetic susceptibility (AMS) at the rare *in situ* outcrops indicate subhorizontal magnetic fabrics in the majority of aplite-pegmatite body (it has steeper magnetic fabrics close to the contact with Říčany pluton – Fig. 2.2), whereas the Říčany pluton has steep magmatic and magnetic foliations (Janoušek et al., 1995a; and Trubač et al., 2009; Fig. 1.4). Also the presence of line rocks and similar geopetal indicators suggests a rather gentle slope of the aplite-pegmatite body. A useful supplementary information could be provided by drilling (if ever performed for lithium or tin exploration).

Říčany pluton is transacted by numerous granitic aplite dykes with typical widths of few centimetres and there is a set of wider (width: few metres, no in-situ outcrops) microgranite dykes near Černé Voděrady (Fig. 2.1). In the eastern part of the outcrop area, the marginal Říčany granite encloses numerous xenoliths (X0-X00 cm) of quartzites and metasedimentary hornfelses. The xenoliths have angular shapes and locally show evidence for brittle fracturing and melt penetration. Biotite hornfelses provide only a limited evidence for boron metasomatism (irregular tourmalinization), but there are abundant tourmalinites ~3-4 km on the northwest from the outcrop area, near Tehov. There is a thin unit of biotite granodiorite irregularly outcropping along the margins of the aplite-pegmatite belt (on the north as well as on the south of the belt) with sharp contacts as well (Fig. 2.1). The granitic aplite of the belt has unidirectional solidification textures, layered texture with abundant tourmaline (line rock) and pegmatite layers, dykes and pockets. The whole belt does not show any specific lithological zoning. Line rock with pegmatite layers is present throughout its horizontal thickness with local disappearance of pegmatite layers or modal banding (intervening massive aplites). Pegmatite pockets are present in the massive aplite as well as in the layered aplite and marginal Říčany granite. Flaring feldspatic megacryst up to few decimetres long are locally present. Flow textures are locally recognizable (Fig. 2.9). Several textural and lithological types of rock were distinguished.

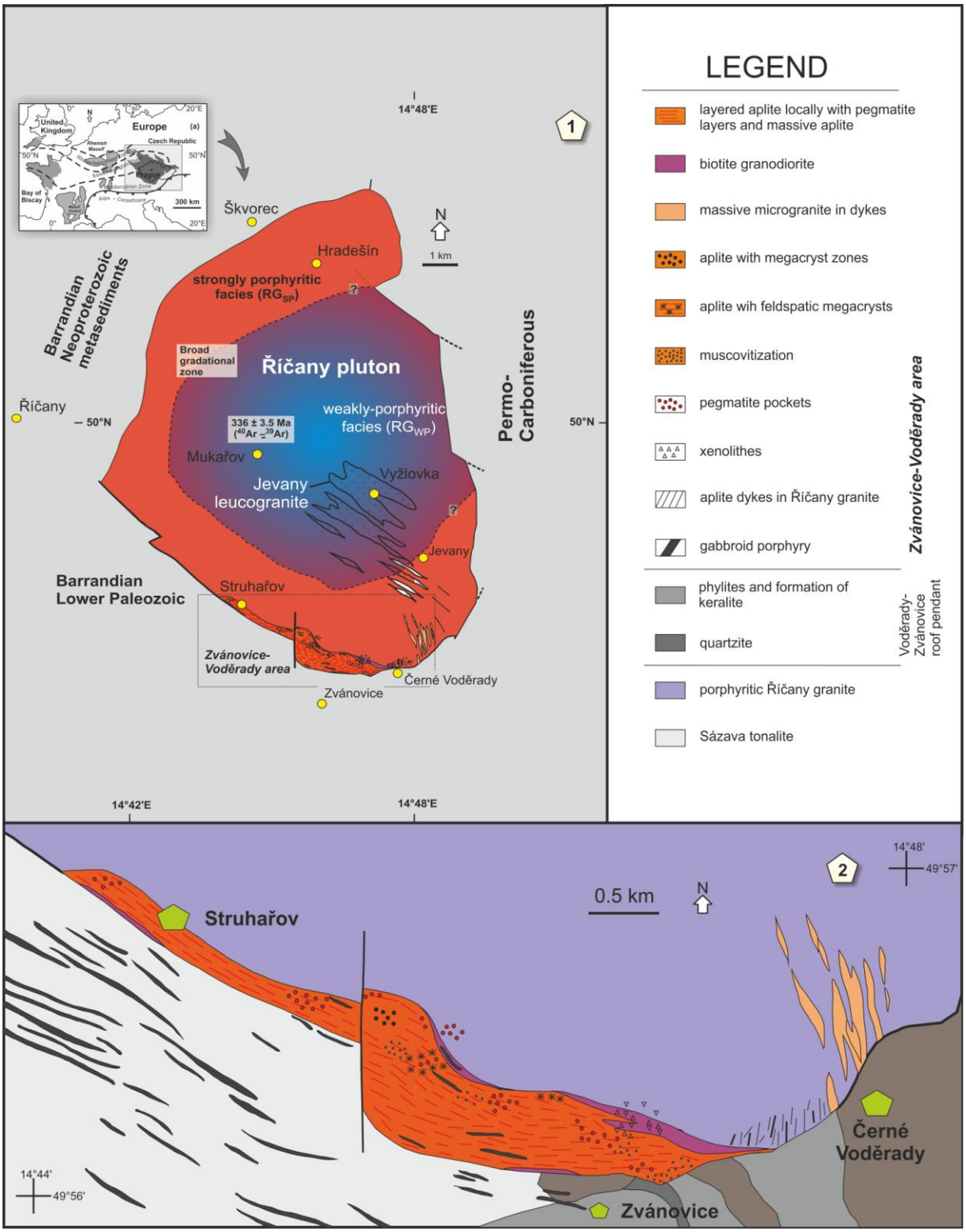

Fig. 2.1 Simplified geological map of the outcrop area. Small black and white map shows position of Bohemian Massif in Europe. (1) Říčany pluton and related position of the aplite-pegmatite belt. (2) Detailed geological map of the aplite-pegmatite belt.

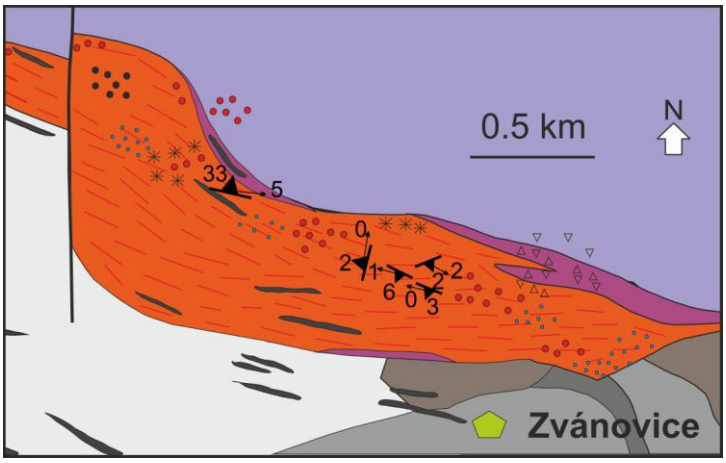

Fig. 2.2 Map of magnetic foliations and lineations measured on the rare *in-situ* outcrops in the aplite-pegmatite belt (AMS).

2.1 Biotite granites and dyke rocks in the Říčany pluton

Marginal Říčany granite is a medium-grained biotite granite with strongly porphyritic, massive texture (Fig. 2.3). Grain sizes vary from less than ~1 millimetre up to ~2 centimetres. The ~2 centimetres big megacrysts are formed by K-feldspar, other megacrysts up to ~1 centimetre big are formed by quartz or plagioclase, biotite forms grains in the matrix less than ~1 millimetre big (together with the other minerals). Megacrysts are irregularly distributed in the rock, but they are missing in the granites from the eastern part of the outcrop area.

Thin unit of black and white equigranular biotite granodiorite with massive texture occurs along the margin of the aplite-pegmatite belt. It is often strongly altered. Quartz, feldspars and biotite form ~1-4 millimetres big grains. Biotite is regularly distributed in the rock, but locally concentrates into biotite-rich enclaves with smaller grain sizes (up to ~1 mm), which are macroscopically more black than the rest of the rock (Fig. 2.3).

Microgranite dykes near Černé Voděrady are formed by massive, equigranular or weakly porphyritic tourmaline microgranite (grain size up to ~2 mm, rare megacrysts up to ~4 mm) (Fig. 2.4). It can contain muscovite or biotite or both apart from black tourmaline, quartz and feldspars. Sharp contacts of muscovite-tourmaline microgranite and only tourmaline microgranite were found within one dyke. Muscovite, biotite and tourmaline can be oriented in one direction and oriented tourmaline can even rarely form indistinct bands.

Granitic aplite of the aplite dykes in the Říčany granite with typical widths of few centimetres is a fine-grained (grain size up to ~2 mm or smaller), tourmaline-bearing aplite (no muscovite or biotite were found), which is macroscopically white or grey. Tourmalinization of the host granite often occurs in the vicinity of these dykes (Fig. 2.4). Black columnar tourmaline can form modal bands, which are typically parallel to the dyke margin. Grain size can also vary in layers parallel to the dyke margin and some bigger dykes

(width ~10-15 cm) have pegmatite layer in the middle (grain sizes up to ~1.5 cm), which is compound of mainly big feldspar and quartz grains and rare tourmaline and garnet grains.

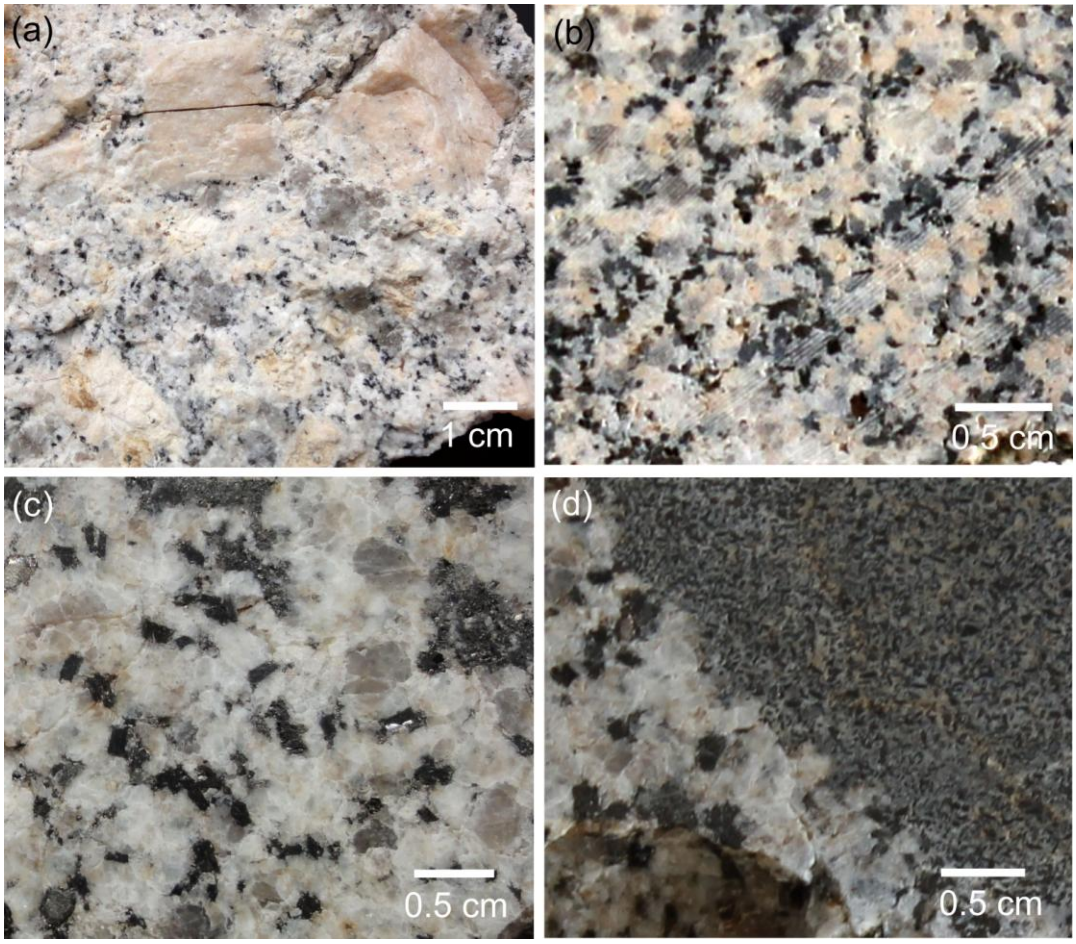

Fig. 2.3 Photographs of marginal Říčany granite and biotite granodiorite: (a) sample DT5/2 – strongly porphyritic variety of the granite; (b) sample ZV7 – equigranular variety of the granite from the eastern part of the outcrop area; (c) sample ZV8 – biotite granodiorite; (d) sample ZV8 – biotite-rich enclave in biotite granodiorite.

2.2 Massive and layered aplites

Massive aplite, which locally outcrops in the aplite-pegmatite belt, is a massive, fine-grained rock typically with pink color (grain size up to ~2 mm or smaller) (Fig. 2.5). It contains several millimetres large columnar grains of black tourmaline (its size can vary), irregularly disseminated in the rock. It contains also muscovite or rarely biotite or various combinations of the three minerals in some areas, or it contains areas, which – despite of the same grain size and matrix coloration – contain no tourmaline, muscovite or biotite; the transition between these types is sharp. Muscovite and biotite are the same size as the matrix grains and are irregularly distributed as well, only biotite is locally concentrates itself into small patches. The tourmaline-free type seems to be parental to (it surrounds) tourmaline-bearing pegmatite pockets; or when the pegmatite pockets are in the tourmaline-bearing, or

analogically muscovite-bearing etc., aplites, the concentrations of these minerals decrease in the aplite around the pegmatite pockets. The solidification of pink aplite provides also a nucleation medium for the growth of large flaring (fan-like branching „megadendritic“ arrangement) K-feldspar crystals.

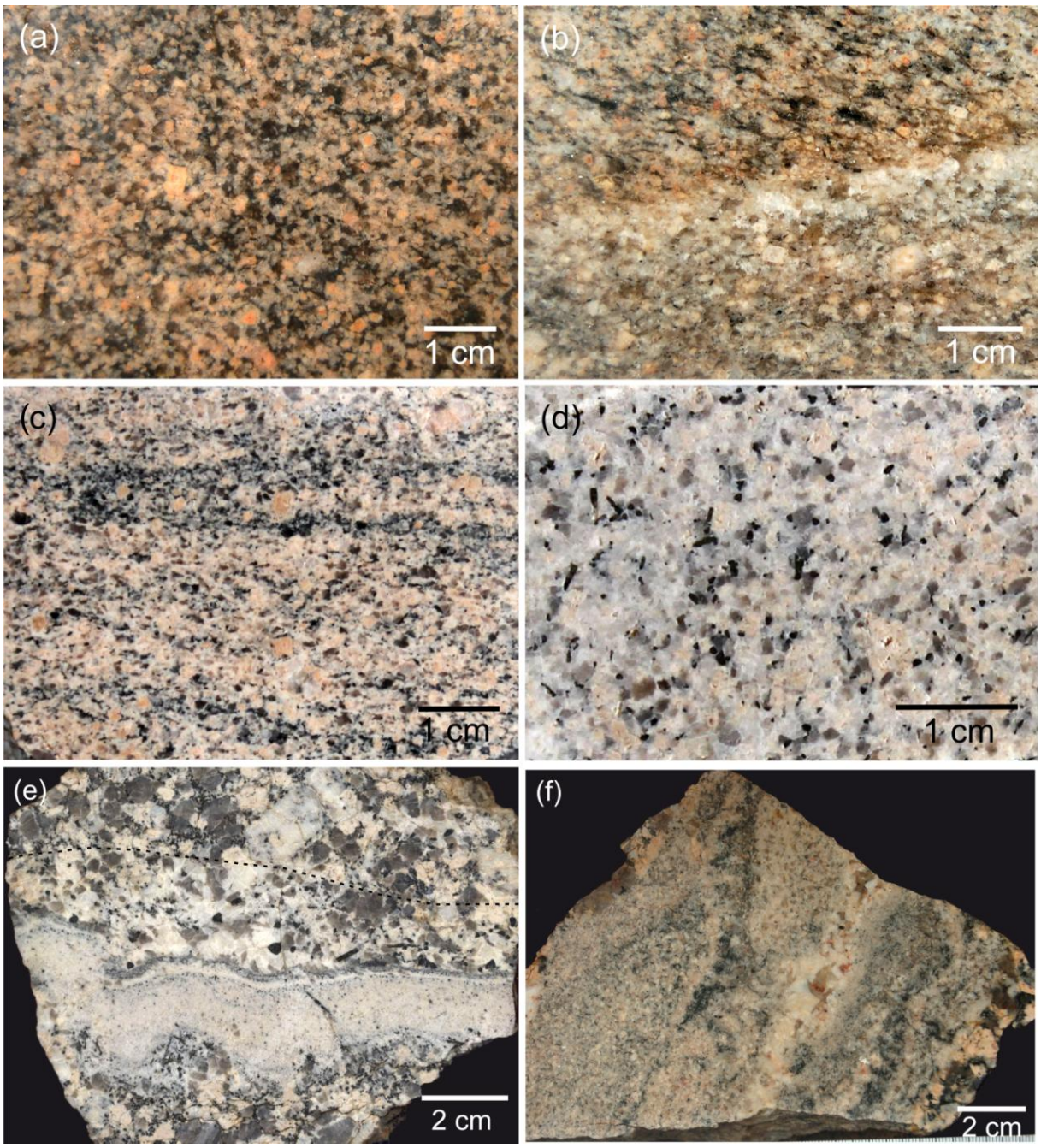

Fig. 2.4 Photographs of microgranites from microgranite dykes near Černé Voděrady, and of aplite dykes in the Říčany pluton: (a) sample DT30; (b) sample DT28 – contact of muscovite-tourmaline microgranite with oriented muscovite and tourmaline grains (upper part) and only tourmaline microgranite (lower part); (c) sample TDX4 – indistinct bands of tourmaline; (d) sample TDX3; (e) sample DTX3 – the dashed black line indicates the area of tourmalinization of the Říčany granite; (f) sample JT3 – one of the widest aplite dykes with a garnet-bearing pegmatite layer in the middle.

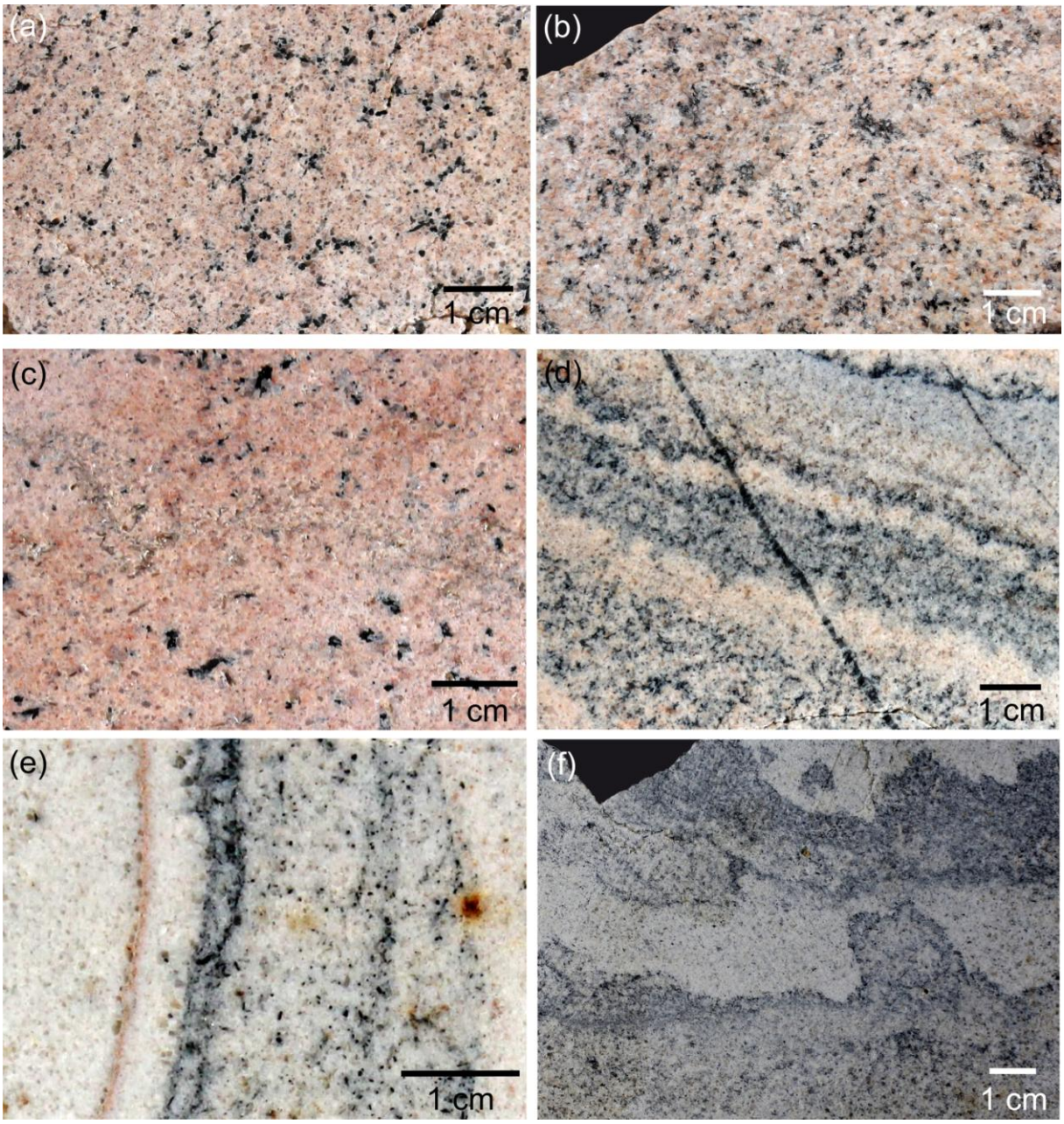

Fig. 2.5 Photographs of massive and layered aplites: (a) sample ZV1 – massive tourmaline aplite; (b) sample JT2N2 – massive aplite with biotite concentrated into small patches; (c) sample AP1 – a muscovite-rich band surrounded by a massive tourmaline aplite; (d) sample TJ7B – pink tourmaline layered aplite transacted by a late hydrothermal vein; (e) sample TJ6B – layered aplite with a tourmaline-rich and a thin garnet-rich band; (f) sample TJ24 – typical white-grey layered aplite with round protrusions in tourmaline-rich bands.

Layered aplites (line rocks), which form the majority of the aplite-pegmatite belt, are very fine-grained to fine-grained and have typically white-grey colors. The transition of pink massive aplites and white-grey layered aplites is gradual, there are samples of pink aplite with modal tourmaline and muscovite bands. The modal layering in the white-grey aplites is formed by ~0.2-5 centimetres thick tourmaline-rich (grey) and tourmaline-poor (white) bands, or less often by thin garnet-rich bands (pink) (Fig. 2.5). No biotite and rarely muscovite

occurs in the layered white-grey aplites. Relatively more muscovite can be found in them when they are pinkish. The bands are straight or show round protrusions that are reminiscent of advancing crystallization fronts and growth controlled by diffusion. Rarely bands cut each other or have another direction (they are usually parallel), which is interpreted like flow textures.

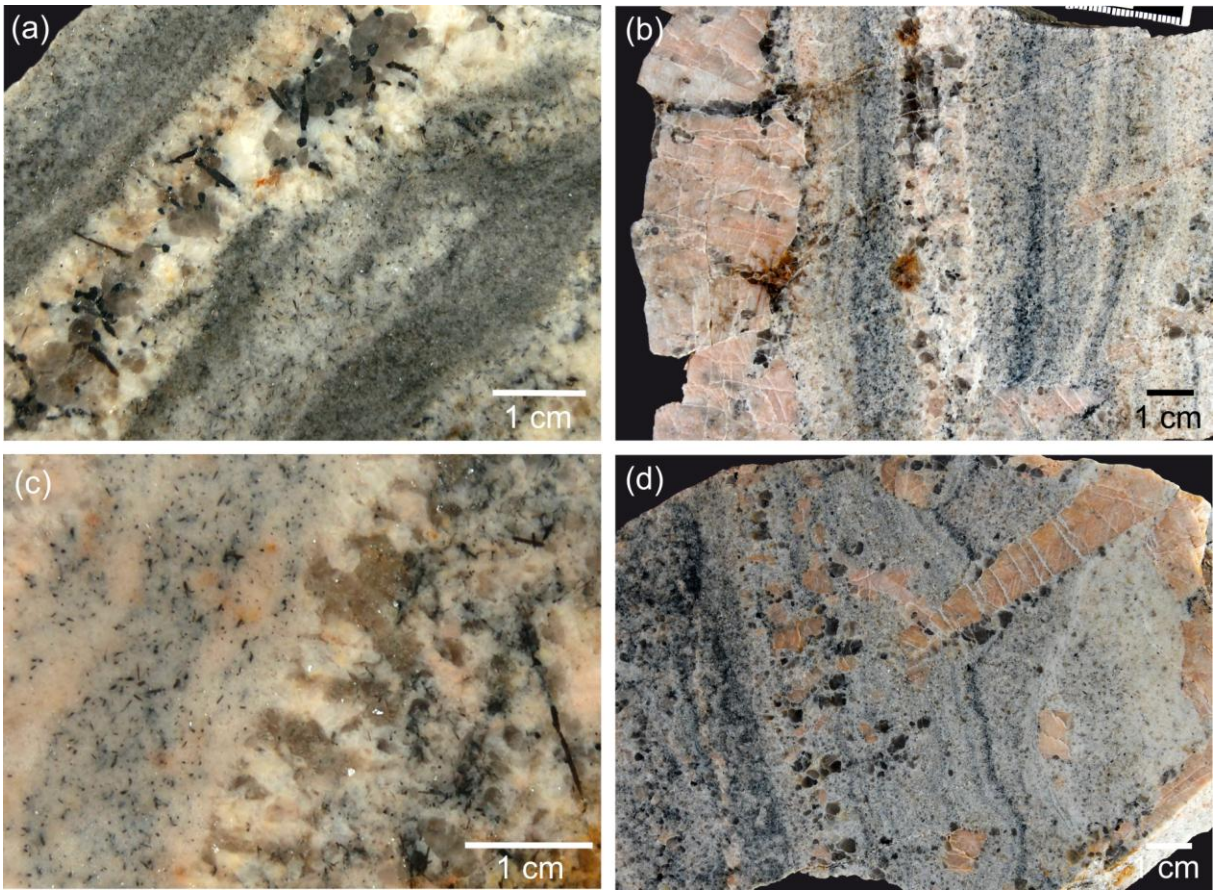

Fig. 2.6 Photographs of pegmatite layers: (a) sample ZV6; (b) sample TJ2 – notice the two solitary feldspar megacrysts cutting the bands in the right part of the picture, and the elongated feldspar grains in the pegmatite layer; (c) sample DT32 – muscovite megacrysts perpendicular to layering (comb muscovite); (d) sample TJ23 – feldspar megacryst extending from the pegmatite layer and cutting the bands, and solitary feldspar and quartz megacrysts nucleated on a line parallel to layering.

2.3 Pegmatite layers, megacryst zones and pegmatite pockets

Grain size can vary in layered aplites too – the layering contains sometimes "pegmatite layers" (Fig. 2.6). These layers are characterized by abrupt change in grain size – it is always bigger than the grain size in the surrounding aplite, but can be various (up to several cm), and can even further grow within the layer. They are formed by various proportions of quartz, feldspars, tourmaline, muscovite and garnet, but quartz and feldspars are usually the most abundant phases. Unidirectional solidification textures (for example small flaring or elongated megacrysts perpendicular to the layer direction, nucleating on one margin of the layer) can be

recognized, especially on muscovite or feldspars (Fig. 2.6 b,c). Big megacrysts sometimes extend from one side of the pegmatite layer perpendicularly (or with some angle) to the layering and "cut" the tourmaline bands (Fig. 2.6 d), which is also an evidence of unidirectional solidification. Big feldspar megacrysts sometimes even grow isolated in the fine-grained layered aplite (and cut the bands too), or nucleate on one "line" parallel to the layering, but do not form coherent pegmatite layer (Fig. 2.6 d).

Approximately in the middle of the outcrop area (Fig. 2.1) is a zone of extremely fine-grained massive tourmaline aplites with pink-grey colour alternating with what we call "megacryst zones" (Fig. 2.7). Megacryst zones are coarse-grained zones (grain size up to ~2-3 cm and it can evolve within the zone) with quartz, feldspars, tourmaline and muscovite, often with clear unidirectional solidification textures. They have sharp, but often undulated contacts with the very fine-grained massive tourmaline aplite, which can exhibit a thin (up to 1 cm thick) pink zone depleted in tourmaline along the megacryst zone contact. Black tourmaline megacrysts can extend from one side of the megacryst zone perpendicularly or with some angle to it, forming so called comb layer, which is one of the unidirectional solidification textures. Bigger quartz grains nucleate on the surface of these tourmaline megacrysts, which together with the depleted layers in aplite indicates inhibited diffusion.

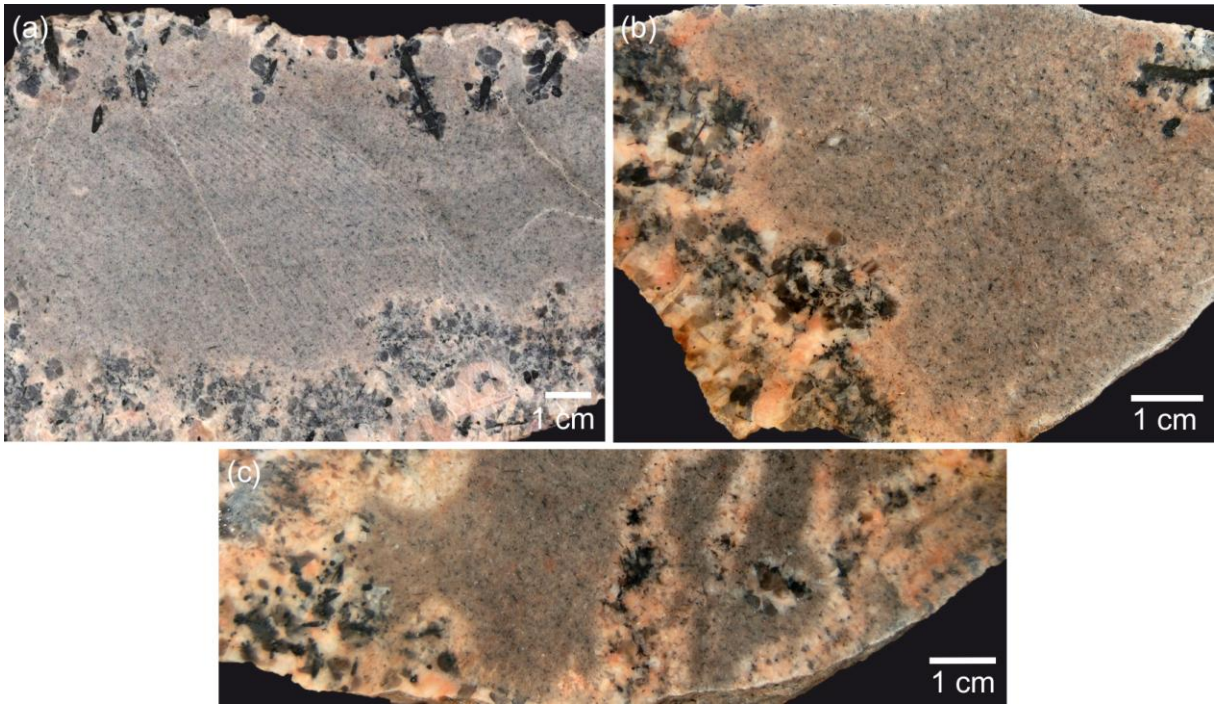

Fig. 2.7 Photographs of megacryst zones: (a) sample DT20 – tourmaline megacrysts extending from the megacryst zone with quartz grains around them; (b) sample DT20/1 – notice the lighter diffusion zone next to the megacryst zone; (c) sample DT20/3 – undulated contacts.

Pegmatite pockets occur in all the lithological rock types of aplite-pegmatite belt as well as in the Říčany granite, and they are connected to these units by sudden or sharp transitions. They contain various proportions of quartz, feldspar, black tourmaline and muscovite with

grain sizes up to several centimetres and have often graphic texture (Fig. 2.8). We incorporate also the large flaring K-feldspar megacrysts in massive aplites into this group (Fig. 2.8 b). Pegmatite pockets show often unidirectional solidification textures – elongated grains oriented perpendicularly to the pocket margin; this textures occur near the margin of the pocket and the grains seem to nucleate at the margin and grow into the center of the pocket (Fig. 2.8 c,d).

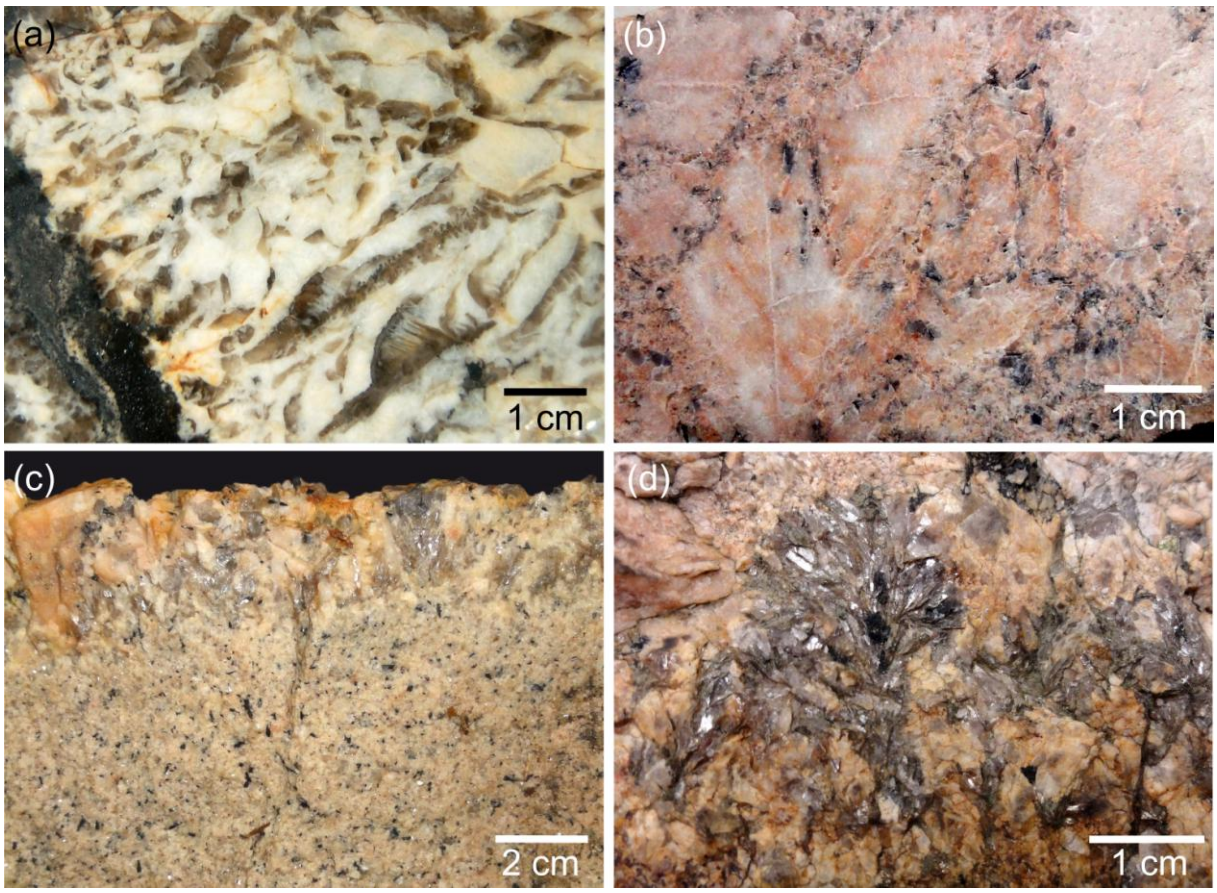

Fig. 2.8 Photographs of pegmatite pockets: (a) sample ZV10 – graphic texture; (b) sample DT10 – flaring K-feldspar megacrysts; (c) field documentation – comb muscovite; (d) field documentation – flaring muscovite megacryst.

2.4 Pegmatite dykes and hydrothermal veins

Layered aplites are transacted by what we call "pegmatite dykes", which are discordant to banding and disrupt the aplites in a semi-brittle manner (Fig. 2.9). This pegmatite dykes have evolved granite modal composition (almost only feldspars and quartz, less often tourmaline, garnet, muscovite, beryl, topaz), and various grain sizes, however always bigger than the grain size of surrounding aplite. The thickness of these dykes varies from several millimetres to several centimetres (Fig. 2.9). They can be accompanied by thin white "sugar zone" along their contacts (up to 0.5 cm thick), which is almost exclusively composed of albite-rich plagioclase (feldspatization) (Fig. 2.9 a).

Numerous hydrothermal veins occur mainly ~3-4 kilometres on the northwest from the aplite-pegmatite belt, near Tehov, but they can be found also in the xenoliths of quartzites and metasedimentary hornfelses (Fig. 2.9), within the aplite-pegmatite body and elsewhere. They are composed mainly of quartz and tourmaline and they are zoned, with oriented tourmaline grains on the margin and massive quartz core. Tourmaline is missing in the veins within the aplite-pegmatite belt, which are almost exclusively composed of quartz. These veins and other tourmalinization products were not considered in this study but some preliminary tourmaline analyses were carried out.

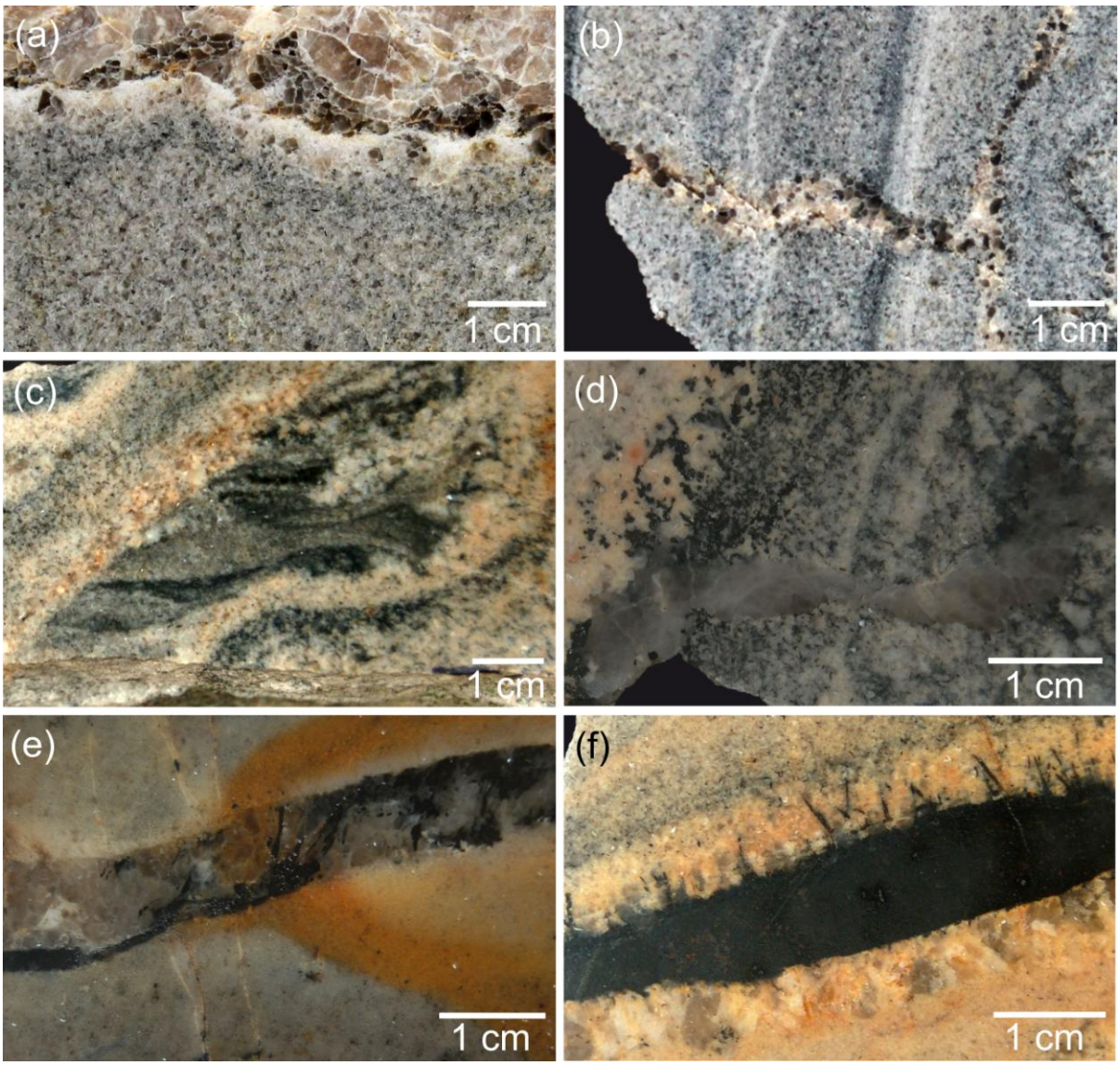

Fig. 2.9 Photographs of pegmatite dykes and hydrothermal veins: (a) sample TJ22A – zonal pegmatite dyke with "sugar zone"; (b) sample TJ19B – pegmatite dyke; (c) sample DT18B – pegmatite dyke and flow/erosional textures; (d) sample DT2/1 – hydrothermal quartz vein cutting layered aplite; (e) sample ZV11 – hydrothermal quartz-tourmaline vein cutting the xenoliths of hornfelse; (f) sample DT23 – hydrothermal quartz-tourmaline vein near Tehov.

3 Petrography

The rocks of the aplite-pegmatite belt, marginal Říčany granite and dykes in the granite are divided into 11 lithological and textural groups. Marginal Říčany granite is studied for comparison as the potential source rock of the aplite-pegmatite belt. Microgranite dykes and the thinner aplite dykes in marginal Říčany granite form two individual groups. The black and white equigranular biotite granite irregularly outcropping along the margin of the aplite-pegmatite belt forms another group, despite the small volume of exposed rock. Other rocks of the aplite-pegmatite belt are divided into more textural groups, which can gradually change one into another, like for example massive aplites and layered aplites. We distinguish massive aplites, layered aplites, pegmatite layers, megacryst zones, pegmatite pockets, pegmatite dykes and hydrothermal veins within the aplite-pegmatite belt. Some of the differences between the rock types in macroscale were already explained in the previous chapter, but it has to be emphasized, that this rock types can change and be distinguished in the scale of one thin-section. For example the layering of the layered aplites is well recognizable in the microscale, as well as the abrupt change of grain size in the case of pegmatite layers, which can change back to the normal aplitic grain size still in the same thin-section (or do not have to). This is not true for the megacryst zones and pegmatite pockets, which which have too big sizes to fit in one thin-section, there can be only part of them there. Hydrothermal veins are more common outside the aplite-pegmatite belt.

These rock types were distinguished not only for descriptive reasons, but also to better illustrate the possible evolution during crystallization or post-magmatic stages, and to highlight features that are crucial to interpretation of these rocks. We can for example best illustrate the unidirectional solidification textures on pegmatite layers, megacryst zones or pegmatite pockets. These rock types can have also different degrees of chemical evolution, which is important to interpretation in combination with the textures. Therefore we distinguish every rock type, which differ texturally or in modal composition.

3.1 Marginal Říčany granites

The marginal Říčany biotite granite has two varieties – the more abundant strongly porphyritic variety and the equigranular variety from the eastern part of the outcrop area (Fig. 3.1). Both rocks have massive unoriented granitic texture and are composed of quartz (~29-32 vol. %), plagioclase (~17-27 vol. %), K-feldspar (~30-31 vol. %), biotite (~12-20 vol. %), and accessory (less than 2 vol. %) muscovite, zircon, apatite, rutile, xenotime, and monazite. Quartz forms in most cases anhedral grains and often exhibits undulatory extinction. Plagioclase is subhedral typically with rectangular-like cross-section. Plagioclase is frequently poikilitic with muscovite inclusions (generally less than ~0.01 mm, rarely up to ~0.1 mm); individual inclusions concentrate in growth zones or are evenly distributed in the entire poikilocryst. Myrmekites (vermicular intergrowths of plagioclase and quartz) developed along

grain boundaries between plagioclase and quartz, but they are not very often. K-feldspar forms subhedral grains, which can be perthitic (with less than 0.01 mm thin equally oriented albite lamellae or more than 0.01 mm thick also equally oriented lamellae, which are not so dense) and locally shows microcline twinning. Biotite forms euhedral to subhedral flakes with rectangular cross-section, with many pleochroic halos. Muscovite forms mainly the inclusions in plagioclase, or is associated with a biotite grain, and its origin is probably secondary.

Thin section DT 5/2 represents the strongly porphyritic variety of marginal Říčany granite (Fig. 3.1). Grain size varies from ~0.15 mm to ~8 mm (in the macroscale also up to ~2 cm). Phenocrysts up to ~8 mm big are formed by plagioclase, K-feldspar or quartz (they are also in the matrix) and are irregularly distributed, biotite grain size does not vary so much (length 0.5-1.2 mm). Individual phenocrysts are frequently poikilitic, containing irregularly inclusions of all other minerals. Modal proportions in this marginal Říčany granite are slightly different from the equigranular variety – strongly porphyritic variety has less biotite (~12 vol. %) and more plagioclase (~27 vol. %).

Thin section ZV7Cp represents the equigranular variety of marginal Říčany granite (Fig. 3.1). Grain size of all the minerals except accessories varies only from ~0.25 mm to ~2.3 mm (excluding the inclusions of muscovite in plagioclase, which have less than ~0.01 mm in size). Minerals are irregularly distributed in the rock and do not show any orientation, grain boundaries are straight or lobate.

The texture of both varieties of the granite is characteristic of a granite, with mafic phases (e.g. biotite) having bigger degree of euhedrality than leucocratic phases (e.g. quartz). Postmagmatic alterations are minimal (e.g. secondary muscovite), or confined to the proximity of dykes. Few centimeters around aplite dykes in the granite can undergo tourmalinization (tourmaline grows mainly at the expense of biotite).

3.2 Biotite granodiorites

Macroscopically black and white equigranular biotite granodiorite forms a thin unit irregularly outcropping along the margin of the aplite-pegmatite body. It has overall a massive texture with grain size varying from ~0.25 mm to ~3 mm, but there are chains of small quartz grains (grain size 0.01-0.1 mm) along the grain boundaries or along the cracks in grains (up to 0.2 mm thick), locally connected with clusters of biotite (up to 2 mm in size, grain size up to 0.2 mm) (Fig. 3.1). Grain boundaries are commonly straight or curved, but where the chains of small quartz grains are present, there are the grain boundaries lobate. The rock contains locally well-defined biotite-rich enclaves (~44 vol. % of biotite, enclaves typically several cm big) (Fig. 3.1), where grain size diminishes, but texture stays the same, except that biotite is mostly bigger than the rest of the minerals (grain size ~0.05-0.3 mm, biotite legth up to 0.5 mm). The chains of small quartz grains with clusters of biotite can be connected with these enclaves. The biotite granodiorite outside enclaves contains quartz (~29-34 vol. %), plagioclase (~35-40 vol. %), K-feldspar (~13-20 vol. %), biotite (~16 vol. %), and accessory

(less than 2 vol. %) minerals like zircon, apatite, muscovite. It is more plagioclase rich and K-feldspar poor than any variety of marginal Říčany granite. Another major difference is the high degree of euhedrality of the plagioclase grains (with rectangular cross-section). Plagioclase shows quite commonly distinct growth zones. Quartz forms anhedral grains usually smaller than plagioclase or biotite (plagioclase length ~0.5-3 mm, biotite length ~1-2 mm, quartz grain size 0.25-0.7 mm, rarely up to 3 mm), and often shows undulatory extinction. Quartz grains tend to form clusters. Quartz in the chains is anhedral too. K-feldspar forms subhedral grains and can show growth zones too. Biotite outside the enclaves and clusters forms tabular flakes with high degree of euhedrality and rectangular cross-section. It has less pleochroic halos than the biotite from marginal Říčany granite. Biotite from the biotite-rich enclaves and clusters looks similar, is only smaller (length ~0.1-0.5 mm).

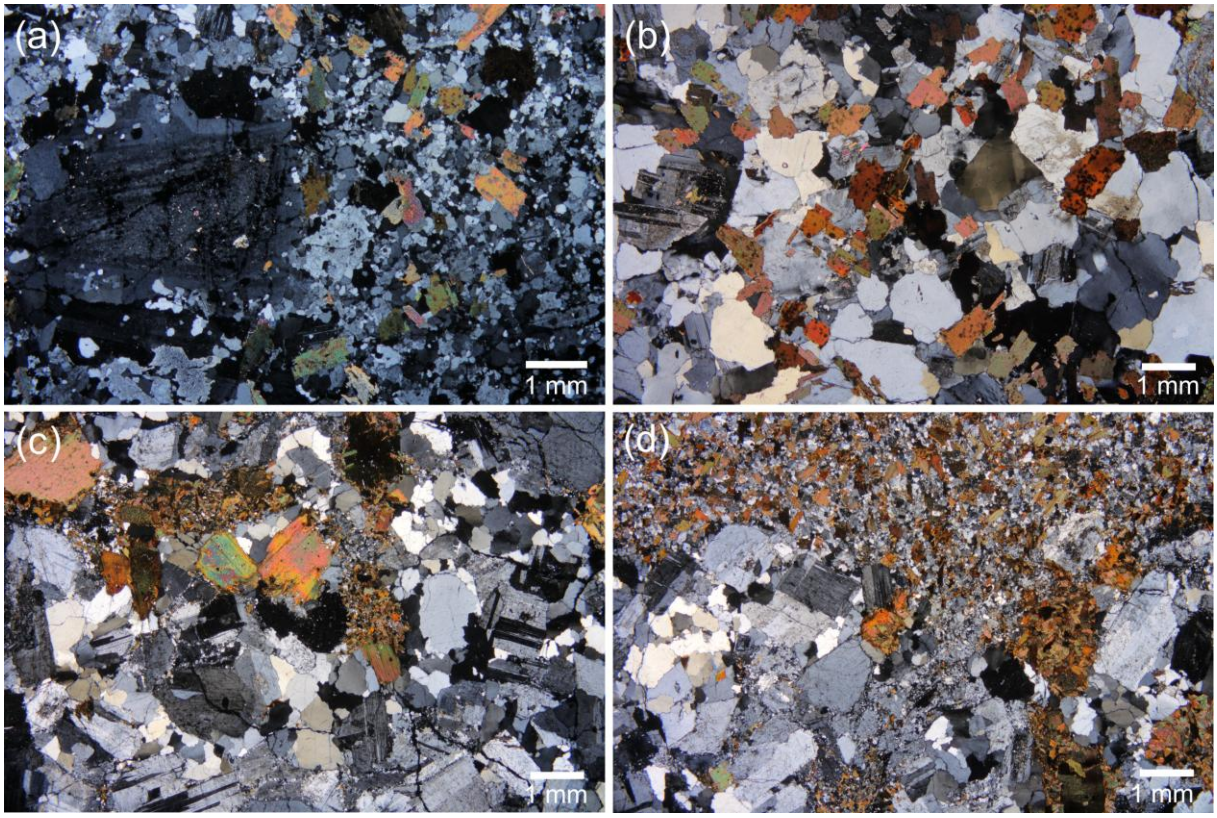

Fig. 3.1 Microphotographs of Říčany granites and biotite granodiorites: (a) thin section DT5/2 - the strongly porphyritic variety of marginal Říčany granite; (b) thin section ZV7C – the equigranular variety of marginal Říčany granite; (c) thin section ZV8A – biotite granodiorite; (d) thin section ZV8B – biotite granodiorite with a biotite-rich enclave.

3.3 Microgranite dykes

The microgranites of the microgranite dykes near Černé Voděrady have various forms. Most often, they are tourmaline-bearing, but they can have also muscovite, biotite, or very rarely garnet (Fig. 3.2). They contain quartz (~35-50 vol. %), K-feldspar (~22-27 vol. %), plagioclase (~13-30 vol. %), tourmaline, muscovite or biotite (~8-15 vol. %), and accessory

garnet, apatite, zircon, cassiterite, xenotime, monazite. They have massive texture, but sometimes are minerals like micas or tourmaline oriented in one direction (with random orientation of feldspars and quartz) (Fig. 3.2 a). The grain size varies usually very much (~0.05-2 mm), but there are no megacrysts, it is more like bigger grains (~0.5-2 mm) surrounded by fine-grained matrix (~0.05-0.1 mm) in the interstitial space or along the grain boundaries (Fig. 3.2 b). Sometimes this matrix is very tourmaline-rich, so the tourmaline forms very fine grains (thin columns with round cross-section vertical to the c axis, with lengths up to ~0.7 mm and approximate diameter of 0.03 mm) in chains along the grain boundaries and this feature is not connected with any bigger phenocrysts of tourmaline. The finer-grained tourmaline can also form very hazy bands. Tourmaline forms always euhedral columns with round or triangular-like cross-section vertical to the c axis, in some microgranite varieties as big as the other grains in the rock (length up to ~0.7 mm). Pleochroic colors parallel to the c axis merge from pale beige to richly brown. The bigger grains of tourmaline can be often zonal with lighter cores than rims. Muscovite forms subhedral flakes with rectangular cross-section as well as biotite (both up to ~1.5 mm long), and garnet forms rarely subhedral grains (grain size ~0.2 mm). Other occurring minerals have the whole range of grain sizes in the rock and do not differ in their features much from the previously described rock types. Plagioclase forms grains with rectangular cross-section with relatively high degree of euhedrality, and can have inclusions of fine-grained muscovite (generally less than ~0.01 mm, rarely up to ~0.1 mm). Myrmekites (vermicular intergrowths of plagioclase and quartz) developed along grain boundaries between plagioclase and quartz, but they are not very often. K-feldspar is subhedral to anhedral and is only rarely and very weakly perthitic. Quartz forms anhedral grains often with undulatory extinction.

3.4 Aplite dykes

Granite aplites of the aplite dykes in marginal Říčany granite are only tourmaline-bearing, without muscovite or biotite. They contain quartz (~25-36 vol. %), K-feldspar (~25-30 vol. %), plagioclase (~33-40 vol. %), tourmaline (~2 vol. % up to ~ 27 vol. % in bands), and accessory minerals (less than ~2 vol. %) like garnet, rutile, zircon, apatite, xenotime, monzonite. They have massive texture with no crystal orientation, the occasional tourmaline banding is purely modal. Grain size varies very much like in microgranite dykes (~0.05-1.5 mm), but there are no phenocrysts surrounded by fine-grained matrix, it varies in space parallel to the dyke margins, or from dyke to dyke. In some bigger dykes (~10 cm widths) exist clear pegmatite layers with crystals up to 2.5 mm big.

Tourmaline forms euhedral to subhedral columns with round or triangular basal sections (as usual). The basal sections have ~0.05-0.2 mm in diameter and lengths up to ~1.5 mm in the aplite (they tend to be finer grained when in a band), but they are usually bigger in the tourmalinization zone around the aplite dyke in granite (basal sections ~1-2 mm in diameter) (Fig. 3.2 d). Pleochroic colours parallel to the c axis merge again from pale beige to richly

brown. The bigger grains of tourmaline can be often zonal with lighter cores than rims. Other minerals do not differ from the previously described. Plagioclase forms subhedral grains with rectangular cross-section, some grains have numerous small muscovite inclusions. K-feldspar is subhedral as well, bigger grains can be perthitic. Quartz is anhedral and usually shows undulatory extinction.

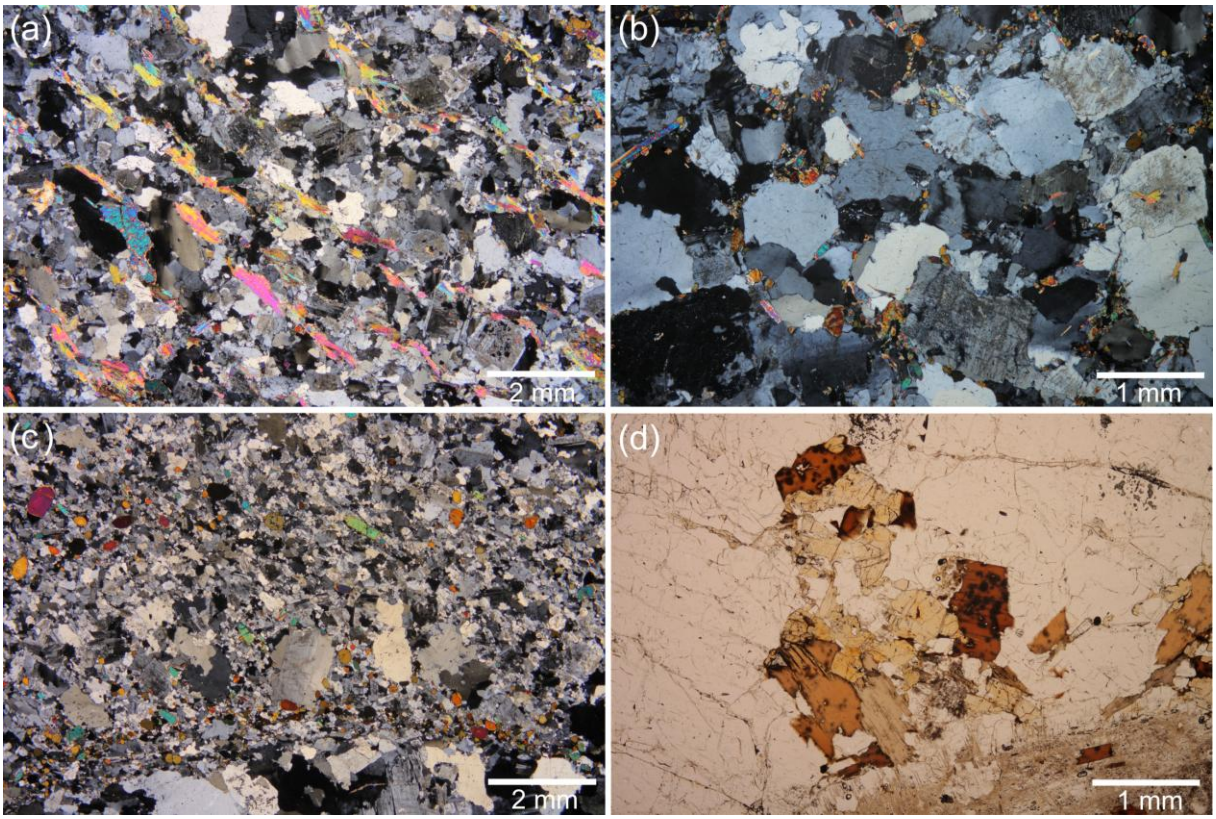

Fig. 3.2 Microphotographs of microgranite and aplite dykes: (a) thin section DT28 – muscovite-, biotite-, and tourmaline-bearing microgranite dyke; (b) thin section DT30 – microgranite dyke with fine-grained interstitial tourmaline; (c) thin section DTX3 – aplite dyke with tourmaline bands; (d) thin section TDX2 – tourmaline replacing biotite in the vicinity of an aplite dyke.

3.5 Massive aplites

Massive granite aplites of the aplite-pegmatite belt are fine-grained rocks (grain size ~0.1-1.5 mm) with massive equigranular texture typical for granites (Fig. 3.3). They contain ~32-35 vol. % of quartz, ~23-28 vol. % of K-feldspar, ~34-39 vol. % of plagioclase, various combinations of tourmaline, biotite and muscovite (~5 vol. % together), and accessory minerals (less than 2 vol. %) like rutile, apatite, ilmenite and xenotime. K-feldspar forms subhedral to anhedral grains, which show in most cases clear microcline twinning, and bigger grains can be slightly perthitic. Quartz looks like usually, it is anhedral and with undulatory extinction. Micrographic intergrowths of K-feldspar and quartz are a far more frequent feature than usually. Also vermicular intergrowths of plagioclase with quartz (myrmekites) are quite frequent. Plagioclase forms otherwise subhedral grains, the grains with bigger degree of

euhedrality have rectangular cross-sections. Tourmaline columns with a high degree of euhedrality are irregularly disseminated in the rock, and they have round basal sections, which are as big as the other minerals (diameter ~0.2-1.5 mm), which means that the columns are usually longer than the normal grain size. Pleochroic colours are usual (from pale beige to richly brown), but the individual grains can be zonal with brown rims and lighter greenish cores and can be alterated along cracks to distinct green to blue zones. Muscovite forms big sheets, which are subhedral, but usually with a high degree of euhedrality, and it is also irregularly disseminated in the rock. Only biotite show clustering, when present.

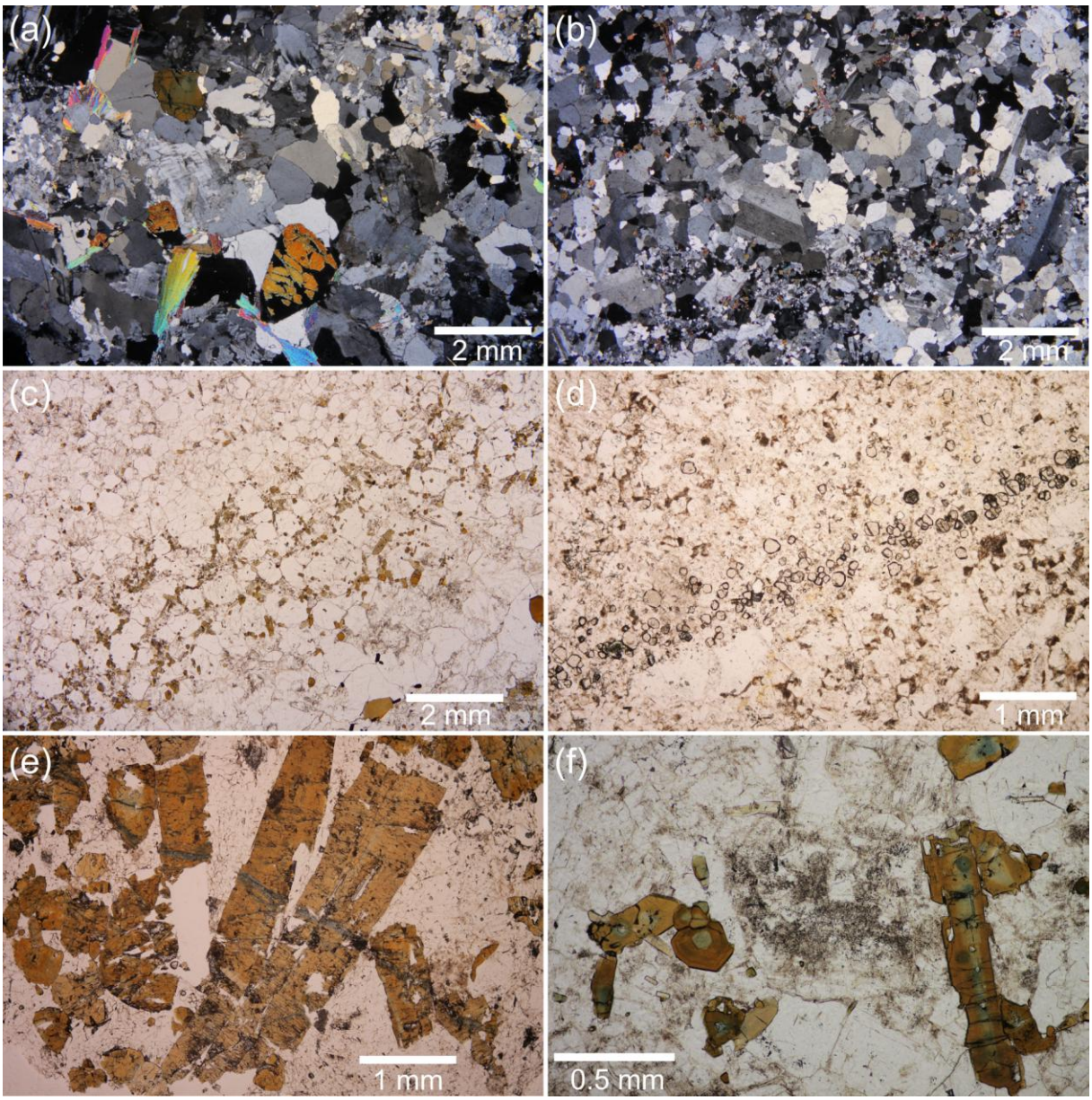

Fig. 3.3 Microphotographs of massive and layered aplites: (a) thin section ZV2A – massive aplite containing dissipated tourmaline and muscovite; (b) thin section DT16A – layered aplite with tourmaline-rich bands; (c) thin section KP – a tourmaline-rich band with interstitial tourmaline in a layered aplite; (d) thin section TJ6B – a garnet-rich band in layered aplite; (e) thin section DT9B – blue alteration veins in tourmaline; (f) thin section TDX2 - blue alteration veins in tourmaline.

3.6 Layered aplites

The main feature of the layered tourmaline aplites in the aplite-pegmatite belt is the alternating of variously thick bands rich in tourmaline (or rarely in garnet) with bands poor in these minerals. The transition between massive and layered aplites is gradual, and in the transition rocks can be also muscovite-rich bands. The minerals in the bands are usually unoriented, the rock has massive, granitic texture (Fig. 3.3). The grain size can be various, it is usually bigger in the transition rocks from massive to layered aplites (~0.2-1.5 mm) than in the typical white-grey layered aplites (~0.05-0.6 mm), but there are no phenocrysts. However, the changes in grain size are only very gradual, not abrupt like in the case of pegmatite layers. The layered aplites contain ~30-35 vol. % of quartz, ~33-40 vol. % of plagioclase, ~21-28 vol. % of K-feldspar, various proportions of tourmaline (up to ~15 vol. %), muscovite or garnet, and accessory minerals (less than ~2 vol. %) like zircon, apatite, columbite/tantalite, monazite, or beryl. Tourmaline forms euhedral to subhedral columns with round basal sections as usual, but it is more fine-grained (up to ~0.05 mm long and ~0.02-0.05 mm thick columns) in the tourmaline-rich bands, where he can "fill up" the interstitial space of other mineral grains forming "chains" of small tourmaline grains along the grain boundaries (Fig. 3.3 c). This fine-grained tourmaline has pleochroic colours from dark bluish grey to light grey, and it is unzonal. The usually more coarse-grained (up to ~0.4 mm thick columns) tourmaline in the tourmaline-poor bands has pleochroic colours as usual - from pale beige to richly brown; and can be zonal with lighter brown cores than rims. Garnet bands are usually far thinner (~0.5-0.7 mm thick) and better defined (denser and more straight) than the tourmaline bands, they are formed by ~0.05-0.2 mm big round euhedral garnet grains (Fig. 3.3 d). Similar grains of garnet can be also disseminated in the rock together with tourmaline. Muscovite can be also disseminated in the rock together with tourmaline, where it forms flakes with rectangular cross-section and high degree of euhedrality (~0.2-2 mm long), or it can form muscovite-rich bands too. Other minerals do not differ from the other rock types much. Feldspars are subhedral and quartz has the lowest degree of euhedrality. The abundance of microclinic twinning and perthitic lamellae in K-feldspar differs from place to place. Myrmekites can occur.

3.7 Pegmatite layers in layered aplites

We define a pegmatite layer as a layer concordant to the modal layering in the layered aplites, where the grain size change abruptly and is relatively bigger than the grain size of the surrounding aplite. However, the grain sizes (~0.1-X mm), or the widths (~3-X0 mm) of this layers can be various. The c axis of elongated grains of minerals is usually perpendicular to the direction of the "plane" of the layer, or to the layering in the surrounding aplite (Fig. 3.4 b,e), indicating comb texture, which is one of the unidirectional solidification textures. Some of the bigger phenocrysts can extend from the pegmatite layer into the layered aplite (as described in the geological setting chapter), but it is not very often and not very obvious in the

microscale. In some cases one side of the pegmatite layer tightly borders with some distinct and straight mineral-rich layer (most often tourmaline-rich, but also garnet- or cassiterite-rich layer), and the minerals of the pegmatite layer appear to have nucleated at the margin of this modal band. On the other side of the pegmatite layer can be a modal band too, but it is usually not so straight and distinct, it copies this uneven margin of the pegmatite layer with some bigger megacrysts extending from the layer (Fig. 3.4 a).

Modal composition of these layers can vary too, but they are usually feldspar- and quartz-rich (~33-40 vol. % of quartz, ~21-26 vol. % of plagioclase and ~34-40 vol. % of K-feldspar), other minerals such as tourmaline, garnet or muscovite occur in various proportions and combinations, usually up to ~3 vol. %. K-feldspar grains are subhedral, frequently perthitic with microcline twinning and occasionally flaring (elongated, fan-like, with one end narrow and sharp – there has the growth began – and the other wide and curved). Plagioclase forms lathy subhedral grains and most clearly exposes the comb texture. Some of the grains can be also narrower on one end and wider on the other, resembling the flaring megacrysts of K-feldspar. Small plagioclase grains (grain size ~0.05-0.2 mm) rarely nucleate at the cracks or along the margins of bigger K-feldspar grains. Quartz is anhedral and with undulatory extincition, as is common. Tourmaline can form rare megacrysts (diameter of the basal section ~1 mm or bigger) as big as the other grains in the pegmatite layer, or also as small grains as are in the surrounding aplite (diameter of the basal section down to ~0.03 mm). Both of them are euhedral columns with round basal sections, which have pale beige to richly brown pleochroic colours and the bigger ones are usually zonal with darker rims than cores, or several alternating darker and lighter zones. Garnet grains are as big as the other grains in the pegmatite layer (grain size ~1 mm or bigger) when occurring, forming euhedral round megacrysts. Muscovite occurs usually in the pegmatite layers within the pinkish transitional aplites from layered to massive aplites, forming flakes with elongate rectangular cross-section and relatively high degree of euhedrality. It can expose comb textures as well, or the individual flakes are oriented so, that they have flaring shape.

3.8 Megacryst zones

Megacryst zones occur in the relatively most fine-grained (grain size ~0.01-0.5 mm) homogeneous tourmaline aplites from the whole aplite-pegmatite belt (Fig. 3.4 g). These aplites have massive granitic texture, the grain sizes vary irregularly and the minerals are distributed irregularly. They contain quartz (~29-35 vol. %), plagioclase (~31-40 vol. %), K-feldspar (~22-35 vol. %), tourmaline (~4-5 vol. %), and accessory minerals (less than 2 vol. %) like muscovite, beryl, zircon, apatite, cassiterite and monazite. The minerals look similarly like in other aplites – quartz is anhedral, K-feldspar is anhedral to subhedral (no perthites, but occasionally with microcline twinning), plagioclase is subhedral and lathy, tourmaline forms subhedral to euhedral columns with round basal sections and pale beige to richly brown pleochroic colours, some of them can have lighter cores than rims.

The megacryst zones are characterized by a very abrupt change of grain size (relatively to the fine-grained aplites), which can evolve toward even bigger grain size from the margin toward the center of the megacryst zone (grain size typically ~0.7-X mm) (Fig. 3.4 g). They contain ~31-33 vol. % of quartz, ~22-33 vol. % of plagioclase, ~24-31 vol. % of K-feldspar, up to ~20 vol. % of tourmaline, but that is various, tourmaline concentration is often bigger in the marginal areas of the megacryst zone. You can see the proportions of the minerals are varying, but there is a tendency toward smaller proportion of plagioclase and bigger proportion of tourmaline relatively to the surrounding fine-grained aplite. The orientation of elongated minerals (comb layers) is more obvious in the macroscale than in the microscale, because only the big megacrysts are oriented. There is nothing extraordinary in the appearance of feldspars and quartz – quartz is the most anhedral mineral, plagioclase is subhedral and lathy and K-feldspar is anhedral to subhedral and the big grains are perthitic and can have small (up to ~0.1 mm long) flakes of mica nucleating along the cracks in it. Tourmaline forms big euhedral megacrysts (up to several millimetres long and ~2 mm wide columns with round basal sections) as well as grains smaller than the majority of the grains in the megacryst zone (diameter of the basal section down to ~0.05 mm) (Fig. 3.4 h). The pleochroic colours of tourmaline are as usual – pale beige to richly brown, and the big megacrysts are zonal with lighter cores than rims (or several transitional colours alternating in zones between), and they can be altered along cracks to bluish pleochroic colour.

3.9 Pegmatite pockets

Pegmatite pockets are characterized by their huge grain size (up to several centimetres) (Fig. 3.4). Therefore is the study of modal proportions in the microscale very restricted, but we can say that the proportion of K-feldspar is usually high (more than ~34 vol. %), although there tend to be zones of feldspar grains, zones of plagioclase grains etc. Even the flaring feldspar megacrysts are included into this group. Other minerals occurring in the pegmatite pockets are quartz, tourmaline, muscovite, minor biotite and accessory rutile. Graphic intergrowths of K-feldspar and quartz are a common phenomenon in the pegmatite pockets (Fig. 3.4 d). Big subhedral K-feldspar grains are in most cases perthitic, some of them expose microcline twinning. Plagioclase is subhedral and lathy as usual and quartz is anhedral. Tourmaline forms big euhedral columns with round basal sections (diameter of the basal sections is several millimetres) and pale beige to richly brown pleochroic colours, and is zonal with lighter cores than rims. Muscovite forms flakes with high degree of euhedrality and elongated rectangular cross-sections, which are usually at the margin of the pegmatite pocket and can be oriented perpendicularly to the margin, which again resemble the comb textures (Fig. 3.4 e). Biotite forms only rare inclusions in the muscovite grains.

The flaring feldspar megacrysts have micrographic texture and there is ~60 vol. % of K-feldspar and ~40 vol. % of quartz. A very rare anhedral tourmaline occurs between the grains (grain size 0.X mm). It has pale beige to paler brown pleochroic colours.

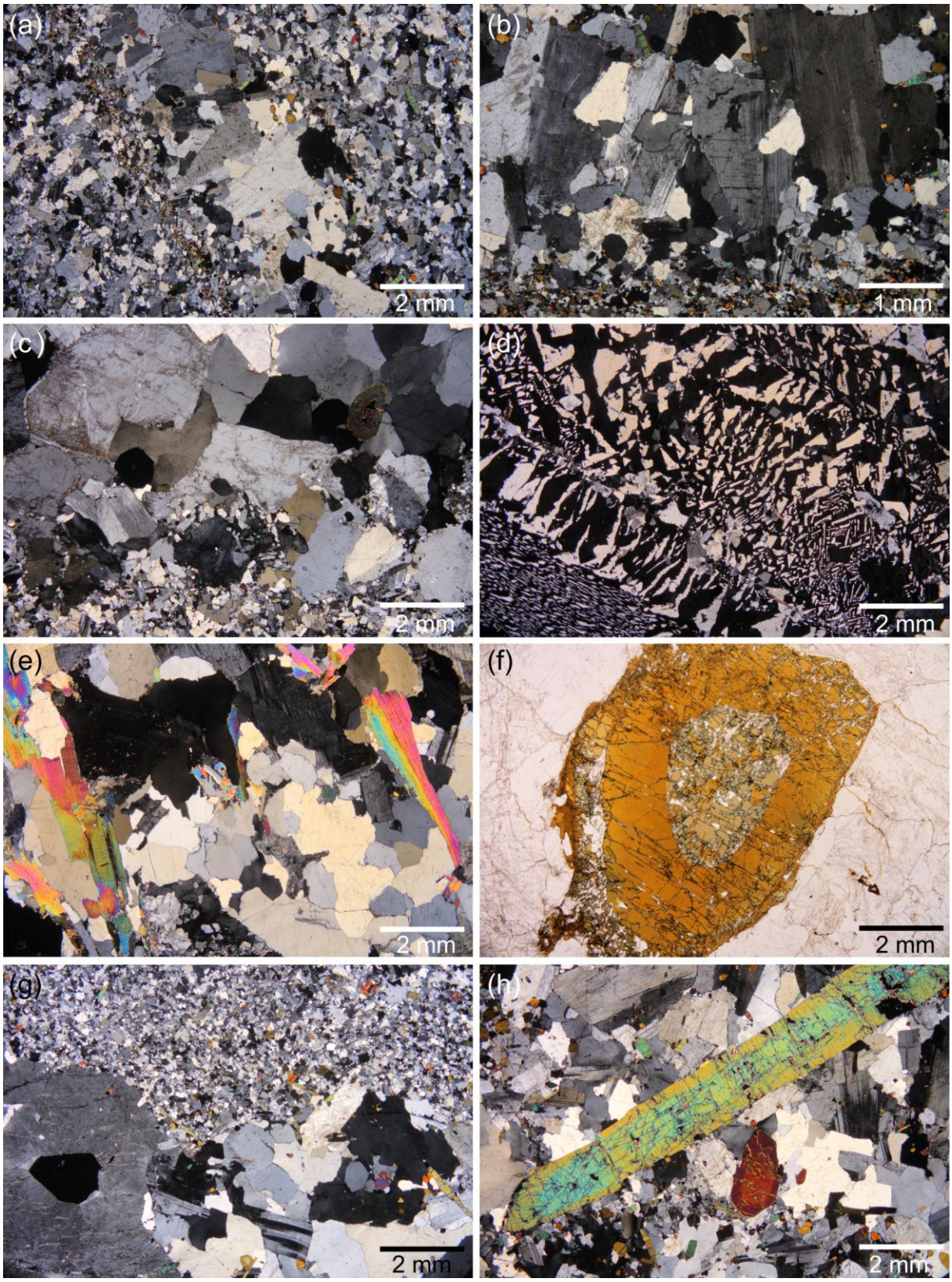

Fig. 3.4 Microphotographs of pegmatite layers, megacryst zones, and pegmatite pockets: (a) thin section DT19 – pegmatite layer rimmed by tourmaline-rich bands on both sides; (b) thin section DT19 – unidirectional solidification textures (comb layer) within the pegmatite layer; (c) thin section TD2 – a pegmatite layer with occasional tourmaline and garnet megacrysts; (d) thin section DT10 – graphic texture in a pegmatite pocket; (e) thin section ZV3A – comb muscovite in a pegmatite pocket; (f) thin

section ZV10A – zonal tourmaline megacryst in a pegmatite pocket; (g) thin section DT20/3 – megacryst zone; (h) thin section DT20/1 – zonal tourmaline megacryst in a megacryst zone.

3.10 Pegmatite dykes

Pegmatite dykes in aplites are characterized also by an abrupt change of grain size like pegmatite layers, but they are discordant to layering, they clearly intersect it. The grain size is relatively bigger than the grain size of the surrounding aplite, but can be various (~0.5 to several millimetres), as well as the width of these dykes (~3 mm to several centimetres). The minerals are unoriented in these dykes, but the dykes can be zonal. There is often a feldspar margin and quartz core, but these zones can alternate and exist in various proportions. Some of the dykes have a plagioclase-rich zone along their margin ("sugar zone"), which is finer-grained than the surrounding aplite (Fig. 3.5 b). The grain size grows within this layer from the well-defined margin bordering with the pegmatite dyke (grain size down to ~0.03 mm) towards the outer more distant margin (grain size up to ~0.3 mm), where this layer gradually verges into the surrounding aplite. Apart from plagioclase there can be minor equally fine-grained tourmaline. On the boundary between pegmatite dyke and sugar zone occur abundant interesting minerals like garnet, muscovite, tourmaline, topaz, beryl or rutile.

Pegmatite dykes contain in general quartz, K-feldspar and plagioclase as main minerals and tourmaline, garnet, muscovite, beryl, topaz, rutile, cassiterite, apatite and columbite/tantalite as accessory minerals (in various proportions). K-feldspar is subhedral to euhedral and the big grains are commonly perthitic with occasional inclusions of small (0.0X-0.X mm big) plagioclase and quartz grains. Plagioclase is lathy and subhedral and in most cases fine-grained as part of the sugar zone, or nucleating along the margins and cracks in big K-feldspar grains (this plagioclase grain size ~0.02-0.5 mm). Quartz is anhedral and shows undulatory extinction, as usual. Tourmaline is an unusual mineral in these dykes and occurs mainly at the boundary of the pegmatite dyke and the sugar zone, where it forms unusual anhedral to subhedral grains (they resemble columns with round basal sections) with pale yellow-green to dark yellow-green pleochroic colours and darker cores than rims. Rare tourmaline grains within the dyke can be found in the areas where the dyke cross-cutes a tourmaline band, and these tourmalines look like the ones in the band. Garnet forms ~1 mm big round euhedral grains mostly at the boundary of the pegmatite dyke and the sugar zone (Fig. 3.5 c), or at the boundary of the sugar zone and the surrounding aplite. Muscovite as well occurs mostly at the boundary of the pegmatite dyke and the sugar zone, forming euhedral flakes with rectangular cross-section (~1-2 mm long). Beryl forms euhedral to subhedral columns with round basal sections, up to ~3 mm long and ~1 mm wide.

3.11 Hydrothermal veins

Hydrothermal veins within the aplite-pegmatite belt are composed exclusively of ~0.2-2 mm big subhedral quartz grains (Fig. 3.5 d). They are typically 1-2 cm wide and crosscut the

textures in aplites. Hydrothermal veins outside the aplite-pegmatite belt are composed of quartz too (it is similar, but can be bigger – up to ~5 mm big), and tourmaline. This tourmaline forms subhedral to euhedral columns with round basal sections (~0.01-0.5 mm wide), which have light blue cores and richly brown to beige rims (pleochroic colours) (Fig. 3.5). This tourmaline is highly localized (the veins are zonal) and the biggest and most euhedral tourmaline is usually at the margin of the vein, and its c axis is perpendicular to the margin of the vein (some grains can extend from the vein). The abundance of tourmaline in these veins is high, in some zones forms tourmaline 100 vol. % of the rock.

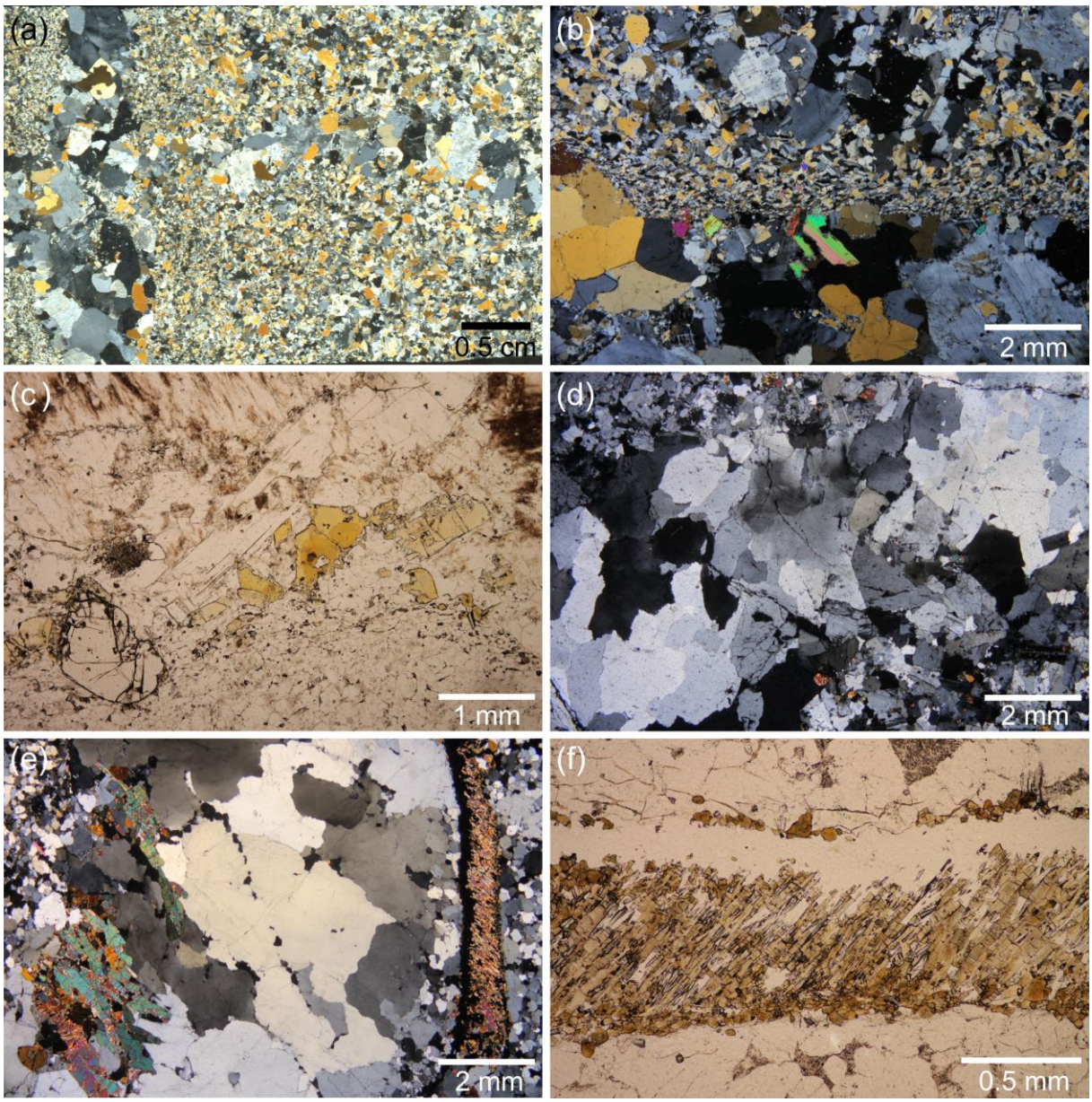

Fig. 3.5 Microphotographs of pegmatite dykes and hydrothermal veins: (a) thin section TJ19B – pegmatite dyke; (b) thin section TJ22A – pegmatite dyke and sugar zone next to it; (c) thin section TJ22A – garnet, tourmaline, muscovite, and topaz megacrysts at the boundary of the pegmatite dyke and the sugar zone; (d) thin section DT2/1 – hydrothermal vein in aplite; (e) thin section ZV11A – quartz-tourmaline hydrothermal vein in xenoliths; (f) thin section ZV11A – hydrothermal tourmaline.

4 Mineral chemistry

4.1 Analytical methods

Minerals were analyzed in polished thin sections using the Vega TESCAN electron microscope equipped with the X-Max 50 EDS detector (system INCA Oxford), hosted at the Institute of Petrology and Structural Geology, Charles University in Prague. Accelerating voltage of 15 kV, probe current of 1.5 nA and counting time 100 s were used. Beam diameter was 3 μm for all minerals but plagioclase, where the signal was recorded during scanning of an area 5 x 5 μm in order to minimize sodium loss.

Standarts for analyzed elements were (S = synthetic, N = natural): F - fluortopaz (N), Na - albite (N), Mg - periclase (S), Al - Y-Al garnet ($Y_3Al_5O_{15}$) (S), Si - sanidine (N), P - apatite (N), Cl - tugtupite (N), K - sanidine (N), Ca - wollastonite (N), Ti - rutile (S), Cr - Cr_2O_3 (S), Mn - rhodonite (N), Fe - haematite (N), Co - Co (S), Ni - pentlandite (N), Cu - Cuprite - Cu_2O (S), Zn - Sphalerite (S), As - GaAs (S), Sr - Celestine (S), Y - $Y_3Al_5O_{12}$ (S), Zr - Zircon (S), Nb - Nb (S), Sn - cassiterite (N), Cs – Pollucite, Ba – Barite, La - $LaPO_4$ (S), Ce - $CePO_4$ (S), Nd - $NdPO_4$ (S), Sm - $SmPO_4$ (S), Eu - $EuPO_4$ (S), Gd - $GdPO_4$ (S), Dy - $DyPO_4$ (S), Er - $ErPO_4$ (S), Yb - $YbPO_4$ (S), Hf - Hf (S), Ta - $KTaO_3$ (S), W – Scheelite, Pb - Pb (S).

4.2 Feldspars

Feldspars form megacrysts or individual grains in the matrix in all rock types. K-feldspar grains are either homogeneous or undergone exsolution, with perthite lamellae (Fig. 4.2). Crystallochemical formulas were calculated on 8 oxygen basis assuming that iron is present in ferrous form.

All K-feldspar grains are rather pure, with 3.1-14.4 mol. % albite and up to 0.7 mol. % anorthite (Fig. 4.2; Tab. 4.1). The concentrations of Ba, Cs, Sr and Rb remain below the respective detection limits (2σ = 0.16-0.18 wt. % BaO, 2σ = 0.14-0.15 wt. % Cs_2O, 2σ = 0.14 wt. % SrO, 2σ = 0.13 wt. % Rb_2O); elevated concentrations of Cs (0.17 wt. % Cs_2O, 0.003 Cs pfu) and of Ba (0.32-0.37 wt. % BaO, 0.006-0.007 Ba pfu) are rare, and are in the more coarse-grained parts. The phosphorous concentrations are often close or slightly above the detection limit (2σ = 0.04-0.09 wt. % P_2O_5, 0.002–0.006 P pfu). Perthitic K-feldspar grains do not show any significant and systematic depletion in the albite end-member (Fig. 4.1). The exsolution lamellae in the perthitic K-feldspar grains have up to 2.6 mol. % anorthite and 0.4-7.4 but generally 0.4-2.3 mol. % orthoclase.

Plagioclase is albite-rich, with up to 15.4 but generally less than 10.7 mol. % anorthite (the distribution has maximum in the lowest values) and up to 7.4 but generally less than 2 mol. % orthoclase (Fig. 4.1; Tab. 4.1). There is no correlation trend between the anorthite and orthoclase end-member in plagioclase. The concentrations of Ba, Cs, Sr and Rb are all below

their detection limits (2σ = 0.16-0.18 wt. % BaO, 2σ = 0.15 wt. % Cs_2O, 2σ = 0.14 wt. % SrO, 2σ = 0.13 wt. % Rb_2O). In about quarter of analysed grains, the phosphorous concentrations exceed the detection limit (2σ = 0.04-0.09 wt. % P_2O_5) and they reach 0.002–0.005 P pfu.

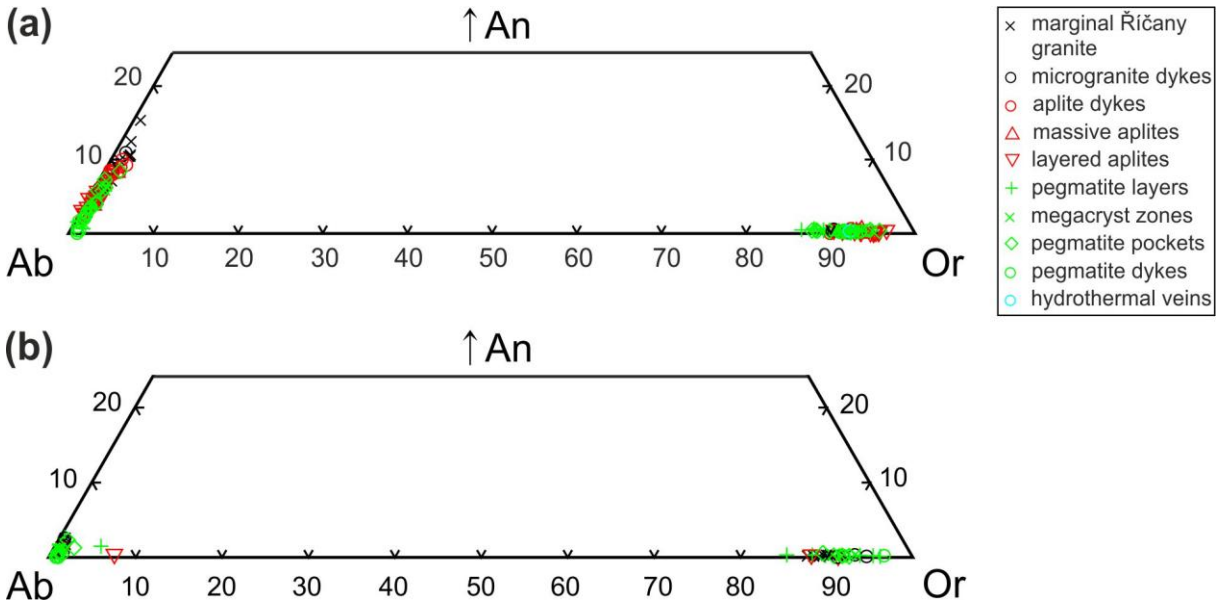

Fig. 4.1 Feldspar molar compositions. An – anorthite end member, Ab – albite end member, Or – orthoclase end member. (a) Homogeneous K-feldspars and plagioclases. (b) Perthitic K-feldspars with their plagioclase lamellae.

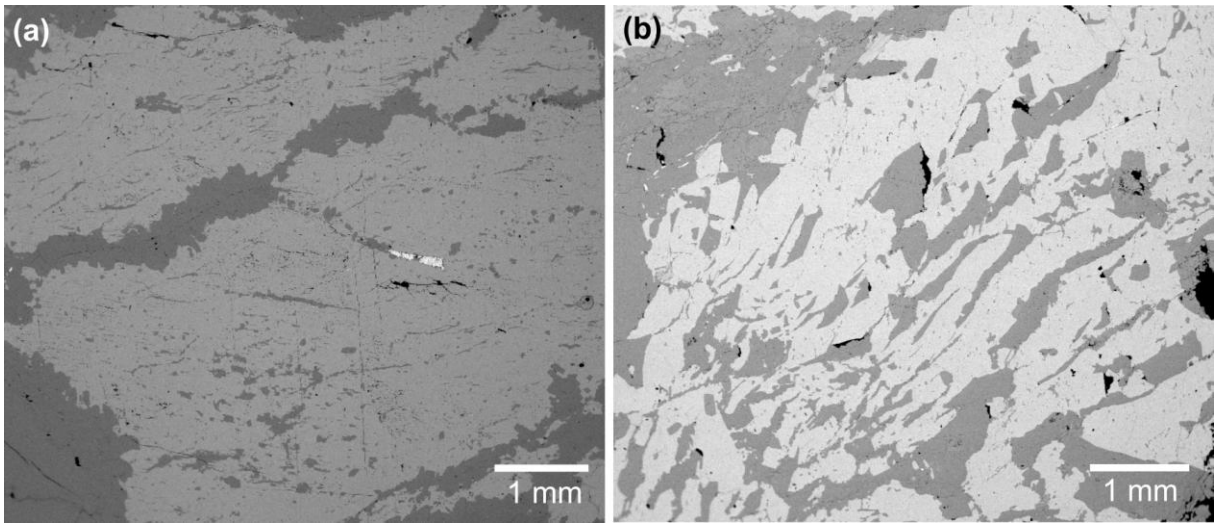

Fig. 4.2 Microphotographs of feldspars in back-scattered electrons. (a) Perthitic K-feldspar with late plagioclase vein from the sample TD2 (pegmatite layers). (b) Micrographic K-feldspar with slightly perthitic rim from the sample DT10 (pegmatite pockets).

The K-feldspar and plagioclase composition changes systematically with a degree of differentiation and textural evolution. However, the transitions between the groups of samples representing different melts are gradual, the groups overlap and different melts can be

recognized even in one thin section (Fig. 4.1; Fig. 4.3). In the marginal Říčany granite, K-feldspar has 9.9-10.6 mol. % albite and up to 0.5 mol. % anorthite, plagioclase contains 4.6-10.7 mol. % anorthite and 0.7-2.0 mol. % orthoclase. Plagioclase grains have overgrowths that are slightly depleted in the anorthite end-member by 3-5 mol. % and in the orthoclase end-member by 1 mol. %.

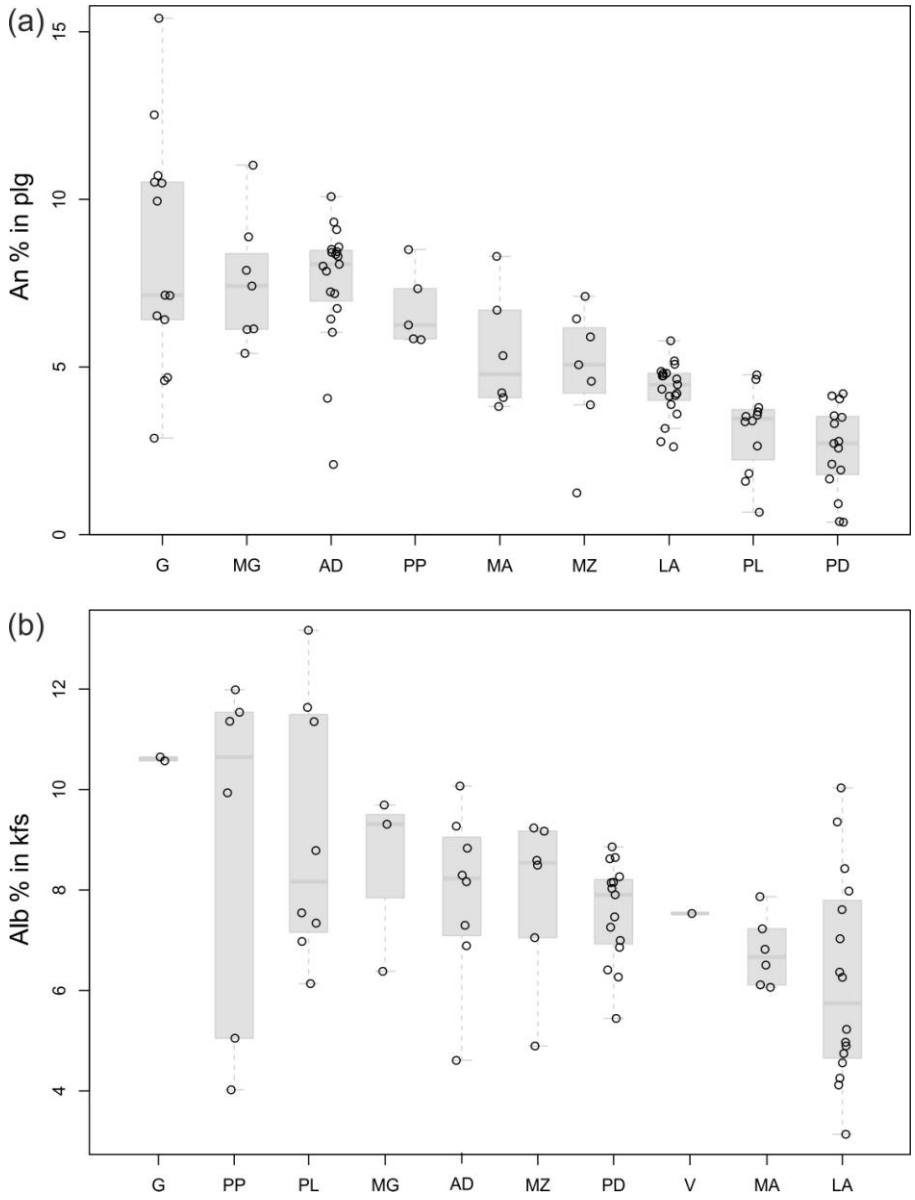

Fig. 4.3 Feldspar molar compositions in the rock groups. (a) Proportion of the anorthite component in plagioclase. (b) Proportion of the albite component in K-feldspar. The values are depicted for each rock group with a boxplot showing the median, two quartiles, and outlying values. Abbreviations: AD – aplite dykes, G – Říčany granite, LA – layered aplites, MA – massive aplites, MG – microgranite dykes, MZ – megacryst zones, PD – pegmatite dykes, PL – pegmatite layers, PP – pegmatite pockets, V – veins.

Aplite and microgranite dykes often have their plagioclase compositions similar to that of the marginal Říčany granite (2.1-11.0 mol. % anorthite; Fig. 4.3). The orthoclase end-

member in plagioclase reaches similar values in every sample and does not exceed 2 mol. %, therefore we will focus only on the anorthite end-member in plagioclase. Plagioclases from the massive aplites are slightly depleted in the anorthite end-member (3.8-8.3 mol. % anorthite) in comparison with the marginal Říčany granite. The same applies to megacryst zones and aplites around them, which are very fine-grained and macroscopically grey (4.6-7.1 mol. % anorthite) and for the pegmatite pockets samples (5.8-8.5 mol. % anorthite). Plagioclases from layered aplites and pegmatite layers in aplites are depleted in the anorthite end-member a bit more (2.6-5.8 mol. % anorthite). Plagioclases from the pegmatite dykes in aplites have 1.7-4.2 mol. % anorthite. Probably very late melt forms plagioclase veins in bigger K-feldspar grains in various samples with plagioclase grains which have up to 3.9 but generally less than 2.0 mol. % anorthite. Plagioclase grains which form exsolution lamellae in the perthitic K-feldspar grains have up to 2.6 mol. % anorthite. Rims of plagioclase grains tend to be slightly depleted in the anorthite and orthoclase end-members only in aplite and microgranite dykes, but not so clearly as in the Říčany granite.

Tab. 4.1 Representative chemical composition of feldspars.

Sample	DT5/2	DT5/2	DTX3	DTX3	ZV2A	ZV2A	TJ6A	TJ6A	DT10
Analysis	4	1	40	54	27	24	3	18	20
Group	G	G	AD	AD	MA	MA	LA	LA	PP
mineral	kfs	plg	kfs	plg	kfs	plg	kfs	plg	plg
type	hom.	hom.	hom.	hom.	hom.	hom.	perth.	hom.	perth.
SiO_2 (*wt. %*)	64.915	65.216	64.627	65.677	64.696	66.303	65.268	66.639	67.739
Al_2O_3	18.665	21.665	18.709	21.244	18.738	20.448	18.742	20.085	19.295
CaO	0.100	2.294	0.134	1.976	*n.d.*	1.125	*n.d.*	0.706	*n.d.*
Na_2O	1.185	10.339	0.799	10.361	0.859	10.950	0.498	11.106	11.462
K_2O	15.149	0.352	15.383	0.392	15.293	0.122	16.091	0.152	0.161
P_2O_5	*n.d.*	0.054	*n.d.*	*n.d.*	0.123	*n.d.*	*n.d.*	*n.d.*	*n.d.*
Total	100.109	100.000	99.703	99.691	99.789	99.007	100.671	98.794	98.710
P (*per 8 O*)	-	0.002	-	-	0.005	-	-	-	-
Si	2.987	2.873	2.986	2.896	2.984	2.934	2.992	2.953	2.996
Al	1.013	1.125	1.019	1.104	1.019	1.067	1.013	1.049	1.006
Ca	0.005	0.108	0.007	0.093	-	0.053	-	0.034	-
Na	0.106	0.883	0.072	0.886	0.077	0.939	0.044	0.954	0.983
K	0.889	0.020	0.907	0.022	0.900	0.007	0.941	0.009	0.009
Total	5.000	5.011	4.990	5.002	4.984	5.000	4.990	4.998	4.994
An (*mol. %*)	0.491	10.708	0.675	9.322	0.000	5.336	0.000	3.366	0.000
Ab	10.572	87.334	7.268	88.477	7.867	93.973	4.493	95.771	99.086
Or	88.937	1.958	92.058	2.201	92.133	0.690	95.507	0.863	0.914
Total	100.000	100.000	100.000	100.000	100.000	100.000	100.000	100.000	100.000

n.d. – below detection limit, kfs-K-feldspar, plg – plagioclase, hom. – homogeneous grain, perth. – perthitic K-feldspar or plagioclase lamellae in it, G – Říčany granite, AD – aplite dykes, MA – massive aplites, LA – layered aplites, PP – pegmatite pockets

Aplite and microgranite dykes have also their K-feldspar compositions similar to that of the marginal Říčany granite, although their ranges of the albite end-member in K-feldspar can be broader and reach lower values (4.6-10.0 mol. % albite). K-feldspars from granite in the surroundings of the aplite dykes can be enriched in the albite component (11.3-12.1 mol. % albite), which is accompanied by higher Ba-feldspar values (0.6-0.7 mol. % Ba-feldspar). The anorthite end-member in K-feldspar reaches similar values in every sample and does not

exceed 0.7 mol. %, therefore we will focus only on the albite end-member in K-feldspar. K-feldspar in massive aplites has 6.1-7.9 mol. % albite and similar ranges of the albite end-member in K-feldspar are also in pegmatite dykes in aplites (6.3-8.9 mol. % albite). Other samples (layered aplites, pegmatite layers, megacryst zones and pegmatite pockets) have often broad range of K-feldspar compositions often including the Říčany granite K-feldspar composition (3.1-12.0 mol. % albite). K-feldspar from the pegmatite layer in sample TD2 and from the sample ZV3A from a pegmatite pocket is enriched in the albite end-member (9.9-14.4 mol. % albite) in comparison with the Říčany granite K-feldspar. Perthitic K-feldspar grains have various compositions in a range corresponding the sample they are from. They do not show any significant and systematic depletion in the albite end-member. There is no systematic compositional zonation of K-feldspar grains either.

4.3 Biotite

Biotite is a common mafic constituent in the marginal Říčany granite but it is much more rare in all other intrusive units. It has been found in microgranite dykes, massive aplites, and pegmatite pockets. Crystallochemical formulas were calculated on the basis of 11 oxygen atoms and by assuming the all iron is present in the ferrous form (Tab. 4.2). Lithium is assumed to be absent in micas, as confirmed by whole-rock geochemical data.

Biotites can be classified as phlogopites and siderophyllites (Fig. 4.4) with 16.4-21.4 wt. % total Al_2O_3 (1.5-2.0 Al pfu) and from 2.0-10.7 wt. % MgO (0.2-1.2 Mg pfu). To octahedral site belongs 0.4-0.9 $^{[6]}$Al pfu and all Mg, 0.9-1.5 Fe pfu (14.6-22.2 wt. % FeO), 0.02-0.09 Mn pfu (0.3-1.3 wt. % MnO), and 0.10-0.18 Ti pfu (1.74-3.00 wt. % TiO_2). Tetrahedral site is occupied by 2.8-2.9 Si pfu, 1.1 – 1.2 $^{[4]}$Al pfu. Interlayer site is occupied mainly by potassium (0.9-1.0 K pfu, 9.0-10.0 wt. % K_2O), Na_2O and CaO concentrations are near their detection limits (2σ = 0.04-0.08 wt. % Na_2O, 2σ = 0.06 wt. % CaO), reaching no more than 0.02 Na pfu and 0.01 Ca pfu. Cs_2O concentrations remain below the detection limit (2σ = 0.14-0.15 wt. % Cs_2O), elevated concentrations are rare (0.2-0.7 wt. % Cs_2O, up to 0.02 Cs pfu). F concentrations are 1.1-2.3 wt. % F (0.3-0.6 F pfu) and all Cl is below the detection limit (2σ = 0.04 wt. % Cl).

Biotite from individual intrusive units differs mainly in element concentrations at octahedral site, that is Mg, Fe, Mn and $^{[6]}$Al, and in F and OH concentrations, we use also *fe#* (molar $Fe^{2+}/[Mg+Fe^{2+}]$), *mn#* (molar $Mn/[Fe^{2+}+Mn]$) (Fig. 4.5). Biotite from marginal Říčany granite has 1.1-1.3 Mg pfu, 0.9-1.4 Fe pfu, 0.02-0.05 Mn pfu, 0.38-0.44 $^{[6]}$Al pfu and 0.3-0.6 F pfu, which gives us *fe#* of 0.44-0.50 and *mn#* of 0.02-0.05. The rims of grains in the marginal Říčany granite tend to be slightly enriched in Cs, but that is the only compositional zonation for grains. The biotite grains in the Říčany granite near aplite dykes tend to be slightly enriched in Mn and depleted in Mg. Biotite from microgranite dykes has 0.3-0.4 Mg pfu, 1.2-1.3 Fe pfu, 0.07-0.09 Mn pfu, 0.73-0.85 $^{[6]}$Al pfu and no F pfu, which gives us *fe#* of 0.78-0.81 and *mn#* of 0.05-0.06. Biotitie from massive aplites has 0.7-0.8 Mg pfu, 1.2-1.3 Fe

pfu, 0.05-0.06 Mn pfu, 0.53-0.56 $^{[6]}$Al pfu, no F pfu, *fe#* of 0.60-0.66 and *mn#* of 0.04-0.05. Biotite from pegmatite pockets forms rare grains with unusual thin long habitus or is enclosed in muscovite (Fig. 4.6). The biotite with unusual thin long habitus from sample DT10 is depleted in Mg (0.8 Mg pfu), enriched in Fe (1.2 Fe pfu), enriched in Al (0.5 $^{[6]}$Al pfu) and has similar concentrations of Mn, Ti and F to marginal Říčany granite (0.03 Mn pfu, 0.14 Ti pfu and 0.50 F pfu). It has *fe#* of 0.61 and *mn#* of 0.02. The biotite enclosed in muscovite from sample ZV3A is depleted in Mg (0.2 Mg pfu), enriched in Fe (1.4-1.5 Fe pfu), enriched in Al (0.7 $^{[6]}$Al pfu), enriched in Mn (0.08 Mn pfu), slightly enriched in Ti (0.17 Ti pfu) and depleted in F (0.3 F pfu). It has *fe#* of 0.83 and *mn#* of 0.06**.** Both of them tend to be slightly enriched in Cs and have slightly bigger vacancies in octahedral and interlayer sites. There is no compositional zonation in these biotites.

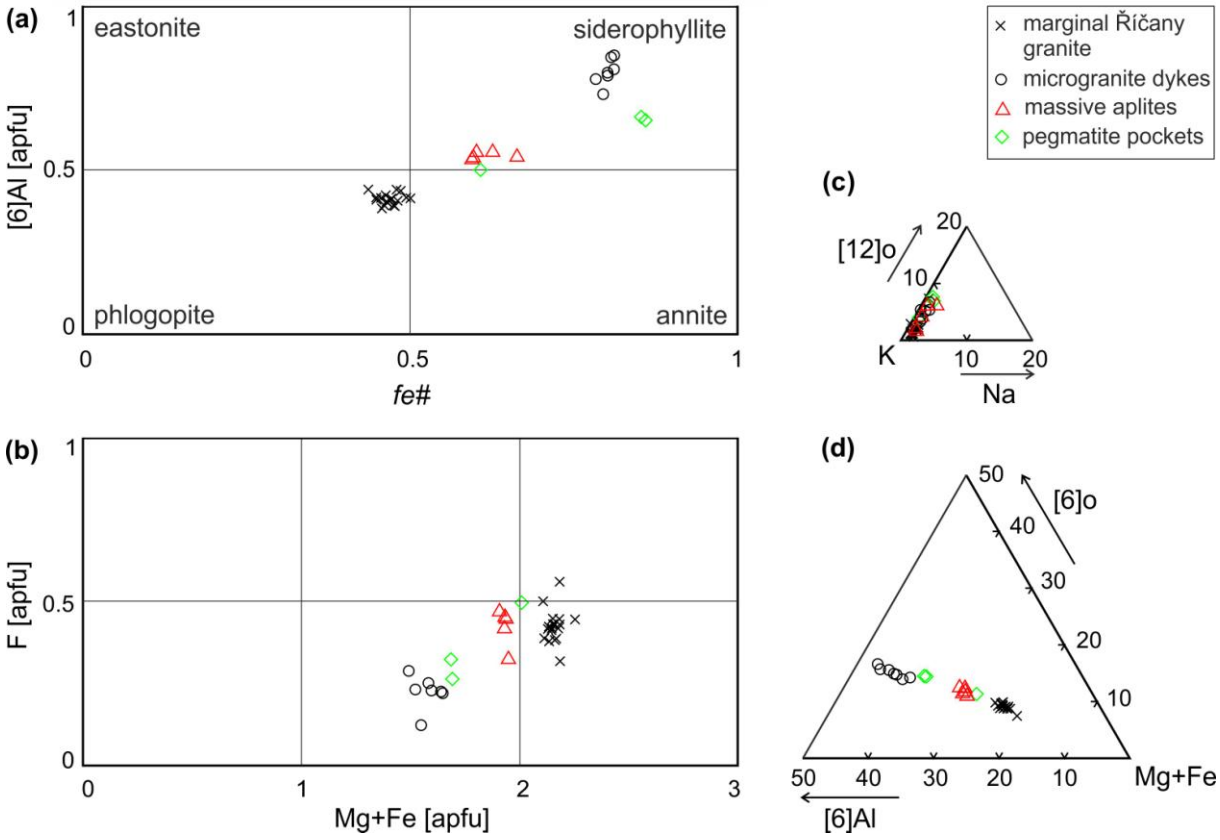

Fig. 4.4 Biotite molar compositions. (a) Octahedral Al *vs.* *fe#* (molar $Fe^{2+}/[Mg+Fe^{2+}]$). Phlogopite in marginal Říčany granite evolves to siderophyllite in aplite-pegmatite belt. (b) F pfu *vs.* (Mg+Fe) pfu. (c) Biotite from pegmatite pockets has slightly bigger vacancy in interlayer site. (d) Biotite from pegmatite pockets has more octahedral Al as well as bigger vacancy in octahedral site.

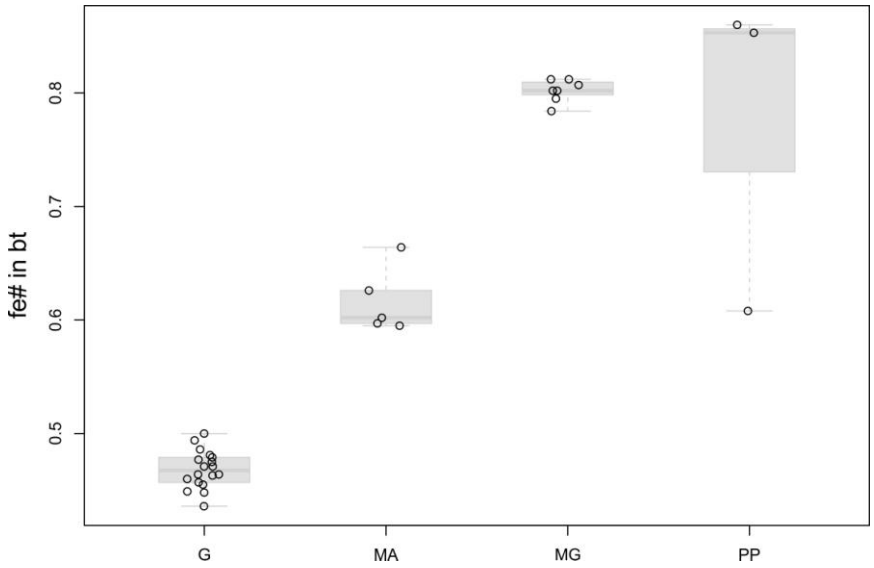

Fig. 4.5 Biotite molar compositions represented by the *fe#* value in the rock groups. The values are depicted for each rock group with a boxplot showing the median, two quartiles, and outlying values. Abbreviations: G – Říčany granite, MA – massive aplites, MG – microgranite dykes, PP – pegmatite pockets.

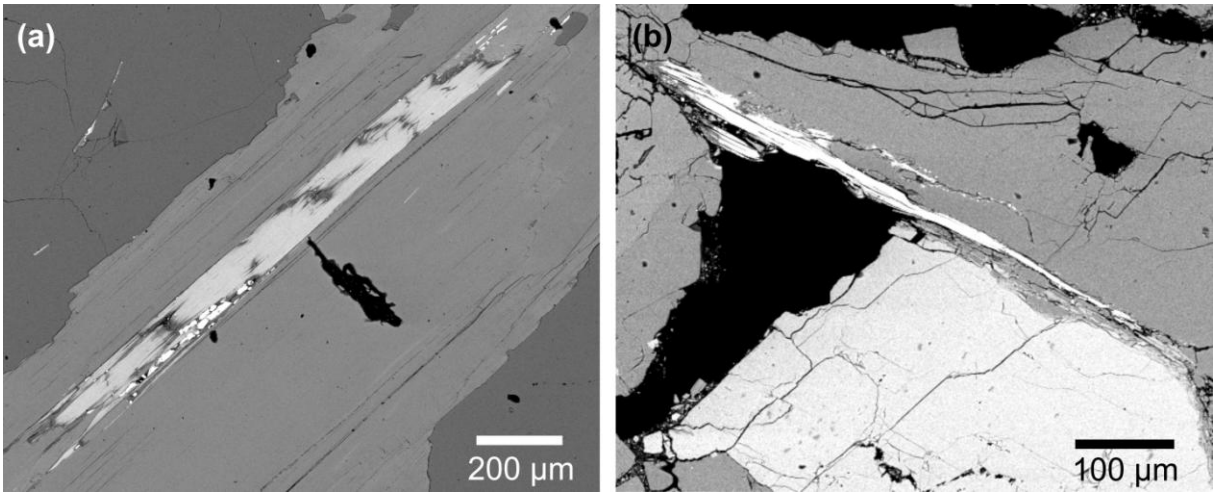

Fig. 4.6 Microphotographs of biotite in back-scattered electrons. (a) Biotite enclosed in muscovite from sample ZV3A (pegmatite pockets). (b) Biotite with unusual thin long habitus from sample DT10 (pegmatite pockets).

4.4 Muscovite

Muscovite is much more widespread than biotite, and it was analyzed in the marginal Říčany granite, microgranite dykes, massive aplites, layered aplites, pegmatite layers, megacryst zones (as alteration veins in feldspars grains), pegmatite pockets and pegmatite dykes. Crystallochemical formulas were calculated on the basis of 11 oxygens and by assuming all iron to be present in the ferrous form (Tab. 4.2). Lithium is assumed to be absent in micas, as confirmed by the whole-rock geochemical data.

Muscovite can be classified as muscovite *ss.* or aluminoceladonite, with the majority being ferroaluminoceladonite (Fig. 4.7). It has 27.3-38.4 wt. % of Al_2O_3 (2.3-3.0 Al pfu; Fig. 4.7) and 10.0-11.0 wt. % K_2O (0.9-1.0 K pfu). It has only 0.1-0.7 wt. % Na_2O (0.0-0.1 Na pfu), CaO concentrations are near the detection limit (2σ = 0.06 wt. % CaO, 0.0 Ca pfu) and Cs_2O concentrations remain below the detection limit (2σ = 0.15 wt. % Cs_2O), elevated concentrations are rare (0.16 wt. % Cs_2O). The octahedral site is occupied by 1.6-2.0 $^{[6]}$Al pfu, 0.0-0.3 but generally up to 0.24 Mg pfu (0.0-3.0 and 2.3 wt. % MgO), 0.0-0.3 but generally up to 0.2 Fe pfu (0.0-4.5 and 3.9 wt. % FeO), MnO concentrations are close to the detection limit (2σ = 0.08-0.13 wt. % MnO), slightly elevated concentrations are only in some samples (0.3-0.8 wt. % MnO, 0.01-0.04 Mn pfu), and up to 0.10 but generally less than 0.06 Ti pfu (2.1 and 1.1 wt. % TiO_2). Tetrahedral site is occupied by 3.0-3.3 Si pfu (44.3-48.2 wt. % SiO_2), 0.7-1.0 $^{[4]}$Al pfu. F concentrations are 0.1-1.8 wt. % F (0.0-0.4 F pfu; Fig. 4.7) and Cl remains below the detection limit (2σ = 0.04 wt. % Cl).

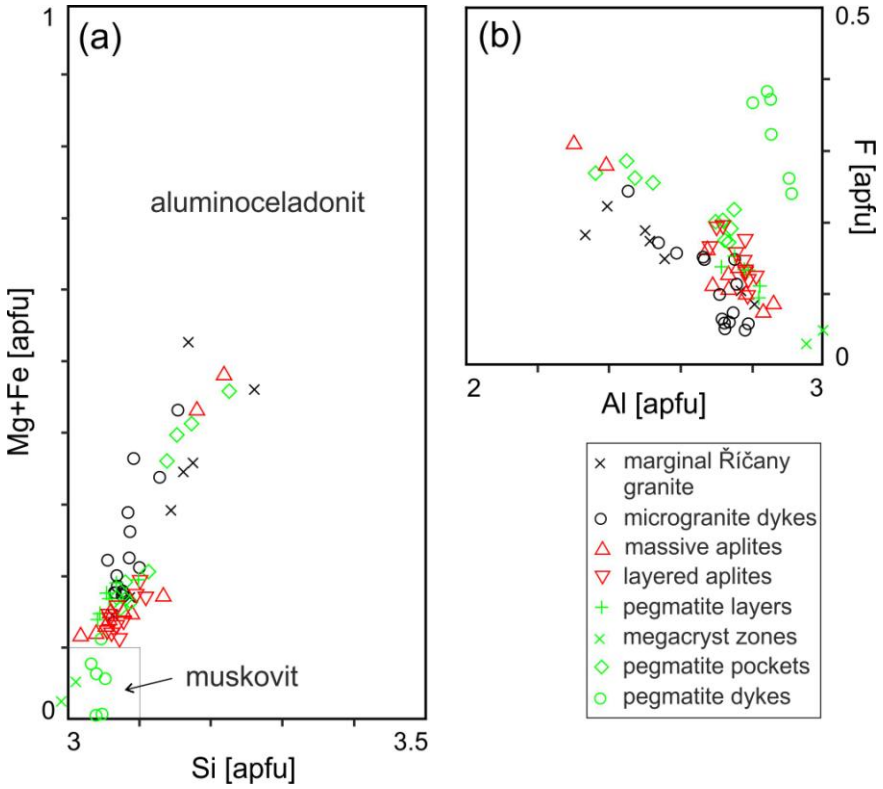

Fig. 4.7 Muscovite molar compositions. (a) Mg + Fe^{2+} *vs.* Si [apfu]. (b) F *vs.* Al [apfu]. Muscovites evolve toward compositions with lower ferromagnesian component, and bigger Al and lower F concentrations (only muscovites from pegmatite dykes are F-rich and Al-rich).

Muscovite from individual intrusive units differs mainly in element concentrations at octahedral site, that is Mg, Fe, Mn and $^{[6]}$Al, and in F and OH concentrations (Fig. 4.8). Muscovite from marginal Říčany granite has 0.19-0.22 Mg pfu, 0.11-0.14 Fe pfu, 1.68-1.70 $^{[6]}$Al pfu and 0.15-0.19 F pfu. Muscovite from the marginal Říčany granite next to the aplite dykes is enriched in Mg and Fe (0.28-0.30 Mg pfu and 0.16-0.25 Fe pfu) and depleted in $^{[6]}$Al

(1.57-1.60 [6]Al pfu). One probably secondary muscovite from the marginal Říčany granite with tiny anhedral habitus is depleted in Mg, Fe and F (0.08-0.11 Mg pfu, 0.06 Fe pfu and 0.08-0.10 F pfu) and enriched in [6]Al (1.86-1.88 [6]Al pfu). Muscovite from the microgranite dykes is depleted in Mg and F in comparison with the marginal Říčany granite and has similar concentration of Fe (0.06-0.17 but generally up to 0.10 Mg pfu, 0.11-0.26 but generally up to 0.20 Fe pfu and 0.05-0.24 but generally up to 0.17 F pfu) and is enriched in [6]Al (1.61-1.88 [6]Al pfu). That is similar to muscovite from the massive aplites, which has 0.02-0.28 Mg pfu, 0.09-0.20 Fe pfu, 0.07-0.31 F pfu and 1.53-1.91 [6]Al pfu. This muscovite has also relatively high concentrations of Mn (up to 0.03 Mn pfu). Muscovite from layered aplites is slightly depleted in Mg and Fe and slightly enriched in [6]Al in comparison with muscovite from the massive aplites (0.04-0.10 Mg pfu, 0.08-0.10 Fe pfu, 1.80-1.87 [6]Al pfu, and 0.10-0.20 F pfu). This is almost the same as the composition of muscovite from the pegmatite layers (0.04-0.08 Mg pfu, 0.10-0.12 Fe pfu, 1.82-1.87 [6]Al pfu, and 0.10-0.15 F pfu).

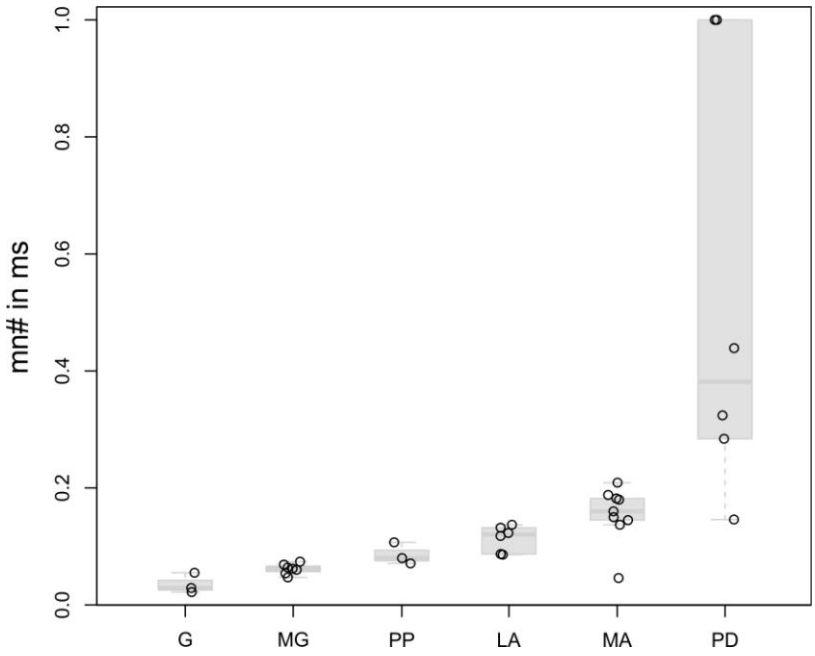

Fig. 4.8 Muscovite molar compositions represented by the *mn#* value in the rock groups. The values are depicted for each rock group with a boxplot showing the median, two quartiles, and outlying values. Abbreviations: G – Říčany granite, LA – layered aplites, MA – massive aplites, MG – microgranite dykes, PD – pegmatite dykes, PP – pegmatite pockets.

There are two types of muscovite in the pegmatite pockets. One type of muscovite is big, euhedral and slightly fan-like and has similar composition to the previous two groups except that it is enriched in F (0.05-0.07 Mg pfu, 0.10-0.14 Fe pfu, 0.17-0.22 F pfu and 1.80-1.83 [6]Al pfu). The second type is much smaller and subhedral and is enriched in Mg, Fe and F and depleted in [6]Al in comparison with the first type of muscovite (0.20-0.23 Mg pfu, 0.16-0.23 Fe pfu, 0.26-0.29 F pfu, and 1.60-1.67 [6]Al pfu). Muscovite from pegmatite dykes is extremely depleted in Mg and Fe and enriched in [6]Al and F (0.00-0.01 Mg pfu, 0.00-0.10 Fe pfu, 0.24-0.38 F pfu and 1.85-1.97 [6]Al pfu). This muscovite has also relatively high

concentrations of Na and Mn (0.05-0.10 Na pfu and 0.02-0.05 Mn pfu). In the coarser varieties of the aplite-pegmatite unit (e.g. megacryst zones) are veins in bigger feldspars composed of small thin grains of muscovite with radial arrangement. These muscovites do not contain any Mg, contain 0.02-0.05 Fe pfu, 0.03-0.05 F pfu and very much Al (2.0 $^{[6]}$Al pfu and 1.0 $^{[4]}$Al pfu). There is no compositional zonation in muscovites.

Tab. 4.2 Representative chemical composition of micas.

Sample	DT5/2	DTX3	DT10	ZV3A	DT5/2	ZV2A	ZV3A	TJ22A
Analysis	14	49	18	13	20	2	5	14
Group	G	G	PP	PP	G	MA	PP	PD
mineral	bt	bt	bt	bt	ms	ms	ms	ms
SiO_2 (*wt. %*)	37.177	36.810	36.478	36.386	46.775	44.887	45.376	44.848
TiO_2	2.620	1.918	2.283	2.966	0.404	0.364	0.766	0.470
Al_2O_3	17.131	16.418	17.084	19.523	31.272	35.508	34.533	35.468
FeO	15.425	14.913	18.366	22.207	2.484	1.715	1.832	0.901
MnO	0.450	0.481	0.447	1.270	*n.d.*	0.391	*n.d.*	0.695
MgO	9.995	10.288	6.656	2.035	2.151	0.215	0.657	*n.d.*
CaO	0.084	*n.d.*	0.067	0.142	*n.d.*	*n.d.*	*n.d.*	*n.d.*
Na_2O	0.056	*n.d.*	*n.d.*	*n.d.*	0.277	0.496	0.620	0.613
K_2O	9.933	9.779	9.333	9.027	10.820	10.574	10.183	10.101
Cs_2O	*n.d.*	*n.d.*	0.600	*n.d.*	*n.d.*	*n.d.*	*n.d.*	*n.d.*
F	1.747	2.260	1.978	1.068	0.876	0.340	1.017	1.780
Total	93.881	91.984	92.507	94.394	94.815	94.403	94.755	94.222
OH (calc.)	5.806	5.183	5.353	6.268	7.545	8.052	7.454	6.716
Total +OH	99.687	97.167	97.861	100.662	102.360	102.455	102.209	100.938
Si (*per 11 O*)	2.855	2.891	2.898	2.851	3.178	3.040	3.070	3.055
$^{[4]}$Al	1.145	1.109	1.102	1.149	0.822	0.960	0.930	0.945
$^{[6]}$Al	0.406	0.411	0.498	0.654	1.682	1.875	1.825	1.903
Fe	0.991	0.979	1.220	1.455	0.141	0.097	0.104	0.051
Mn	0.029	0.032	0.030	0.084	-	0.022	-	0.040
Ti	0.151	0.113	0.136	0.175	0.021	0.019	0.039	0.024
Mg	1.144	1.204	0.788	0.238	0.218	0.022	0.066	0.000
Ca	0.007	-	0.006	0.012	-	-	-	-
Na	0.008	0.010	0.008	0.010	0.037	0.065	0.081	0.081
K	0.973	0.980	0.946	0.902	0.938	0.914	0.879	0.878
Cs	-	-	0.020	-	-	-	-	-
Total cat.	7.709	7.731	7.652	7.529	7.036	7.013	6.994	6.977
F^-	0.424	0.561	0.497	0.265	0.188	0.073	0.218	0.383
OH^-	1.576	1.439	1.503	1.735	1.812	1.927	1.782	1.617
fe#	0.464	0.449	0.608	0.860	0.393	0.817	0.610	1.000
mn#	0.029	0.032	0.024	0.055	0.000	0.188	0.000	0.439

n.d. – below detection limit, bt – biotite, ms – muscovite, G – Říčany granite, MA – massive aplites, PP – pegmatite pockets, PD – pegmatite dykes

4.5 Garnet

Garnet was observed and analyzed in the aplite-pegmatite unit in layered aplites, pegmatite layers and pegmatite dykes. Exploratory recalculations of crystallochemical formulas based on 12 oxygen atoms lead to violation of individual site occupancies and unrealistically high concentrations of ferric iron, and these indicate partial vacancy in the tetrahedral site. The crystallochemical formulas were calculated on the basis of 5 cations in octahedral and cubic site (Tab. 4.3).

Garnet is extremely Mn-rich with 17.8-38.7 wt. % MnO (1.2-2.7 Mn pfu), 4.7-25.3 wt. % FeO (0.3-1.7 Fe^{2+} pfu), 0.1-0.9 but generally less than 0.5 wt. % CaO (0.01-0.08 and 0.05 Ca pfu) and MgO close to the detection limit (2σ = 0.04-0.07 wt. % MgO) except one sample from layered aplites (0.05-0.27 wt. % MgO, 0.01-0.03 Mg pfu) (Tab. 4.3). Our garnet is therefore mainly spessartine-almandine solid solution. Octahedral site is occupied by 1.91-1.97 Al pfu (19.56-20.50 wt. % Al_2O_3), 0.03-0.08 Fe^{3+} pfu (calculated) and up to 0.02 Ti pfu (up to 0.36 wt. % TiO_2). Tetrahedral site is occupied by 2.77-2.92 Si pfu (33.45-35.77 wt. % SiO_2) and by 0.00-0.01 P pfu (up to 0.19 wt. % P_2O_5, 2σ = 0.04-0.09 wt. % P_2O_5), which is compensated by up to 0.01 vacancy pfu in cubic site. Calculated 0.33-0.86 OH^- pfu substitutes for SiO_4 group. This leads us to a conclusion, that our garnet is mainly a hydrous spessartine.

The *mn#* value (molar Mn/[Fe^{2+}+Mn]) in garnet has trimodal distribution and it provides a useful indicator for the degree of magma differentiation (Fig. 4.9). Disseminated grains or bands of garnet in layered aplites (including aplites near pegmatite layers) have *mn#* = 0.43-0.64 with the bands of garnet having *mn#* = 0.56-0.63. Garnet from pegmatite layers can have similar values of *mn#* like that from the fine-grained parts (in sample TJ6A), or it has *mn#* = 0.68-0.82 (in sample TD2). The most evolved garnet is represented by sample TJ22A from pegmatite dykes, with *mn#* = 0.85-0.90. There are basically only Fe^{2+} and Mn in cubic site, so they vary proportionally. No other elements in garnets vary systematically. The rims of grains tend to be depleted in Ti in comparison with the central parts of the same grains.

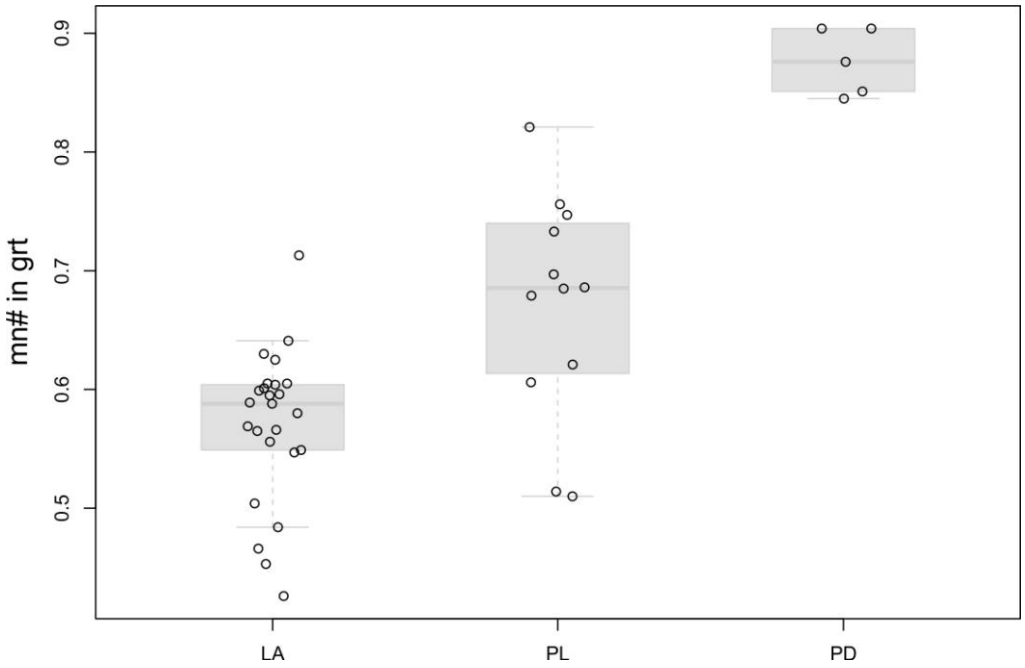

Fig. 4.9 Garnet molar compositions represented by the *mn#* value in the rock groups. The values are depicted for each rock group with a boxplot showing the median, two quartiles, and outlying values. Abbreviations: LA – layered aplites, PD – pegmatite dykes, PL – pegmatite layers.

Tab. 4.3 Representative chemical composition of garnets.

Sample	TJ10A	TJ16	TJ16	TJ6A	TD2	TD2	TJ22A	TJ22A
Analysis	39	26	27	33	1	2	1	3
Group	LA	LA	LA	PL-band	PL	PL	PD	PD
position	rim	center	rim	center	center	rim	center	rim
SiO_2 (*wt. %*)	34.838	34.826	35.343	33.896	33.449	35.000	34.709	35.012
TiO_2	0.095	0.241	*n.d.*	0.363	0.326	0.150	0.277	0.131
Al_2O_3	19.996	19.965	20.151	19.806	19.597	19.563	19.999	20.186
FeO	23.133	17.924	20.151	16.672	11.366	14.499	7.519	4.651
MnO	19.507	25.490	23.343	26.426	31.891	28.898	36.101	38.518
MgO	0.134	*n.d.*	0.118	0.084	*n.d.*	*n.d.*	*n.d.*	*n.d.*
CaO	0.376	0.254	0.351	0.213	0.370	0.393	0.386	0.351
P_2O_5	*n.d.*	*n.d.*	*n.d.*	*n.d.*	0.192	0.087	0.130	*n.d.*
Total	98.127	98.767	99.554	97.641	97.190	98.590	99.121	98.939
OH (*calc.*)	1.389	1.711	1.371	2.520	2.932	1.204	2.093	1.649
Total + OH	99.517	100.478	100.925	100.161	100.167	99.800	101.214	100.588
P (*per 5 cat.*)	-	-	-	-	0.013	0.006	0.009	-
Si	2.898	2.875	2.901	2.809	2.772	2.906	2.840	2.880
Al	1.961	1.943	1.949	1.935	1.914	1.914	1.929	1.957
Fe^{3+}	0.033	0.042	0.051	0.043	0.065	0.076	0.054	0.035
Ti	0.006	0.015	-	0.023	0.020	0.009	0.017	0.008
Mg	0.017	-	0.014	0.010	-	-	-	-
Fe^{2+}	1.576	1.195	1.332	1.113	0.722	0.930	0.460	0.285
Mn	1.374	1.782	1.623	1.855	2.238	2.032	2.502	2.684
Ca	0.034	0.022	0.031	0.019	0.033	0.035	0.034	0.031
Total cat.	7.898	7.875	7.901	7.812	7.779	7.909	7.844	7.880
Total O	11.782	11.737	11.776	11.621	11.548	11.790	11.679	11.747
OH^-	0.408	0.499	0.398	0.738	0.859	0.353	0.605	0.479
mn#	0.466	0.599	0.549	0.625	0.756	0.686	0.845	0.904

n.d. – below detection limit, LA – layered aplites, PL – pegmatite layers, PD – pegmatite dykes

4.6 Tourmaline

Tourmaline was observed and analyzed in all rock types in the aplite-pegmatite unit and in the marginal Říčany granite near aplite dykes where tourmalinization occurred. It forms variously sized grains which can be zonal with alternating darker brownish zones and lighter greyish zones, or tiny greenish grains in the interstitial space of other mineral grains. The zonation of some tourmaline grains is visible in the back-scattered electron mode on the electron microscope (Fig. 4.12). Most of crystallochemical formulas were calculated on the basis of 15 cations in T, Z and Y sites using the general crystallochemical formula of Henry et al., 2011: $XY_3Z_6(T_6O_{18})(BO_3)_3V_3W$ and by assuming all iron to be present in the ferrous form and no lithium to be present (Tab. 4.4). Part of the crystallochemical formulas in the samples TJ22A and TJ19B were calculated on the basis of 24.5 oxygens by assuming lithium to be equal the vacancy in Y site (it was too large in previous recalculations) and all iron to be present in the ferrous form.

Tourmalines can be classified as dravites, schorls or elbaites (Fig. 4.11). They have 0.07-1.76 Mg pfu (0.26-6.85 wt. % MgO), 0.51-2.34 Fe pfu (3.46-16.38 wt. % FeO), up to 0.60 but generally less than 0.22 Mn pfu (up to 4.10 and 1.30 wt. % MnO), and up to 0.86 but in Li-bearing tourmalines up to 1.55 Al in Y site (total 5.76-7.55 Al pfu, 28.06-36.75 wt. %

Al_2O_3). X site is occupied by 0.48-0.87 Na pfu (1.50-2.55 wt. % Na_2O), up to 0.31 but generally less than 0.09 Ca pfu (up to 1.71 and 0.50 wt. % CaO), and up to 0.05 K pfu (K_2O concentrations are near the detection limit, 2σ = 0.04-0.05 wt. % K_2O). Vacancy in X site reaches 0.06-0.51 apfu. Z site is in most cases fully occupied by Al, in rare cases is there up to 0.29 Mg pfu. T site is occupied by Si (5.74-6.00 Si pfu, 31.79-35.90 wt. % SiO_2) and up to 0.26 Al pfu. W site is occupied by up to 0.28 but in Li-bearing tourmalines up to 0.94 F pfu (up to 0.53 and 1.71 wt. % F), up to 0.26 O pfu, and OH^- group.

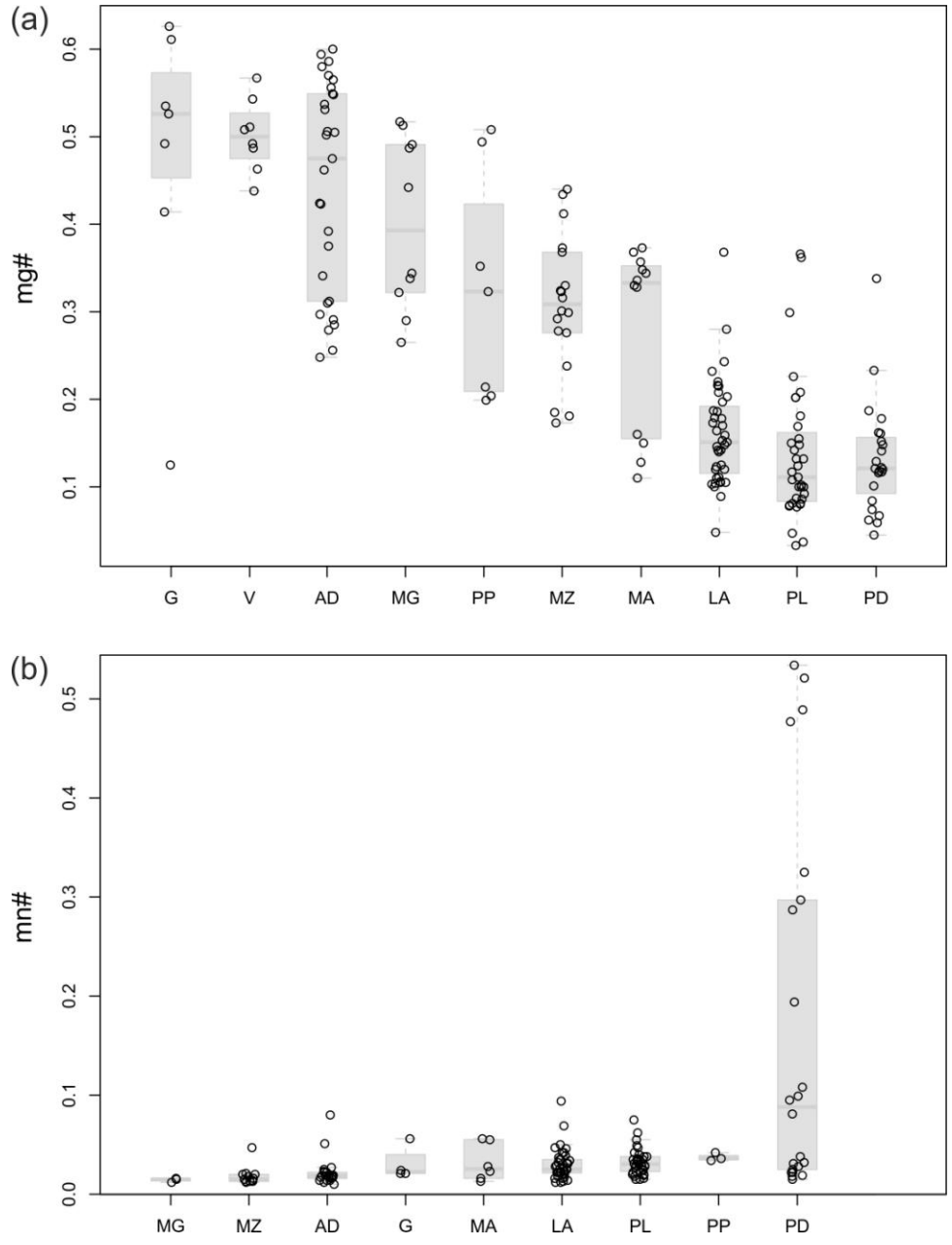

Fig. 4.10 Tourmaline molar compositions in the rock groups. (a) The *mg#* value of tourmaline. (b) The *mn#* value of tourmaline. The values are depicted for each rock group with a boxplot showing the median, two quartiles, and outlying values. Abbreviations: AD – aplite dykes, G – Říčany granite, LA – layered aplites, MA – massive aplites, MG – microgranite dykes, MZ – megacryst zones, PD – pegmatite dykes, PL – pegmatite layers, PP – pegmatite pockets, V – veins.

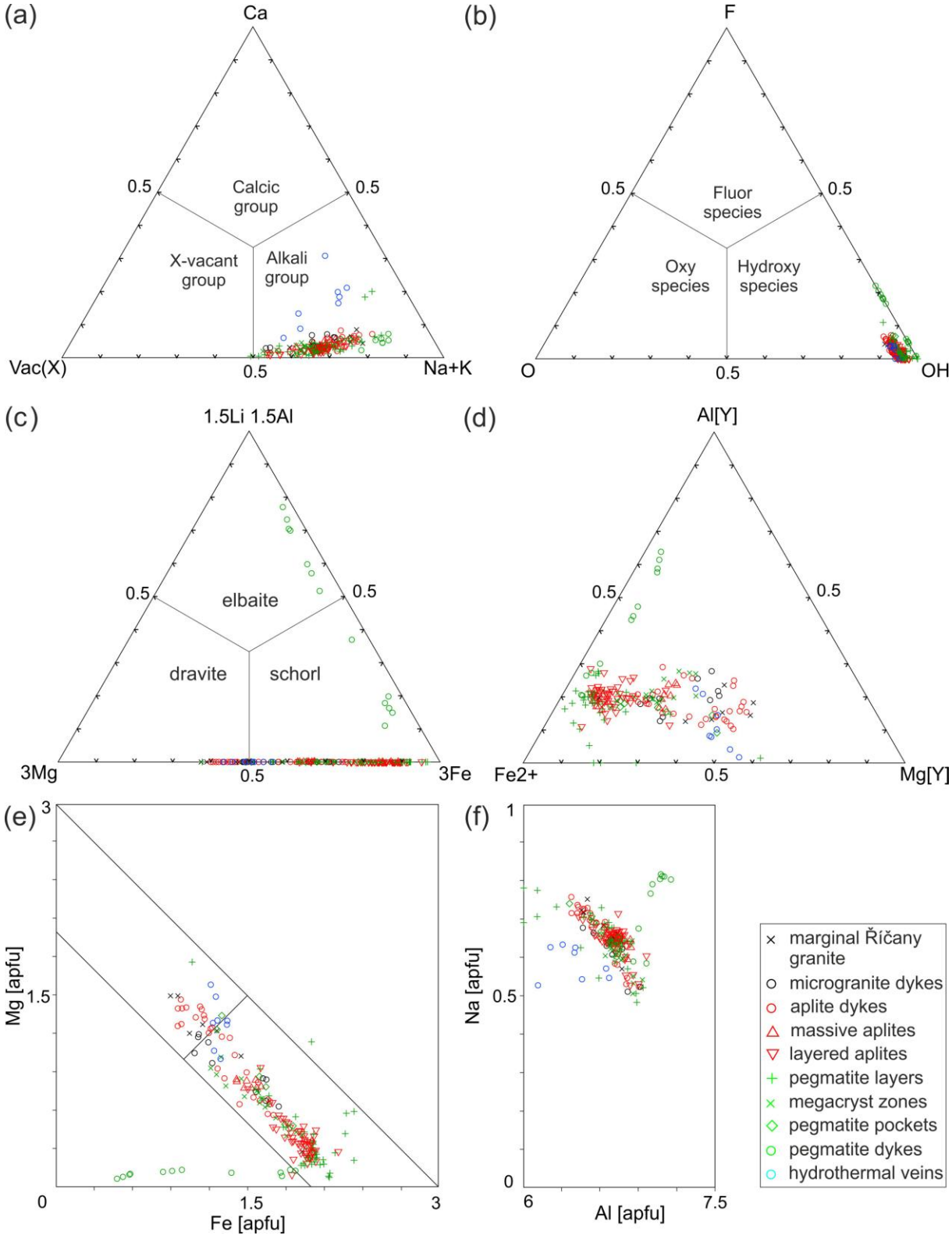

Fig. 4.11 Tourmaline molar compositions. (a) Ternary system for the primary tourmaline groups based on the dominant occupancy of the X site; Vac(X) = vacancy in the X site; Henry at al., 2011. (b) Ternary system for a general series of tourmaline species based on the anion occupancy of the W site; Henry et al., 2011. (c) Ternary diagram used for classifying alkali-group tourmaline with OH^- dominance at the W site based on the Y site occupancy; Henry at al., 2011. (d) Ternary diagram showing proportion of the main elements at the Y site. (e) Mg [apfu] *vs.* Fe [apfu] diagram. (f) Na

[apfu] *vs.* Al [apfu] diagram showing the different nature of the hydrothermal veins and pegmatite dykes tourmalines. ´

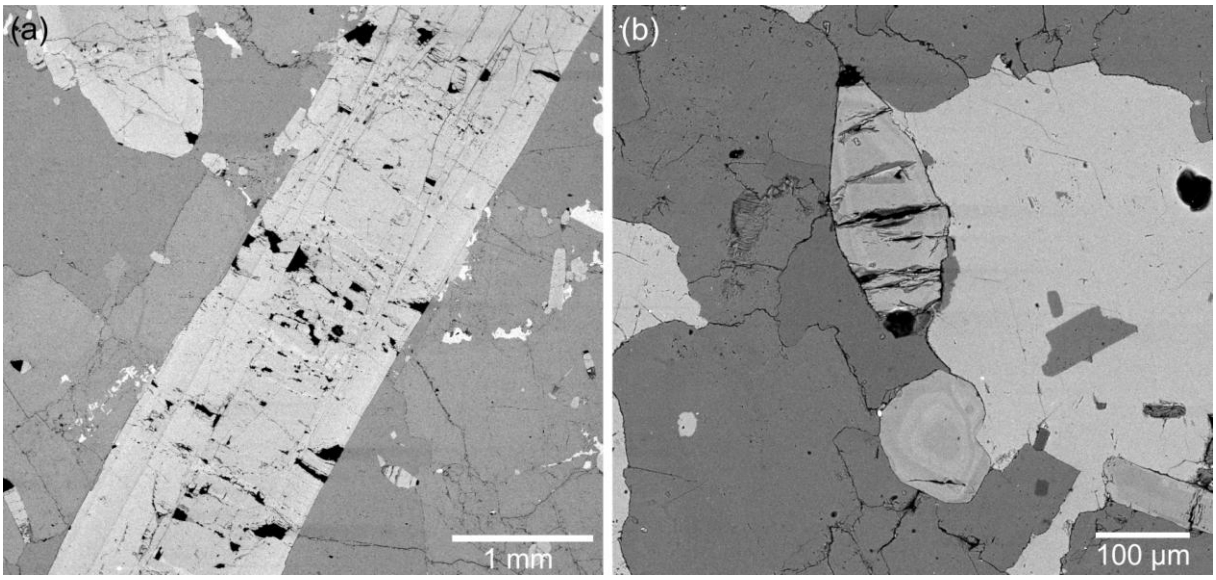

Fig. 4.12 Microphotographs of tourmaline in back-scattered electrons. (a) Zonal tourmaline from the sample DT 20/1 (megacryst zones). (b) Zonal tourmaline from the sample TJ10A (layered aplites).

Tourmalines from individual units and the zones in tourmaline grains vary systematically in concentrations of elements in Y site mainly. The *mg#* value (molar Mg/[Fe+Mg]) and *mn#* value (molar Mn/[Fe+Mn]) in tourmaline provides a useful indicator for the degree of magma differentiation (Fig. 4.10). The lighter zones in back-scattered electron images of tourmalines (Fig. 4.12) have always smaller *mg#* and bigger *mn#* values than the darker zones in the same grains (they are always relatively depleted in Mg and enriched in Fe and Mn) (Fig. 4.13). The *mn#* value is rarely bigger than 0.10, therefore we will focus on the *mg#* value. Tourmaline from microgranite dykes has darker cores and lighter thin rims in back-scattered electron images and total *mg#* = 0.27-0.52 (measured from cores as well as rims). Tourmaline from aplite dykes has similar or slightly bigger *mg#* values (*mg#* = 0.26-0.60) and can have similar zoning style too, or the darker and lighter zones can alternate several times and then end with a darker rim. Two types of tourmalines were analyzed from the tourmalinized marginal Říčany granite near the aplite dykes. One is dark and unzonal tourmaline replacing biotite with *mg#* = 0.53-0.63, and the other is big euhedral gradually zonal tourmaline with lighter rim than core and *mg#* = 0.13-0.54. Tourmaline from massive aplites has also big dark cores and thin lighter rims, but although it is still true, that the lighter color in back-scattered electron image the smaller *mg#* and bigger *mn#*, the total *mg#* values are smaller: *mg#* = 0.11-0.37. The *mg#* values of tourmalines from the layered aplites are similar to massive aplites tourmalines (*mg#* = 0.09-0.37), but if the tourmalines are in the form of tiny greenish grains in the interstitial space of other mineral grains, they have only *mg#* = 0.05-0.21. The zoning style in layered aplites can be various, but the cores are always dark.

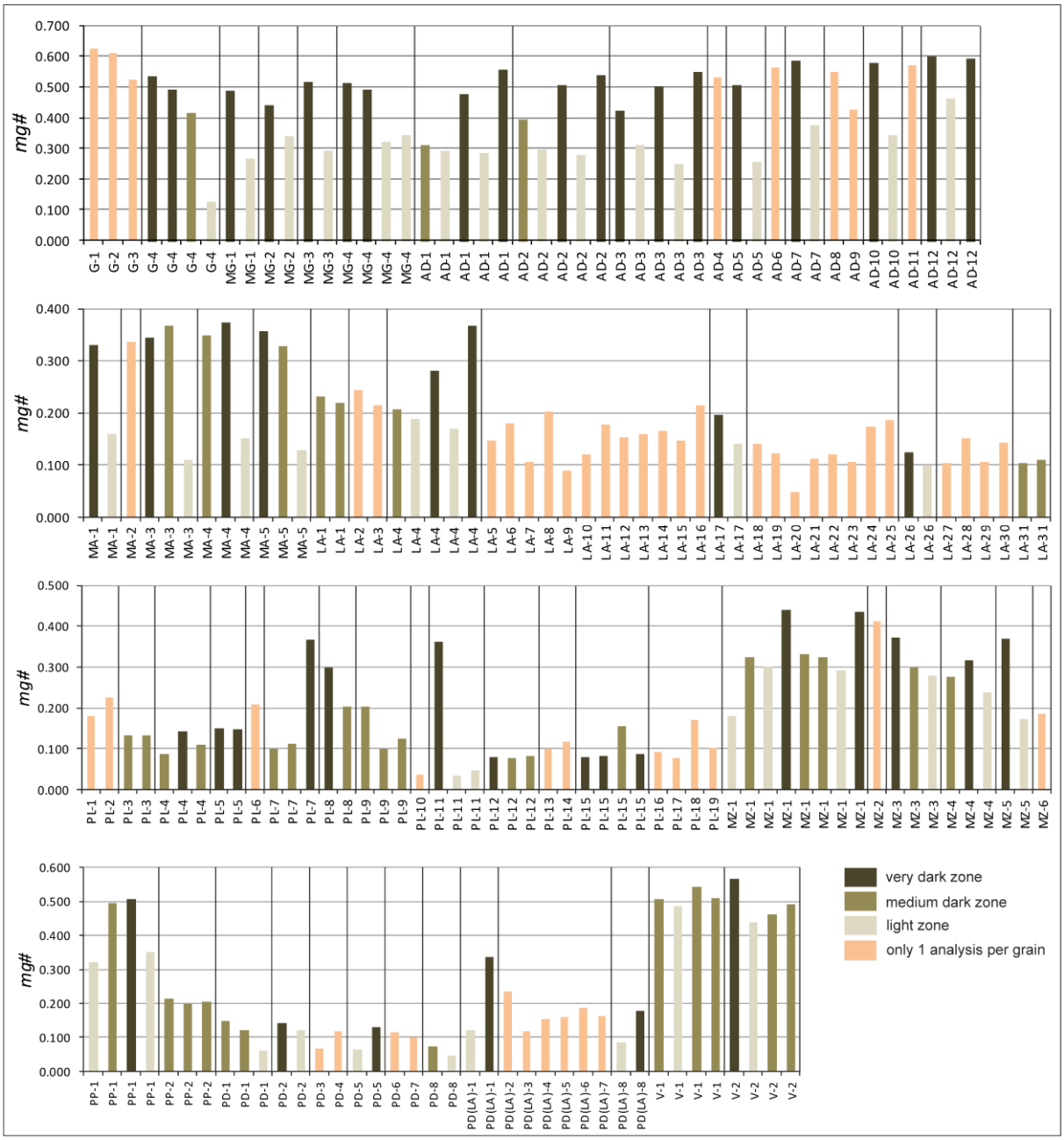

Fig. 4.13 Difference in mg# value in different zones in tourmaline grains. Individual columns represent individual analysis marked by the abbreviation of the rock group and number of the grain analysed (for example PP-1 is analysis in pegmatite pockets in grain number 1). Grains with more analysis than 1 are separated by black vertical lines. Dark brown color represents a relatively very dark zone, light brown color represents a relatively medium dark zone, and light grey color represents a relatively light zone in back-scattered electrons. Pink color is used for the analyses which were sole in the grain and can not be compared to other zones in the grain, because the color differences depicted here are only relative within the grain. The darker is the zone in the grain in back-scattered electrons, the higher is the mg# value in the zone.

Tourmalines from pegmatite layers and aplites around them have similar total *mg#* values (*mg#* = 0.03-0.37) to layered aplites, but the dark cores of the tourmaline grains are smaller and the majority of analysed compositions has *mg#* below 0.23 (Fig. 4.10). Big

tourmalines from megacryst zones have *mg#* = 0.18-0.44 with usually dark cores and light rims, but the colors can alternate in between several times, and the tourmalines from the aplites around them have *mg#* = 0.17-0.37 also with darker cores. Tourmalines from the pegmatite pockets can have relatively primitive *mg#* values (*mg#* = 0.32-0.51 in one pocket, interstitial tourmaline) as well as relatively evolved *mg#* values (*mg#* = 0.20-0.21 in another pocket, euhedral unzonal tourmaline). They have relatively high F concentrations (0.13-0.28 F pfu). Tourmaline from the pegmatite dykes has *mg#* = 0.05-0.15, *mn#* =0.03-0.53 (the higher *mn#*, the higher Al in Y – up to 1.55 Al in Y pfu), up to 0.94 F pfu, and it is the Li-bearing one. This tourmalines have lighter cores and darker rims. The tourmalines from the aplites around them correspond to massive or layered aplites (*mg#* = 0.12-0.34). Tourmalines from hydrothermal veins have *mg#* = 0.44-0.57, *mn#* value always 0.00, and anomalously high Ca concentrations (0.06-0.31 Ca pfu). They are in bands usually at the margins of hydrothermal veins and are zonal.

Tab. 4.4 Representative chemical composition of tourmaline.

Sample	TDX2	TDX2	TJ10A	TJ10A	TJ10A	TJ6A	DT20/1	DT10	TJ22A	TJ22A
Analysis	26	25	16	15	24	5	14	12	23	21
Group	AD	AD	LA	LA	LA	PL	MZ	PP	PD	PD
zone in grain	dark	light	dark	light	unzonal	dark	dark	light	light	dark
SiO_2 (*wt. %*)	35.022	34.367	34.324	33.745	33.646	35.243	35.113	34.137	33.577	35.072
TiO_2	1.191	0.786	0.859	0.891	0.383	0.350	0.400	0.486	0.881	0.429
Al_2O_3	32.007	33.053	32.105	32.857	33.022	35.074	35.195	32.550	33.393	36.747
FeO	7.993	11.760	11.231	13.507	13.879	14.001	9.002	11.425	12.807	4.155
MnO	0.098	0.268	0.151	0.364	0.552	0.541	*n.d.*	*n.d.*	1.388	3.922
MgO	5.614	2.627	3.673	1.555	1.057	0.672	3.533	3.053	0.518	0.384
CaO	0.397	0.129	0.290	0.153	0.147	*n.d.*	0.130	0.210	0.145	0.332
Na_2O	2.319	1.999	2.115	2.006	1.990	1.498	1.676	1.977	1.968	2.514
K_2O	0.078	0.040	0.049	0.063	0.071	*n.d.*	*n.d.*	*n.d.*	0.087	*n.d.*
F	0.445	*n.d.*	0.281	*n.d.*	*n.d.*	*n.d.*	*n.d.*	0.513	0.449	1.383
Total	84.976	85.110	84.965	85.193	84.746	87.444	85.169	84.302	85.024	84.360
B_2O_3 (*calc.*)	10.288	10.185	10.175	10.089	10.024	10.431	10.394	10.079	10.096	10.353
Total + B_2O_3	95.264	95.295	95.141	95.282	94.771	97.875	95.563	94.381	95.120	94.713
(per T+Z+Y=15)									*(per 24.5 O)*	
Si	5.917	5.865	5.864	5.814	5.834	5.873	5.872	5.888	5.781	5.888
^{T}Al	0.083	0.135	0.136	0.186	0.166	0.127	0.128	0.112	0.219	0.112
^{Z}Al	6.000	6.000	6.000	6.000	6.000	6.000	6.000	6.000	6.000	6.000
^{Y}Al	0.292	0.514	0.328	0.486	0.584	0.762	0.810	0.505	0.558	1.161
Ti	0.151	0.101	0.110	0.115	0.050	0.044	0.050	0.063	0.114	0.054
Fe	1.129	1.678	1.604	1.946	2.012	1.951	1.259	1.648	1.844	0.583
Mn	0.014	0.039	0.022	0.053	0.081	0.076	-	-	0.202	0.558
Mg	1.414	0.668	0.935	0.399	0.273	0.167	0.881	0.785	0.133	0.096
Li	-	-	-	-	-	-	-	-	0.044	0.491
Ca	0.072	0.024	0.053	0.028	0.027	-	0.023	0.039	0.027	0.060
Na	0.759	0.661	0.700	0.670	0.669	0.484	0.543	0.661	0.657	0.818
K	0.017	0.009	0.011	0.014	0.016	-	-	-	0.019	-
Total cat.	15.848	15.694	15.764	15.712	15.712	15.484	15.566	15.700	15.554	15.331
Total O	24.716	24.649	24.615	24.636	24.628	24.603	24.686	24.628	24.500	24.500
F^-	0.238	-	0.152	-	-	-	-	0.280	0.244	0.734
mg#	0.556	0.285	0.368	0.170	0.120	0.079	0.412	0.323	0.067	0.141
mn#	0.012	0.023	0.013	0.027	0.039	0.038	0.000	0.000	0.099	0.489

n.d. – below detection limit, AD – aplite dykes, LA – layered aplites, PL – pegmatite layers, MZ – megacryst zones, PP – pegmatite pockets, PD – pegmatite dykes

4.7 Beryl

Beryl was observed and analyzed in layered aplites, pegmatite layers in aplites, megacryst zones and pegmatite dykes. Crystallochemical formulas were calculated on the basis of 15 oxygen atoms (without 3 BeO which can not be measured on electron microscope) and by assuming the all iron is present in the ferrous form.

Beryl contains mainly aluminium apart from silicon and beryllium (1.91-2.00 Al pfu, 17.84-18.82 wt % Al_2O_3), its main admixtures are iron (0.01-0.07 Fe pfu, 0.16-0.90 wt. % FeO) and sodium (0.03-0.09 Na pfu, 0.18-0.50 wt. % Na_2O). MgO, MnO, CaO, K_2O and TiO_2 concentrations are below their detection limits, with rare exceptions of MgO (up to 0.13 wt. % MgO, 0.02 Mg pfu) and TiO_2 (0.12 wt. % TiO_2, 0.01 Ti pfu). BeO concentrations were calculated assuming 3 Be pfu (13.66-13.86 wt. % BeO) and added to the sum of other measured oxides (total of 98.43-99.50 wt. % oxides). Beryls from different units do not vary significantly in their composition.

4.8 Topaz

Topaz was found and analyzed only in pegmatite dykes. Crystallochemical formulas were calculated on the basis of 5 oxygen atoms.

Topaz in pegmatite dykes is very pure and fluor-rich, with 0.99 Si pfu (31.2-31.6 wt. % SiO_2), 2.0 Al pfu (54.2-54.6 wt. % Al_2O_3) and 1.83-1.86 F pfu (18.4-18.6 wt. % F), calculated 0.14-0.17 OH pfu).

4.9 Accessory phosphates

4.9.1 Apatite

Apatite was analyzed in every unit except pegmatite pockets and hydrothermal veins, that are marginal Říčany granite, microgranite and aplite dykes, massive aplites, layered aplites, pegmatite layers, megacryst zones and pegmatite dykes. Crystallochemical formulas were calculated on the basis of 12.5 oxygen atoms. However, concentrations of fluorine or chlorine in apatite can not be measured accurately with EDS with unknown crystallochemical orientations of the apatite grains (Henderson, 2011). Therefore the measured concentrations of components in the hydroxyl site in our apatites must be taken only as approximate.

All analyzed apatites can be classified as fluorapatites with a high probability, because nearly all of them have their apparent fluorine concentrations bigger than 1 F pfu, and even when considering the mistake in measuring we can say that all the apatites are very fluorine-rich (3.7-6.2 wt. % F measured). Chlorine concentrations are below the detection limit (2σ = 0.04 wt. % Cl). The tetrahedral site of the apatites is occupied by 2.97-3.00 P pfu (41.72-42.68 wt. % P_2O_5) with a little admixture of up to 0.05 Si pfu (up to 0.56 wt. % SiO_2). The apatites further contain 4.5-4.9 or rarely up to 5.0 Ca pfu (49.6-54.4 and 57.3 wt. % CaO), up

to 0.34 or rarely up to 0.46 Mn pfu (up to 4.83 and 6.41 wt. % MnO), up to 0.05 Sr pfu (up to 1.08 wt. % SrO) and rarely elevated concentrations of iron (up to 0.02 pfu, up to 0.34 wt. % FeO), potassium (up to 0.03 K pfu, up to 0.27 wt. % K_2O), and cerium (up to 0.01 Ce pfu, up to 0.21 wt. % Ce_2O_3).

Apatites from individual intrusive units differ systematically mainly in manganese, iron or calcium content. Apatites from marginal Říčany granite, which are mainly associated with biotite, have 0.02-0.03 Mn pfu and about 0.02 Fe pfu. Apatites from microgranite dykes have 0.04-0.06 Mn pfu and up to 0.02 Fe pfu. Apatites from aplite dykes, massive aplites, layered aplites and megacryst zones have 0.09-0.11 Mn pfu and usually 0.00 or rarely up to 0.01 Fe pfu. Apatites from all the previous units have 4.8-4.9 Ca pfu. A calcium-rich apatite was analyzed in pegmatite layer (5.0 Ca pfu, 0.00 Mn and Fe pfu). Apatites from pegmatite dykes are extremely manganese-rich (0.28-0.46 Mn pfu, 0.00 Fe pfu) and calcium-poor (4.5-4.7 Ca pfu).

4.9.2 Xenotime-(Y)

Few xenotime-(Y) grains were analyzed in marginal Říčany granite, aplite dykes, massive aplites and pegmatite dykes. Crystallochemical formulas were calculated on the basis of 4 oxygen atoms. The sums of analyzed oxides are too low (71.5-90.8 wt. %), therefore the measured concentrations must be taken only as approximate and emphasis should be put on the relative differences.

Xenotime-(Y) contains 0.97-1.03 P pfu (27.3-33.1 wt. % P_2O_5) and other components vary in different xenotime-(Y) grains. Yttrium concentrations are relatively bigger in xenotime-(Y) from marginal Říčany granite (0.75 Y pfu), medium in the xenotime-(Y) from aplite dykes and pegmatite dykes (0.67 Y pfu) and low in xenotime-(Y) from massive aplites (0.43 Y pfu). Inverse distribution of concentrations in xenotime-(Y) have calcium and silicon (G: 0.00 Si pfu, up to 0.01 Ca pfu; AD and PD: 0.10-0.11 Si pfu, 0.01-0.02 Ca pfu; MA: 0.27 Si pfu, 0.07 Ca pfu). Thorium concentrations are biggest in xenotime-(Y) from massive aplites (MA: 0.05 Th pfu, other: 0.01-0.02 Th pfu), uranium concentrations do not vary systematically (0.01-0.02 rarely up to 0.04 U pfu). Gadolinium and erbium concentrations are biggest in xenotime-(Y) from marginal Říčany granite (0.03 Gd pfu, 0.04-0.05 Er pfu), medium in aplite dykes and massive aplites (0.02 Gd pfu, 0.04 Er pfu) and there are none in pegmatite dykes. Dysprosium and ytterbium concentrations in xenotime-(Y) vary as follows: G: 0.06 Dy pfu, 0.04 Yb pfu; AD: 0.05 Dy pfu, 0.06 Yb pfu; MA: 0.04 Dy pfu, 0.04 Yb pfu; PD: 0.04 Dy pfu, 0.07 Yb pfu. Rare elevated iron concentrations are in xenotime-(Y) from pegmatite dykes (0.03 Fe pfu). However, only few grains were studied and these concentrations must be taken only as approximate examples.

4.9.3 Monazite-(Ce)

Few monazite-(Ce) grains were analyzed in marginal Říčany granite, microgranite dykes, massive aplites, layered aplites, megacryst zones and pegmatite dykes.

Crystallochemical formulas were calculated on the basis of 4 oxygen atoms. The sums of analyzed oxides are too low (83.1-94.5 wt. %), therefore the measured concentrations must be taken only as approximate and emphasis should be put on the relative differences.

Monazite-(Ce) contains 0.90-1.00 P pfu (23.0-26.9 wt. % P_2O_5), 0.30-0.44 Ce pfu (17.5-27.7 wt. % Ce_2O_3) – the highest concentrations are in monazite-(Ce) from marginal Říčany granite, 0.12-0.18 and in monazite-(Ce) from marginal Říčany granite 0.25-0.26 La pfu (6.8-11.4 and 15.5-16.1 wt. % La_2O_3), 0.12-0.17 Nd pfu (7.1-10.6 wt. % Nd_2O_3), 0.12-0.24 Th pfu (12.3-22.1 wt. % ThO_2), 0.09-0.14 and in monazite-(Ce) from marginal Říčany granite 0.04-0.05 Ca pfu (1.9-2.8 and 0.9-1.1 wt. % CaO), 0.03-0.09 and in monazite-(Ce) from layered aplites 0.14 Si pfu (0.6-2.2 and 2.9 wt. % SiO_2), and up to 0.02 U pfu (up to 2.2 wt. % UO_2. In monazite-(Ce) from layered aplites are the only elevated concentrations of aluminium and strontium (0.02 Al pfu, 0.02 Sr pfu). Concentrations of Sm_2O_3 only rarely exceed the detection limit (2σ = 0.26 wt. % Sm_2O_3, up to 2.0 wt. % Sm_2O_3, up to 0.03 Sm pfu).

4.10 Accessory silicates and oxides

4.10.1 Zircon

Zircon was analyzed in marginal Říčany granite, microgranite and aplite dykes, layered aplites, pegmatite layers, megacryst zones and pegmatite dykes. Crystallochemical formulas were calculated on the basis of 1 cation in dodecahedral site (A site when using the general crystallochemical formula ATO_4). Exploratory recalculations of crystallochemical formulas based on 4 oxygen atoms lead to violation of individual site occupancies.

Sums of analyzed oxides in zircon vary from 70.3 up to 99.5 wt. % of oxides. ZrO_2, SiO_2 and CaO concentrations in individual zircon grains correspond to their sums of analyzed oxides, the lower is the sum of oxides, the lower is the sum of ZrO_2 and SiO_2 concentrations (0.78-0.97 Zr pfu, 38.3-65.4 wt. % ZrO_2; 0.61-0.97 Si pfu, 18.9-31.8 wt. % SiO_2) and the higher is CaO concentration (up to 0.09 Ca pfu, up to 2.0 wt. % CaO). Low sum of oxides in zircon indicates presence of OH^- group (incorporation mechanisms for H in zircon: Botis et al., 2013). Zircon further contains 0.01-0.06 Hf pfu (0.8-6.4 wt. % HfO_2), 0.00-0.03 and rarely up to 0.07 Th pfu (0.0-3.5 and 8.0 wt. % ThO_2), up to 0.01 U pfu (up to 1.7 wt. % UO_2), 0.01-0.05 Fe pfu (0.3-1.8 wt. % FeO), up to 0.14 Al pfu (up to 3.1 wt. % Al_2O_3), up to 0.02 Ti pfu (up to 0.6 wt. % TiO_2), up to 0.12 F pfu (up to 1.0 wt. % F), rarely up to 0.04 K pfu (up to 0.7 wt. % K_2O), rarely up to 0.02 Ce pfu (up to 1.3 wt. % Ce_2O_3), and rarely up to 0.02 Sc pfu (up to 0.4 wt. % Sc_2O_3).

Zircons from marginal Říčany granite and aplite dykes have the lowest concentrations of hafnium and some zircons from pegmatite dykes have the highest concentrations of thorium or hafnium and they tend to have elevated concentrations of scandium. Zircons from microgranite dykes have the highest contents of fluorine (0.11-0.12 F pfu), zircons from megacryst zones and one zircon from pegmatite dyke have medium contents of fluorine (0.06-

0.08 F pfu) and the rest of zircons from other units is fluorine-free. Other differences in zircon composition correspond to the sum of oxides in the zircon, which does not differ according to the unit the zircon is from, but probably indicates the degree of alteration of the individual zircon grains.

4.10.2 Rutile

Rutile was analyzed in marginal Říčany granite, aplite dykes, massive aplites, pegmatite layers, pegmatite pockets and pegmatite dykes. Crystallochemical formulas were calculated on the basis of 2 oxygen atoms (Tab. 4.5).

Rutile contains 0.75-0.98 Ti pfu (65.3-96.5 wt. % TiO_2), 0.01-0.10 and rarely up to 0.13 Nb pfu (0.8-14.0 and 18.3 wt. % Nb_2O_5), up to 0.08 Fe pfu (0.3-6.5 wt. % FeO), up to 0.02 and rarely up to 0.03 Ta pfu (up to 5.2 and 7.8 wt. % Ta_2O_5), up to 0.02 and rarely up to 0.03 Sn pfu (up to 3.5 and 4.7 wt. % SnO_2), up to 0.02 Si pfu (up to 1.5 wt. % SiO_2), up to 0.01 and rarely up to 0.02 Al pfu (up to 0.9 and 1.4 wt. % Al_2O_3), rarely up to 0.01 Cr pfu (up to 0.6 wt. % Cr_2O_3), and up to 0.004 W pfu (up to 1.1 wt. % WO_3). MnO, CaO, K_2O, V_2O_5, ZrO_2 and Sc_2O_3 concentrations only rarely exceed their detection limits (2σ = 0.13 wt. % MnO, 2σ = 0.06 wt. % CaO, 2σ = 0.05 wt. % K_2O, 2σ = 0.11-0.16 wt. % V_2O_5, 2σ = 0.16-0.19 wt. % ZrO_2, 2σ = 0.06-0.09 wt. % Sc_2O_3). Rutile forms a linear trend in the diagram Fe + Mn *vs.* Nb + Ta (Fig. 4.14).

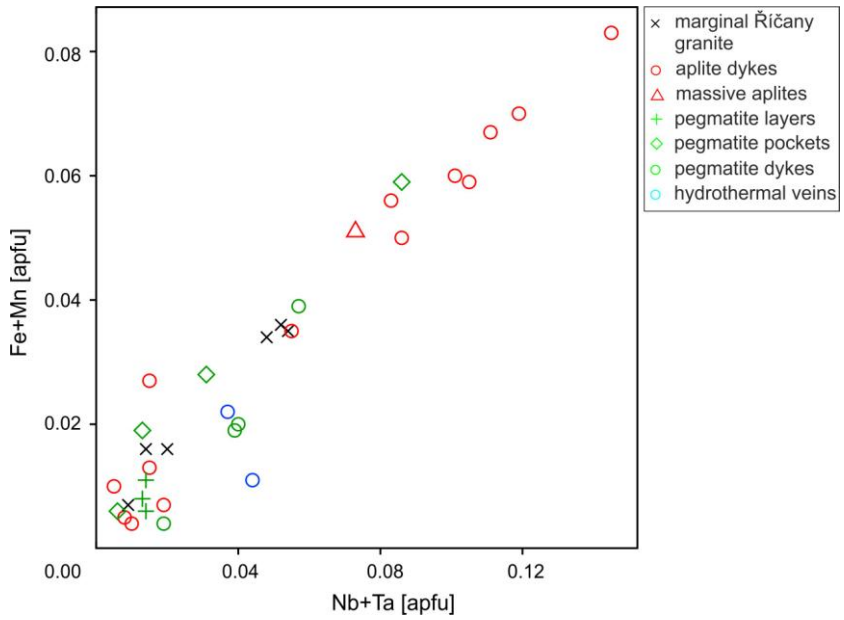

Fig. 4.14 Rutile molar composition. Fe + Mn [apfu] *vs.* Nb + Ta [apfu] diagram.

Rutiles from marginal Říčany granite, which are usually associated with biotites, have high titanium contents (0.90-0.98 Ti pfu), but they can be depleted in Ti (down to 0.75 Ti pfu) near aplite dykes, where they can have up to 0.13 Nb pfu or up to 0.08 Fe pfu. Rutiles from marginal Říčany granite have also the highest contents of calcium, vanadium and chromium. Rutiles from aplite dykes as well as rutiles from homogeneous aplites can have up to 0.09 Nb

pfu and up to 0.07 Fe pfu, they have 0.80-0.90 Ti pfu and the highest contents of tantalum, wolfram and tin. Rutiles from pegmatite pockets have 0.83-0.96 Ti pfu and but they differ according to the individual pegmatite pockets. Rutiles from pegmatite dykes have 0.87-0.96 Ti pfu and have the highest contents of scandium and tin.

4.10.3 Cassiterite

Few cassiterite grains were analyzed in microgranite dykes, pegmatite layers, megacryst zones and pegmatite dykes. Crystallochemical formulas were calculated on the basis of 2 oxygen atoms (Tab. 4.5).

Cassiterite is very pure with 0.96-0.98 Sn pfu (96.1-99.4 wt. % SnO_2). It further contains 0.01-0.03 Ti pfu (0.4-1.5 wt. % TiO_2), up to 0.01 Ta pfu (0.8-1.5 wt. % Ta_2O_5), up to 0.005 Nb pfu (up to 0.5 wt. % Nb_2O_5), and up to 0.005 Fe pfu (up to 0.2 wt. % FeO). WO_3, ZrO_2, and SiO_2 concentrations only rarely exceed their detection limits (2σ = 0.20 wt. % WO_3, 2σ = 0.16-0.19 wt. % ZrO_2, 2σ = 0.17 wt. % SiO_2).

Cassiterite from microgranite dykes and pegmatite layers has the lowest titanium contents (0.01 Ti pfu), cassiterite from megacryst zones has 0.02 Ti pfu and cassiterite from pegmatite dykes has 0.02-0.03 Ti pfu. However, only few grains were studied.

4.10.4 Columbite-tantalite

Few grains of columbite-tantalite were analysed in aplite dykes, layered aplites, pegmatite layers and pegmatite dykes. Crystallochemical formulas were calculated on the basis of 3 cations and for the columbites-tantalites in pegmatite dykes on the basis of 6 oxygen atoms (Tab. 4.5). Recalculations of crystallochemical formulas based on 6 oxygen atoms lead to wrong charge-balance in all the crystals except crystals in pegmatite dykes, and part of ferrous iron had to be recalculated on ferric form.

In columbites-tantalites predominates the columbite component with 1.40-1.66 Nb pfu (49.5-62.2 wt. % Nb_2O_5). The columbite-tantalite grains further contain 0.07-0.43 Ta pfu (4.9-25.1 wt. % Ta_2O_5), 0.13-0.89 Mn pfu (2.7-17.4 wt. % MnO), 0.07-0.63 Fe^{2+} pfu, 0.00-0.20 Fe^{3+} pfu (1.3-15.9 wt. % FeO), 0.13-0.29 Ti pfu (2.8-6.9 wt. % TiO_2), 0.01-0.03 Sn pfu (0.5-1.6 wt. % SnO_2), up to 0.07 W pfu (up to 4.2 wt. % WO_3), and up to 0.12 Si pfu (up to 2.1 wt. % SiO_2). Al_2O_3, ZrO_2 and Sc_2O_3 concentrations only rarely exceed their detection limits (2σ = 0.04-0.08 wt. % Al_2O_3, 2σ = 0.19-0.26 wt. % ZrO_2, 2σ = 0.08-0.09 wt. % Sc_2O_3).

Columbite-tantalite from pegmatite dykes has the highest manganese content (0.87-0.89 Mn pfu), the lowest iron content (0.07-0.09 Fe^{2+} pfu, 0.00 Fe^{3+} pfu), and the highest tantalium content (0.16-0.43 Ta pfu). There are no other systematic differences in composition of columbites-tantalites from different units.

4.10.5 Ilmenite-pyrophanite

Only two grains of ilmenite-pyrophanite were analysed in massive aplites and pegmatite layers. Crystallochemical formulas were calculated on the basis of 3 oxygen atoms (Tab. 4.5).

Ilmenite-pyrophanite grains contain 0.99 Ti pfu (51.6-52.1 wt. % TiO_2), 0.36-0.53 Fe pfu (16.9-25.4 wt. % FeO), 0.46-0.62 Mn pfu (21.7-28.7 wt. % MnO), and 0.01 Nb pfu (0.8-1.2 wt. % Nb_2O_5). The grain in massive aplites is slightly more iron-rich (ilmenite) and the grain in pegmatite layer is more manganese-rich (pyrophanite).

Tab. 4.5 Representative chemical composition of accessory oxides.

Sample	TD2	DT20/1	ZV2A	DT5/2	DTX3	DT10	TDX2	TJ6A	TJ22A
Analysis	64	34	31	9	20	16	50	31	44
Group	PL	MZ	MA	G	AD	PP	AD	PL	PD
mineral	cass	cass	ilm	rut	rut	rut	col	col	col
SiO_2 (*wt.%*)	0.193	*n.d.*	0.244	0.218	0.585	0.295	1.691	1.352	*n.d.*
TiO_2	0.423	1.163	52.102	96.455	72.877	90.350	5.340	2.944	2.764
Al_2O_3	*n.d.*	*n.d.*	*n.d.*	0.082	0.320	0.124	*n.d.*	*n.d.*	*n.d.*
FeO	*n.d.*	*n.d.*	25.363	0.645	4.854	2.410	15.912	12.409	1.255
MnO	*n.d.*	*n.d.*	21.701	*n.d.*	*n.d.*	*n.d.*	2.723	8.207	16.832
Nb_2O_5	0.252	0.410	0.764	1.521	12.308	4.649	61.919	59.864	49.528
Ta_2O_5	0.773	0.804	*n.d.*	*n.d.*	4.629	0.648	6.049	11.371	25.105
SnO_2	98.957	98.058	*n.d.*	0.152	2.592	1.861	1.270	0.645	0.553
ZrO_2	0.166	*n.d.*	*n.d.*	*n.d.*	*n.d.*	*n.d.*	0.377	*n.d.*	*n.d.*
WO_3	*n.d.*	0.257	*n.d.*	*n.d.*	0.498	0.475	*n.d.*	2.927	4.231
Cr_2O_3	*n.d.*	*n.d.*	*n.d.*	0.124	*n.d.*	*n.d.*	*n.d.*	*n.d.*	*n.d.*
Sc_2O_3	*n.d.*	*n.d.*	*n.d.*	*n.d.*	*n.d.*	*n.d.*	0.804	*n.d.*	*n.d.*
Total	100.898	100.743	100.264	99.196	98.662	100.812	96.099	99.720	100.268
	(*per 2 O*)	(*per 2 O*)	(*per 3 O*)	(*per 2 O*)	(*per 2 O*)	(*per 2 O*)	(*per 3 cat*)	(*per 3 cat*)	(*per 6 O*)
Si	0.005	-	0.006	0.003	0.009	0.004	0.097	0.078	-
Al	-	-	-	0.001	0.006	0.002	-	-	-
Ti	0.008	0.022	0.985	0.979	0.812	0.929	0.230	0.128	0.130
W	-	0.002	-	-	0.002	0.002	-	0.044	0.068
Nb	0.003	0.005	0.009	0.009	0.082	0.029	1.604	1.559	1.396
Fe^{3+}	-	-	-	-	-	-	0.132	0.172	-
Sn	0.975	0.964	-	0.001	0.015	0.010	0.029	0.015	0.014
Zr	0.002	-	-	-	-	-	0.011	-	-
Cr	-	-	-	0.001	-	-	-	-	-
Fe_{tot}	-	-	0.533	0.007	0.060	0.028	0.762	0.598	0.065
Ta	0.005	0.005	-	-	0.019	0.002	0.094	0.178	0.426
Mn	-	-	0.462	-	-	-	0.132	0.401	0.889
Sc	-	-	-	-	-	-	0.040	-	-
Total cat.	0.998	0.997	1.995	1.002	1.005	1.006	3.000	3.000	2.988
Total O	2.000	2.000	3.000	2.000	2.000	2.000	5.934	5.914	6.000

n.d. – below detection limit, cass – cassiterite, ilm – ilmenite-pyrophanite, rut – rutile, col – columbite-tantalite, G – Říčany granite, AD – aplite dykes, MA-massive aplites, PL – pegmatite layers, MZ – megacryst zones, PP – pegmatite pockets, PD – pegmatite dykes

5 Whole-rock geochemistry

5.1 Analytical methods

Samples of rocks from the aplite-pegmatite belt were analyzed for whole-rock geochemistry in Acme Labs (Canada, http://acmelab.com/) and Activation Laboratories (Canada, http://www.actlabs.com/). Major, minor, as well as trace elements were analysed using both ICP-ES (inductively coupled plasma emission spectrometry) and ICP-MS (inductively coupled plasma mass spectrometry) methods (code 1DX and 4A-4B in Acme Labs and WRA + trace 4Lithoresearch in Actlabs). The detection limits in Actlabs were 0.01 wt. % for SiO_2, Al_2O_3, Fe_2O_{3tot}, MgO, CaO, Na_2O, K_2O, P_2O_5; 0.001 wt. % for MnO and TiO_2; 5 ppm for V; 2 ppm for Zr, Sr, Ba; 1 ppm for Mn, B, Be, Sc, Y; 0.5 ppm for La, Cr; 0.1 ppm for As, Co, Er, Eu, Ge, Gd, Hf, Ho, Li, Lu, Nb, Ni, Pr, Rb, Se, Sm, Tb, Th, Tm, U, Yb, Zn; 0.05 ppm for Ta, Sn; 0.02 ppm for Bi, Cs, Ga, In, Nd, Sb, Te, Tl; 0.01 ppm for Pb, Ce, Cd, Cu, Mo; 0.002 ppm for Ag; 0.001 ppm for Dy, Re; and 0.5 ppb for Au. The detection limits in Acme Labs were 0.05 wt. % for S; 0.04 wt. % for Fe_2O_{3tot}; 0.02 wt. % for total C; 0.01 wt. % for SiO_2, TiO_2, Al_2O_3, MgO, MnO, CaO, Na_2O, K_2O; 0.002 wt. % for Cr_2O_3; 0.001 wt. % for P_2O_5; 20 ppm for B, Ni; 8 ppm for V; 1 ppm for Ba, Be, Ga, La, Sc, Sn, Sr, Zn; 0.5 ppm for As, Se, W; 0.3 ppm for Nd; 0.2 ppm for Co, Th; 0.1 ppm for Ag, Bi, Cd, Ce, Cs, Cu, Hf, Mo, Nb, Pb, Rb, Sb, Ta, Tl, U, Y, Zr; 0.05 ppm for Dy, Gd, Sm, Yb; 0.03 ppm for Er; 0.02 ppm for Eu, Ho, Pr; 0.01 ppm for Hg, Lu, Tb, Tm; and 0.5 ppb for Au. Analyses of the samples from the Říčany granite have been taken from the thesis of Trubač (2008) (Acme Labs, ICP-ES and ICP-MS). Analyses for boron were performed in the Geological laboratories of the Charles University in Prague, and analyses for lithium and fluor were performed in the laboratories of the Czech Geological Society, Prague. For more information about methods please contact these laboratories. Interpretation and plotting of the whole-rock geochemical data was facilitated by the freeware R-language package *GCDkit*, version 3.0 (Janoušek et al., 2006).

5.2 Results

The content of major as well as minor and trace elements was analysed in 19 samples of rocks from the aplite-pegmatite belt, and 22 analyses of the Říčany granite were used. The compositions of analysed samples from the aplite-pegmatite belt and the mean of the analysed samples of the Říčany granite from Trubač (2008) can be found in Tab. 5.1. Remarkable is the high content of SiO_2 in the rocks from the aplite-pegmatite belt (73.6-77.4 wt. % SiO_2) and the varying content of B_2O_3 in the rocks from the aplite-pegmatite belt, which is in average very high (0.00-0.40 wt. % B_2O_3).

Tab. 5.1 Whole-rock composition of analysed samples.

Sample	RIC1	OAP6	DT27B	DT30	JT2	DT7B/1	DT7B/2	DT14	JT30A	JT30B
Group	G	GR	MG	MG	AD	MA	MA	MA	MA	MA
SiO_2 (*wt. %*)	70.90	67.99	75.42	75.49	75.25	77.40	75.25	77.40	75.07	75.06
TiO_2	0.29	0.36	0.09	0.07	0.08	0.08	0.18	0.05	0.05	0.05
Al_2O_3	14.76	14.90	14.70	14.78	14.19	13.39	14.30	13.64	14.07	14.27
FeO_{tot}	1.54	3.88	0.56	0.62	0.60	0.25	1.09	0.22	0.53	0.58
MnO	0.03	0.09	0.02	0.01	0.01	0.01	0.03	0.01	0.01	0.02
MgO	1.03	1.04	0.18	0.20	0.31	0.07	0.44	0.05	0.15	0.10
CaO	1.19	3.39	0.63	0.58	0.36	0.64	0.62	0.60	0.67	0.46
Na_2O	3.59	2.86	3.86	3.85	3.71	3.95	3.85	4.33	4.20	4.17
K_2O	5.25	2.60	4.45	4.55	4.79	4.63	4.34	4.15	4.11	4.70
P_2O_5	0.16	0.12	0.07	0.08	0.05	0.03	0.05	0.05	0.05	0.05
B_2O_3	-	-	0.19	0.37	0.38	0.10	0.21	0.08	0.29	0.32
F	-	0.06	0.06	0.04	0.06	0.03	0.09	0.02	0.04	0.03
LOI	0.67	1.02	0.91	0.70	0.60	0.50	0.84	0.50	1.10	0.50
Total	99.42	98.24	100.90	100.90	99.93	101.00	101.00	101.00	100.01	99.96
Test	-	98.30	101.14	101.34	100.38	101.07	101.29	101.11	100.35	100.30
Ag (*ppm*)	-	1.00	-	-	0.10	-	-	-	0.10	0.10
As	9.79	13.00	9.00	33.00	4.60	-	-	-	1.20	2.60
Ba	860.64	1409.00	161.00	168.00	48.00	22.00	93.00	18.00	90.00	37.00
Be	13.09	2.00	8.00	6.00	9.00	20.00	11.00	8.00	15.00	21.00
Bi	1.24	-	1.30	4.60	2.50	3.20	2.50	0.80	3.30	4.10
Co	3.80	5.00	-	-	0.50	-	-	-	0.10	0.10
Cr	35.14	-	-	-	1.00	-	-	-	1.00	1.00
Cs	41.15	16.30	44.70	25.90	57.30	32.60	42.70	40.30	59.50	21.80
Cu	3.55	-	-	-	0.40	-	-	-	0.50	0.50
Ga	22.80	16.00	23.00	20.00	22.60	19.00	25.00	21.00	21.50	24.90
Ge	-	1.80	2.60	2.70	-	2.40	2.50	2.80	-	-
Hf	6.85	3.70	1.10	1.40	1.60	0.60	3.10	1.30	1.60	1.00
Li	-	82.06	140.00	30.00	10.00	30.00	160.00	20.00	20.00	10.00
Mo	0.23	-	-	-	0.10	-	-	-	0.10	0.10
Nb	18.50	5.80	7.30	0.70	18.40	24.40	13.10	8.30	6.60	19.10
Ni	14.05	-	-	-	1.70	-	-	-	0.30	0.90
Pb	13.05	17.00	53.00	65.00	21.30	68.00	65.00	49.00	4.90	4.20
Rb	338.35	107.00	352.00	327.00	393.40	350.00	369.00	353.00	259.80	354.40
Sb	0.45	0.30	0.30	-	0.30	0.50	0.40	-	0.10	0.10
Sc	3.21	8.00	4.00	3.00	0.20	1.00	5.00	2.00	0.20	0.20
Sn	17.55	6.00	38.00	19.00	18.00	25.00	38.00	23.00	24.00	15.00
Sr	332.50	370.00	67.00	63.00	38.10	35.00	57.00	16.00	41.80	15.90
Ta	2.86	0.54	2.05	1.66	7.40	11.40	4.59	4.33	2.10	7.90
Th	33.17	14.70	7.70	6.73	8.10	8.36	20.20	7.89	7.50	7.70
Tl	0.93	1.06	2.52	2.28	0.10	2.55	2.70	2.47	0.10	0.10
U	10.61	3.38	5.15	5.61	3.50	2.71	7.88	4.27	3.40	4.00
V	17.64	60.00	-	-	2.00	-	15.00	-	2.00	2.00
W	0.19	-	1.70	-	0.20	2.30	1.00	0.70	0.10	0.10
Y	10.75	18.90	11.60	12.20	10.30	4.50	19.40	11.80	10.30	10.30
Zn	41.55	40.00	-	-	4.00	-	40.00	-	1.00	1.00
Zr	203.72	146.00	30.00	33.00	31.20	12.00	78.00	21.00	25.20	15.50
La	31.41	28.80	7.78	6.64	6.00	3.32	15.80	4.05	4.10	3.90
Ce	62.68	50.00	16.00	13.50	12.60	6.66	32.30	8.69	9.00	7.70
Pr	7.15	5.85	1.78	1.48	1.54	0.75	3.57	1.01	1.16	1.12
Nd	25.45	21.20	6.64	5.68	5.70	2.62	12.90	3.42	3.80	4.50
Sm	4.17	4.27	1.68	1.46	1.30	0.68	3.09	1.23	1.23	1.20
Eu	0.69	0.98	0.19	0.19	0.09	0.06	0.12	0.02	0.11	0.05
Gd	2.78	3.78	1.62	1.48	1.21	0.58	2.75	1.28	1.13	1.17
Tb	0.39	0.55	0.29	0.29	0.25	0.11	0.50	0.25	0.24	0.26
Dy	2.00	3.28	1.89	1.87	1.60	0.73	3.09	1.70	1.59	1.51
Ho	0.34	0.65	0.39	0.39	0.32	0.16	0.66	0.38	0.32	0.31
Er	0.94	1.98	1.19	1.19	0.94	0.48	2.02	1.16	1.03	0.94

Tm	0.15	0.31	0.19	0.19	0.17	0.07	0.31	0.20	0.18	0.16
Yb	0.89	2.06	1.24	1.25	1.03	0.49	2.07	1.33	1.09	1.09
Lu	0.12	0.33	0.19	0.21	0.14	0.08	0.34	0.21	0.17	0.15
Eu*	1.18	1.34	0.55	0.49	0.42	0.21	0.97	0.41	0.39	0.39
Eu/Eu*	0.58	0.73	0.35	0.39	0.22	0.29	0.13	0.06	0.28	0.13
Nb/Ta	6.46	10.74	3.56	0.42	2.49	2.14	2.85	1.92	3.14	2.42
Zr/Hf	29.72	39.46	27.27	23.57	19.50	20.00	25.16	16.15	15.75	15.50
Th/Ta	11.58	27.22	3.76	4.05	1.09	0.73	4.40	1.82	3.57	0.97
Ba/La	27.40	48.92	20.69	25.30	8.00	6.63	5.89	4.44	21.95	9.49
Rb/Sr	1.02	0.29	5.25	5.19	10.33	10.00	6.47	22.06	6.22	22.29
K/Rb	128.91	201.73	104.95	115.52	101.08	109.82	97.64	97.60	131.34	110.10
ΣREE	139.18	124.04	41.07	35.81	32.89	16.80	79.52	24.93	25.15	24.06

RIC1 is a mean of all the analysed samples of the Říčany granite from Trubač (2008). G – Říčany granite, GR – granodiorite, MG – microgranite dykes, AD – aplite dykes, MA – massive aplites, LA – layered aplites, MZ – megacryst zones, PP – pegmatite pockets, [-] – not measured

Tab. 5.1 Whole-rock composition of analysed samples-continued.

Sample	JT72	JT73	OAP2	TD1	TJ7B	DT20	TJ13A/1	TJ13A/2	OAP3	PEG
Group	MA	MA	LA	LA	LA	MG	MG	MG	PP	PP
SiO_2 (*wt. %*)	75.47	75.80	74.04	75.36	75.27	74.20	76.24	74.02	73.64	75.16
TiO_2	0.05	0.09	0.05	0.03	0.04	0.05	0.05	0.05	0.03	0.04
Al_2O_3	12.90	13.45	13.80	13.40	14.23	14.22	14.12	14.30	14.34	13.95
FeO_{tot}	0.32	0.44	0.65	0.56	0.63	0.62	0.63	0.65	0.26	0.37
MnO	0.01	0.02	0.02	0.02	0.02	0.02	0.02	0.01	0.01	0.01
MgO	0.08	0.11	0.14	0.07	0.11	0.12	0.12	0.14	0.07	0.04
CaO	0.54	0.58	0.58	0.42	0.42	0.40	0.43	0.32	0.32	0.26
Na_2O	3.94	4.11	3.68	4.23	4.62	4.23	4.50	3.70	3.83	3.80
K_2O	4.43	3.97	4.79	3.89	3.55	4.24	3.78	5.39	6.12	5.77
P_2O_5	0.02	0.06	0.07	0.07	0.07	0.07	0.07	0.05	0.12	0.10
B_2O_3	0.13	0.19	0.40	0.29	0.35	0.36	0.36	0.40	0.12	0.15
F	0.03	0.05	0.04	0.03	0.04	0.04	0.04	0.03	0.02	0.02
LOI	0.49	1.45	1.12	0.44	0.52	0.38	0.50	0.50	1.12	0.46
Total	98.24	100.10	98.93	98.48	99.47	98.55	100.50	99.15	99.85	99.95
Test	98.42	100.32	99.38	98.81	99.87	98.94	100.86	99.57	100.00	100.13
Ag (*ppm*)	-	-	-	-	-	-	-	-	-	-
As	-	-	-	-	-	-	-	-	-	5.00
Ba	15.00	20.00	88.00	20.00	37.00	26.00	21.00	22.00	52.00	35.00
Be	12.00	17.00	7.00	69.00	64.00	128.00	19.00	8.00	41.00	112.00
Bi	1.00	2.40	2.00	1.60	0.40	3.70	2.90	1.30	-	0.50
Co	-	-	-	-	-	-	-	-	-	-
Cr	-	-	-	-	-	-	-	-	-	-
Cs	142.00	73.30	56.10	17.90	19.80	61.90	24.60	22.10	35.20	34.20
Cu	-	-	-	-	-	-	-	-	-	-
Ga	22.00	25.00	21.00	25.00	29.00	30.00	24.00	28.00	22.00	22.00
Ge	2.60	2.50	2.40	4.00	4.00	4.70	3.30	3.30	4.30	4.60
Hf	1.40	1.60	2.50	1.40	1.30	2.50	1.60	0.60	0.40	0.40
Li	60.00	79.21	24.79	10.00	10.00	10.00	10.00	10.00	11.18	10.00
Mo	-	-	-	-	-	-	-	-	-	-
Nb	12.00	15.20	5.60	8.70	20.40	10.80	4.70	6.40	3.20	5.10
Ni	-	-	-	-	-	-	-	-	-	-
Pb	64.00	50.00	54.00	32.00	31.00	37.00	34.00	41.00	36.00	36.00
Rb	412.00	373.00	292.00	327.00	358.00	490.00	385.00	473.00	613.00	606.00
Sb	1.10	0.30	-	-	-	0.20	-	0.30	-	-
Sc	1.00	4.00	1.00	1.00	3.00	3.00	3.00	4.00	-	1.00
Sn	39.00	37.00	21.00	11.00	44.00	23.00	26.00	24.00	14.00	22.00
Sr	33.00	24.00	29.00	8.00	10.00	11.00	9.00	10.00	34.00	24.00
Ta	5.75	4.30	2.53	3.75	8.48	7.03	3.56	3.32	2.70	9.28

Th	7.81	8.08	7.93	5.51	7.11	6.22	6.95	6.74	0.98	1.40
Tl	3.01	2.19	1.60	1.90	2.38	3.85	2.61	3.57	3.43	4.00
U	3.02	4.24	7.62	2.74	4.52	2.56	2.81	1.69	1.15	1.31
V	-	-	-	-	6.00	-	-	-	-	-
W	-	-	-	-	1.50	5.20	-	-	-	-
Y	11.10	12.70	18.30	8.60	8.90	8.10	9.60	9.10	1.30	1.70
Zn	-	-	-	-	30.00	-	-	-	-	-
Zr	26.00	29.00	49.00	19.00	16.00	28.00	20.00	8.00	5.00	4.00
La	4.27	4.42	4.41	2.79	3.05	2.70	3.22	3.44	0.36	0.90
Ce	9.12	9.11	9.27	5.14	7.05	5.40	6.69	7.43	0.69	1.68
Pr	1.04	1.07	1.10	0.65	0.86	0.70	0.85	0.92	0.08	0.20
Nd	3.62	3.62	3.93	2.45	3.05	2.48	3.19	3.05	0.34	0.66
Sm	0.98	1.20	1.33	0.93	1.16	0.86	1.02	1.03	0.10	0.20
Eu	0.07	0.03	0.05	0.01	0.02	0.03	0.02	0.04	0.04	0.03
Gd	1.04	1.23	1.54	0.92	1.09	0.80	1.07	0.97	0.09	0.22
Tb	0.23	0.27	0.37	0.19	0.20	0.17	0.21	0.21	0.02	0.04
Dy	1.57	1.80	2.48	1.24	1.34	1.19	1.35	1.36	0.16	0.24
Ho	0.35	0.35	0.49	0.28	0.29	0.25	0.30	0.29	0.03	0.05
Er	1.11	1.12	1.56	0.87	0.94	0.79	0.98	0.91	0.11	0.17
Tm	0.18	0.19	0.29	0.14	0.17	0.15	0.16	0.16	0.02	0.03
Yb	1.21	1.36	2.09	0.95	1.15	1.12	1.21	1.14	0.15	0.25
Lu	0.20	0.20	0.30	0.16	0.18	0.18	0.21	0.18	0.02	0.04
Eu*	0.33	0.40	0.47	0.31	0.37	0.28	0.34	0.33	0.03	0.07
Eu/Eu*	0.20	0.07	0.11	0.04	0.05	0.09	0.07	0.13	1.27	0.46
Nb/Ta	2.09	3.53	2.21	2.32	2.41	1.54	1.32	1.93	1.19	0.55
Zr/Hf	18.57	18.13	19.60	13.57	12.31	11.20	12.50	13.33	12.50	10.00
Th/Ta	1.36	1.88	3.13	1.47	0.84	0.88	1.95	2.03	0.36	0.15
Ba/La	3.51	4.52	19.95	7.17	12.13	9.63	6.52	6.40	144.44	38.89
Rb/Sr	12.48	15.54	10.07	40.88	35.80	44.55	42.78	47.30	18.03	25.25
K/Rb	89.27	88.36	136.19	98.76	82.32	71.84	81.51	94.60	82.88	79.05
ΣREE	24.98	25.97	29.22	16.72	20.55	16.81	20.48	21.13	2.21	4.72

G – Říčany granite, GR – granodiorite, MG – microgranite dykes, AD – aplite dykes, MA – massive aplites, LA – layered aplites, MZ – megacryst zones, PP – pegmatite pockets, [-] – not measured

5.2.1 Petrographical classification diagrams

All the rock samples of the Říčany granite and rocks from the aplite-pegmatite belt plot in the granite field of the O'Connor petrographical classification diagram (O'Connor, 1965), based on the modal (normative) abundance of K-feldspar, albite and anorthite (Fig. 5.1). The rocks from the aplite-pegmatite belt form a trend toward bigger abundance of albite (more Na) and are depleted in anorthite (less Ca) relatively to the Říčany granite. The marginal unit of biotite granodiorite in the aplite-pegmatite belt plots indeed in the granodiorite field and it is much richer in anorthite relatively to all the other samples.

When plotted in the Q'-ANOR diagram of Streckeisen and Le Maitre (1979), which is only modified QAPF diagram, the rocks can be further distinguished (Fig. 5.1). The majority of samples of the Říčany granite plots in the field of syenogranite, whereas the samples from the aplite-pegmatite belt extend from the syenogranite into the alkali-feldspar granite field (there are mainly samples from pegmatite pockets and megacryst zones groups). That means that the rocks from the aplite-pegmatite belt are in average enriched in orthoclase relatively to anorthite and the Říčany granite, which is caused probably by their lower anorthite contents (as visible in the O'Connor diagram). However, the biggest differences within both rock suites are in the proportion of quartz relatively to feldspars (along the Q' axis), but in average

have the rocks from the aplite-pegmatite belt more quartz relatively to feldspars than the Říčany granite. The marginal unit of biotite granodiorite in the aplite-pegmatite belt plots near the field of granodiorite, but already in the tonalite field, and has a relatively high proportion of quartz relatively to feldspars in comparison with the other units.

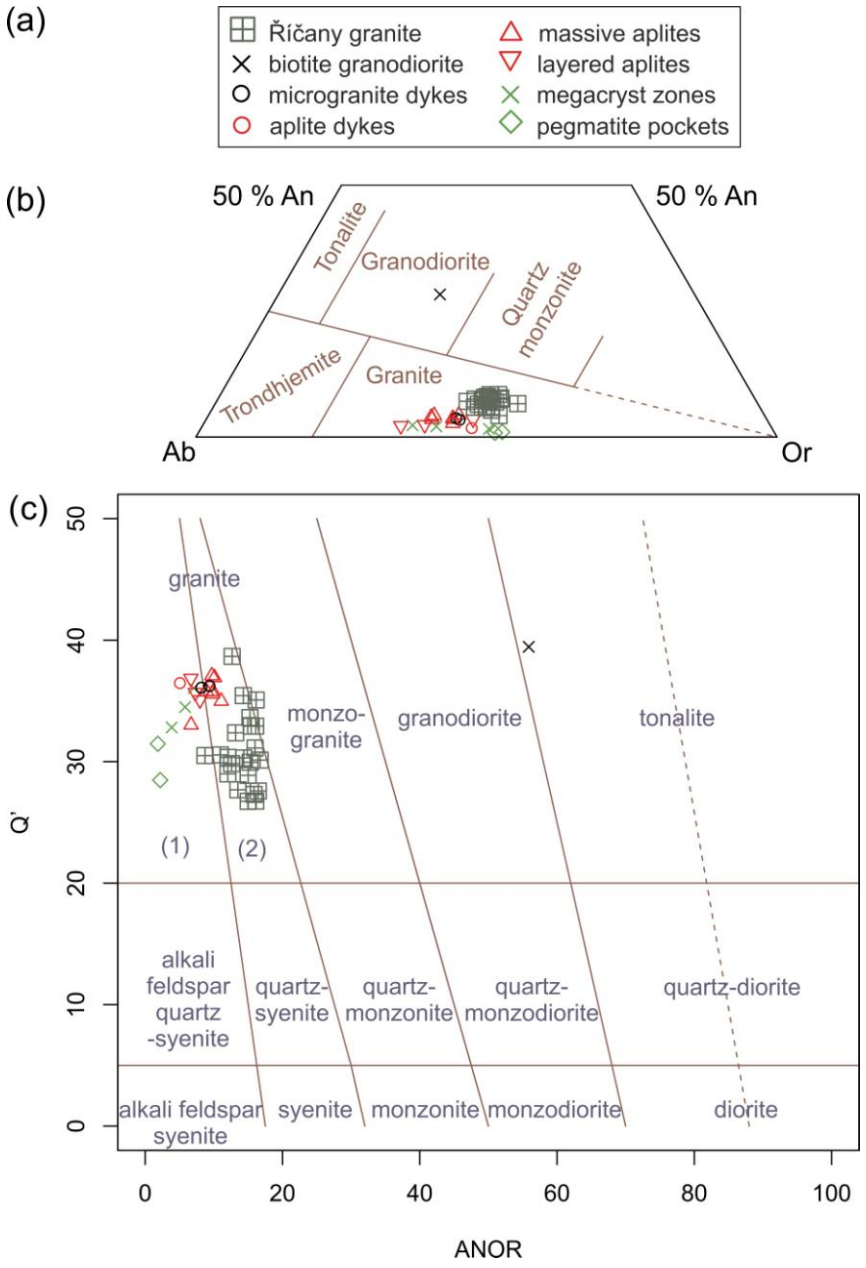

Fig. 5.1 Position of the analysed samples in petrographical classification diagrams. (a) symbols used for the rock groups (b) O'Connor's triangular petrographical classification diagram designed for rocks with more than 10 % of quartz (O'Connor, 1965). An, Ab, Or are normative contents of anorthite, albite and orthoclase end-members in the analysed samples, respectively (recalculated after Hutchison 1974, 1975). (c) Q'-ANOR petrographical classification diagram (Streckeisen and Le Maitre, 1979). Q' = (Q / (Q + Or + Ab + An)) * 100 and ANOR = (An / (Or + An)) * 100, where Q, Or, Ab and An are normative contents of quartz, orthoclase, albite and anorthite in the analysed samples (recalculated with a mesonorm of Mielke and Winkler, 1979).

5.2.2 Variation diagrams

In order to properly investigate the chemical evolution within and between the rock units, various variation diagrams are useful (Fig. 5.2 and Fig. 5.3). The most important thing, which can be observed in the variation diagrams, is that the Říčany granite and the rocks from the aplite-pegmatite belt form two distinctly separated groups in all of them, and the Říčany granite samples are usually more clustered together than the more dispersed aplite-pegmatite group (this suggests some further evolution within the aplite-pegmatite belt).

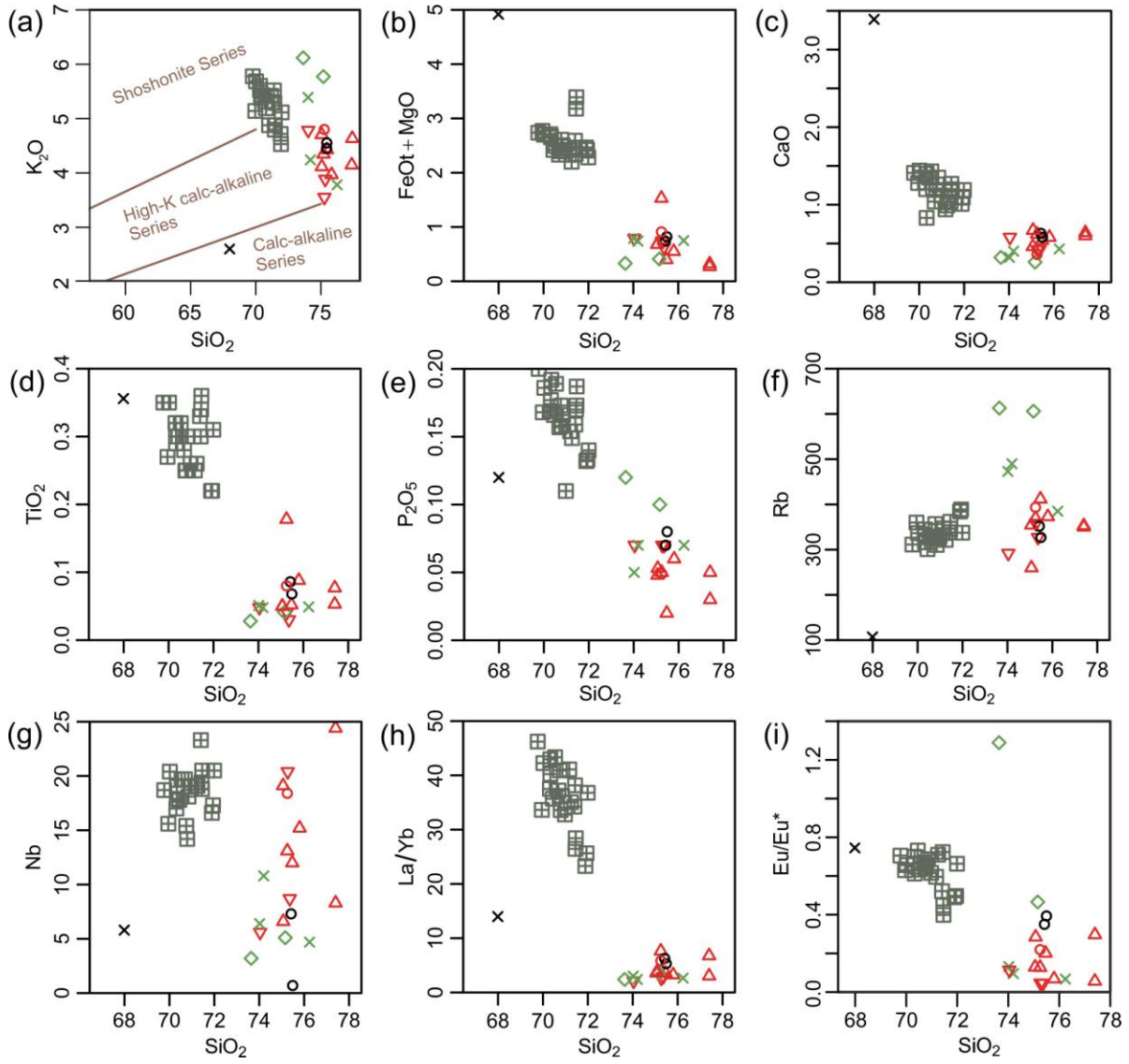

Fig. 5.2 Selected variations diagrams for the analysed samples (part 1 – depicted vs. SiO_2). All the oxides are in wt. % and all the elements are in ppm. (a) K_2O vs. SiO_2 with the classification fields of Peccerillo and Taylor 1976 (b) FeO_{tot} + MgO vs. SiO_2 (c) CaO vs. SiO_2 (d) TiO_2 vs. SiO_2 (e) P_2O_5 vs. SiO_2 (f) Rb vs. SiO_2 (g) Nb vs. SiO_2 (h) La/Yb vs. SiO_2 (i) Eu/Eu^* vs. SiO_2

The rocks from the aplite-pegmatite belt are depleted in almost all the major elements relatively to the Říčany granite (Říčany granite: 14.09-15.15 wt. % Al_2O_3, 4.53-5.78 wt. % K_2O, 0.83-1.44 wt. % CaO, 1.22-2.02 wt. % FeO_{tot}, 0.78-1.37 wt. % MgO, 0.01-0.04 wt. %

MnO, 0.22-0.36 TiO_2, 0.11-0.20 wt. % P_2O_5 and average 0.20 wt. % F according to Vejnar, 1973; rocks from the aplite-pegmatite belt: 12.90-14.78 wt. % Al_2O_3, 3.55-6.12 wt. % K_2O, 0.26-0.67 wt. % CaO, 0.22-1.09 wt. % FeO_{tot}, 0.04-0.44 wt. % MgO, 0.01-0.03 wt. % MnO, 0.03-0.18 TiO_2, 0.02-0.12 wt. % P_2O_5 and 0.02-0.09 wt. % F; other details can be seen in Tab. 5.1) except Si, Na and B (Říčany granite: 69.77-71.99 wt. % SiO_2, 2.83-3.77 wt. % Na_2O, average 0.04 wt. % B according to Vejnar, 1973; rocks from the aplite-pegmatite belt: 73.64-77.40 wt. % SiO_2, 3.68-4.62 wt. % Na_2O, 0.00-0.40 wt. % B_2O_3; Tab. 5.1). Within the samples from the aplite-pegmatite belt is no distinguishable trend between the units in major element composition, only the pegmatite samples have higher contents of K_2O and P_2O_5. The biotite granodiorite unit differs greatly as can be seen in Tab. 5.1.

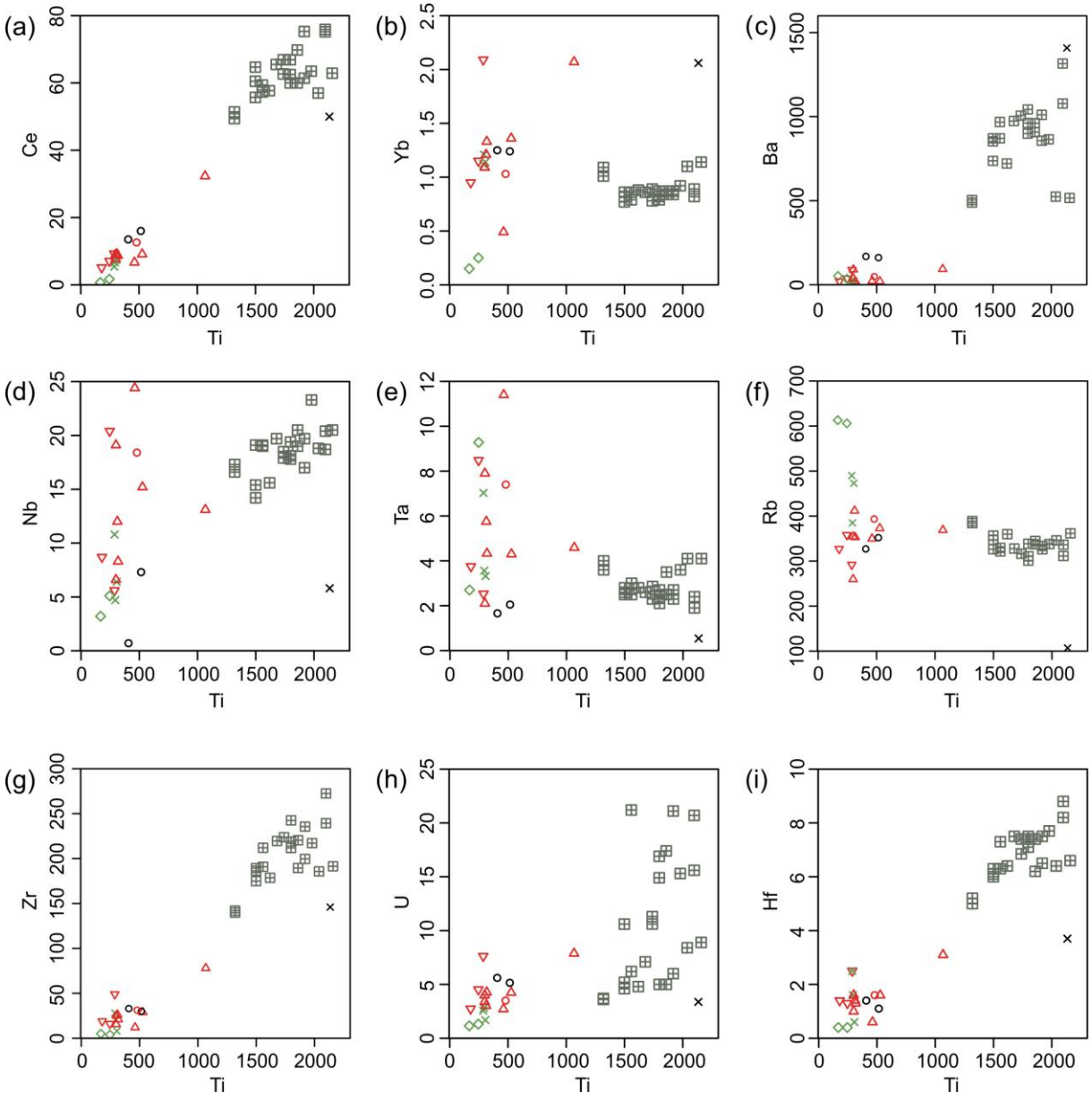

Fig. 5.3 Selected variations diagrams for the analysed samples (part 2 – depicted vs. Ti). All the values are in ppm. (a) Ce vs. Ti (b) Yb vs. Ti (c) Ba vs. Ti (d) Nb vs. Ti (e) Ta vs. Ti (f) Rb vs. Ti (g) Zr vs. Ti (h) U vs. Ti (i) Hf vs. Ti.

Concerning the trace element composition, the rocks from the aplite-pegmatite belt are enriched in Be, Sn, W, Ta and Pb relatively to the Říčany granite (Říčany granite: ~10.16 ppm Be, 8.31 ppm Sn, 0.1-0.3 ppm W, 1.9-4.1 ppm Ta, 7-21.5 ppm Pb; rocks from the aplite-pegmatite belt: 6.8-128 ppm Be, 11.4-38 ppm Sn, 0.1-5.2 ppm W, 1.7-11.4 ppm Ta, 21.3-65 ppm Pb). They are depleted in the transitional metals like Sc, V, Cr, Co, Ni, Cu, Zn, Zr, Nb; than in Sr, Ba, Th, U and LREE (La-Tb) (the most important values: Říčany granite: 222.1-471.6 ppm Sr, 489-1316 ppm Ba, 27.6-39.1 ppm Th, 3.6-21.2 ppm U; rocks from the aplite-pegmatite belt: 8.6-67 ppm Sr, 15-168 ppm Ba, 0.98-20.2 ppm Th, 1.2-7.9 ppm U). The elements, which have approximately the same range of values in both of the rock suites are Rb, Cs, Bi, Mo, Sb, Ga, Y and HREE (Dy-Hf). Within the samples from the aplite-pegmatite belt, pegmatites tend to have distinctly higher contents of Rb and Be, and lower contents of Zr, La, Ce and Nb.

5.2.3 Magmatic series

Granitic rocks can be specified with help of various parameters. Here are used mainly Fe^* value (weight proportion of FeO_{tot} / (FeO_{tot} + MgO)), modified alkali-lime index (MALI) ($Na_2O + K_2O - CaO$ in wt. %), aluminium saturation index (ASI) (molecular Al_2O_3 / ($CaO - 1.67P_2O_5 + Na_2O + K_2O$), A/NK value (molecular Al_2O_3 / ($Na_2O + K_2O$)) and A/CNK value (molecular Al_2O_3 / ($CaO + Na_2O + K_2O$)). All the analysed rock samples are peraluminous (ASI > 1.0; A/NK > 1.0; A/CNK > 1.0) according to both Frost et al. (2001) and Shand (1943) (Fig. 5.4). The ranges of ASI and A/CNK values are similar for both rock suites (ASI of Říčany granite = 1.43-1.64, ASI of samples from aplite-pegmatite belt = 1.43-1.68; A/CNK of Říčany granite = 1.01-1.18; A/CNK of samples from aplite-pegmatite belt = 1.05-1.20), but the samples from the aplite-pegmatite belt have lower A/NK values (A/NK = 1.11-1.32) than the samples of Říčany granite (A/NK = 1.20-1.43). They are shifted from the Říčany granite samples toward the line where A/NK = A/CNK (dashed line in the diagram of Shand, 1943, Fig. 5.4), which only means that the rocks from the aplite-pegmatite belt have lower contents of CaO (that was showed on other diagrams already – e.g. O'Connor). The marginal unit of biotite granodiorite has distinctly higher A/NK value than all the other samples (A/NK = 1.98). Another specification provides the diagram of Villaseca et al. (1998) (Fig. 5.4), according to which is the Říčany granite lowly to moderately peraluminous and the rocks from the aplite-pegmatite belt are felsic peraluminous (with a further linear evolutional trend), which means that they are very evolved.

According to the MALI and SiO_2 content in wt. % of the samples, the majority of rocks is alkali-calcic (Frost et al., 2001), the samples from the aplite-pegmatite belt only shift relatively to the Říčany granite samples toward bigger SiO_2 contents along the alkali-calcic field, and the two rock suites form two distinctly separated groups (Fig. 5.4). The Říčany granite samples have MALI = 6.75-8.26 and 69.77-71.99 wt. % SiO_2, whereas the samples from the aplite-pegmatite belt have MALI = 7.50-9.63 (this points again to the lower values of CaO in the aplites and pegmatites) and 73.64-77.40 wt. % SiO_2. The aplites from the aplite-

pegmatite belt are near the border between alkali-calcic and calc-alkalic fields, stretching also in the calc-alkalic field. Only some pegmatites reach the alkali field, and the marginal unit of biotite granodiorite in the aplite-pegmatite belt plots in the calcic field (MALI = 2.07; 67.99 wt. % SiO_2).

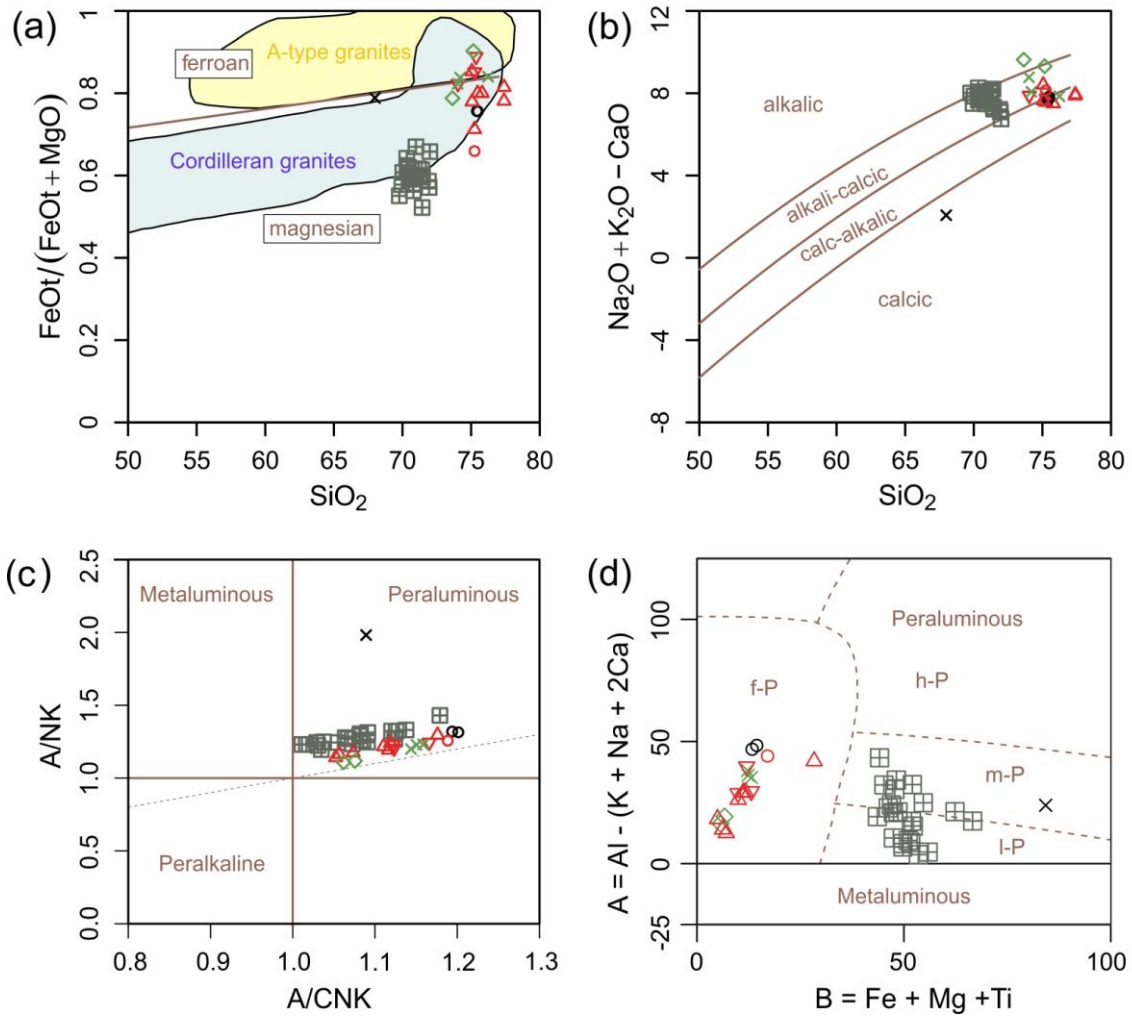

Fig. 5.4 Position of the analysed samples in the classification diagrams for granitic rocks. (a) Classification diagram discriminating ferroan and magnesian rocks according to Fe^* value (weight proportion of FeO^{tot} / (FeO^{tot} + MgO)) (Frost et al., 2001). Usual positions of A-type granites and Cordilleran granites indicated. (b) Classification diagram discriminating alkalic, alkali-calcic, calc-alkalic and calcic rocks according to modified alkali-lime index (MALI) (Na_2O + K_2O – CaO in wt. %) (Frost et al., 2001). (c) Classification diagram discriminating peraluminous, metaluminous and peralkaline rocks according to A/NK value (molecular Al_2O_3 / (Na_2O + K_2O)) and A/CNK value (molecular Al_2O_3 / (CaO + Na_2O + K_2O)) (Shand, 1943). The dashed line is the line where A/NK = A/CNK. (d) A-B plot of Villaseca et al., 1998 (based on millications: 1000 gram-atoms per 100 grams). l-P – lowly peraluminous, m-P moderately peraluminous, h-P – highly peraluminous, f-P – felsic peraluminous.

According to the Fe^* value and the diagram of Frost et al. (2001) (Fig. 5.4), the Říčany granite samples are clearly magnesian (Fe^* = 0.38-0.53), whereas the samples from the aplite-pegmatite belt (including the marginal unit of biotite granodiorite) plot near the border between ferroan and magnesian fields (Fe^* = 0.52-0.84). The two rock suites form again two distinctly separated groups.

In the SiO_2 vs. K_2O classification diagram of Peccerillo & Taylor (1976) (Fig. 5.2), the increasing SiO_2 concentrations are used as an index of fractionation, and they are very high in our samples. The Říčany granite samples stretch from shoshonite to high-K calc-alkaline series (4.53-5.78 wt. % K_2O) and the samples from the aplite-pegmatite belt form a separated, more dispersed group, with the majority of samples in the high-K calc-alkaline field and generally lower contents of K_2O (3.55-5.39 wt. % K_2O). The pegmatite samples form an exception, they have the highest contents of K_2O (5.77-6.12 wt. % K_2O) and belong to shoshonite series. The biotite granodiorite sample belongs to calc-alkaline series.

In summary, our rocks are peraluminous, alkali-calcic or calc-alcalic with high K_2O contents, which are slightly decreasing from the Říčany granite toward the aplites from aplite-pegmatite belt. The marginal granodiorite is an exception, which is calcic with very low K_2O contents (~2.6 wt. % K_2O). Pegmatites from the aplite-pegmatite belt tend to be alkalic with very high K_2O contents. Rocks from the aplite-pegmatite belt have higher Fe^* values and SiO_2 contents relatively to the Říčany granite and the two rock suites form two separated groups.

5.2.4 Trace elements

We used spidergrams of selected element contents normalized to the bulk upper continental crust (UCC) composition according to Rudnick & Gao (2003) with ordering according to Nesbitt et al. (2009) in order to study composition anomalies in our rocks. When we compare only the bulk continental crust composition with the composition of studied rocks, all the studied rocks tend to be enriched in Cs, Rb, Li, Be, U, Th, Ta, Tl, Pb, Sn and slightly in K, Nb, Ga, Ge; and depleted in Ba, Sr, LREE, Sc, Hf, Zr, Ti, V, Mo, Cr, Co, Ni, P and slightly in HREE and Y relatively to the UCC (Fig. 5.5).

The rocks from the aplite-pegmatite belt tend to be relatively more depleted in the majority of elements than the Říčany granite (Fig. 5.5; Fig. 6.2). Pegmatite pockets are the relatively most depleted in the majority of elements. The biotite granodiorite is on the contrary relatively the most enriched in the majority of elements. The most distinct difference between the Říčany granite and the rocks from the aplite-pegmatite belt is in Ba (~8-80x depleted in the aplite-pegmatite belt and ~0.5x enriched in the Říčany granite) and Sr (~10-80x depleted in the aplite-pegmatite belt and around 0 in the Říčany granite).

5.2.5 REE distribution

The sum of REE is distinctly higher in the Říčany granite than in the rocks from the aplite-pegmatite belt (ΣREE = 2.2-79.5 ppm with the majority of values around 25 ppm in the aplite-pegmatite belt and ΣREE = 112.0-166.7 ppm with the majority of values around 135

ppm in the Říčany granite). When we compare the rare earth element (REE) contents in studied rocks with the REE contents in chondrite (according to McDonough and Sun, 1995) and plot that in a chondrite-normalized spidergram, the most striking feature in the diagram is the big negative Eu-anomaly in the rocks from the aplite-pegmatite belt ($Eu/Eu^* = 0.04$-0.39 in the rocks from the aplite-pegmatite belt except pegmatites), which is much smaller in the Říčany granite ($Eu/Eu^* = 0.40$-0.73 in the Říčany granite), marginal biotite granodiorite ($Eu/Eu^* = 0.75$ in the granodiorite) and is small or missing in the pegmatites ($Eu/Eu^* = 0.47$-1.29 in the pegmatites) (but this is caused probably by the very low value of the REE contents in the pegmatite samples – Eu content can not be much lower any more) (Fig. 5.6 and the variation diagram of Eu/Eu^* vs. SiO_2 in Fig. 5.2).

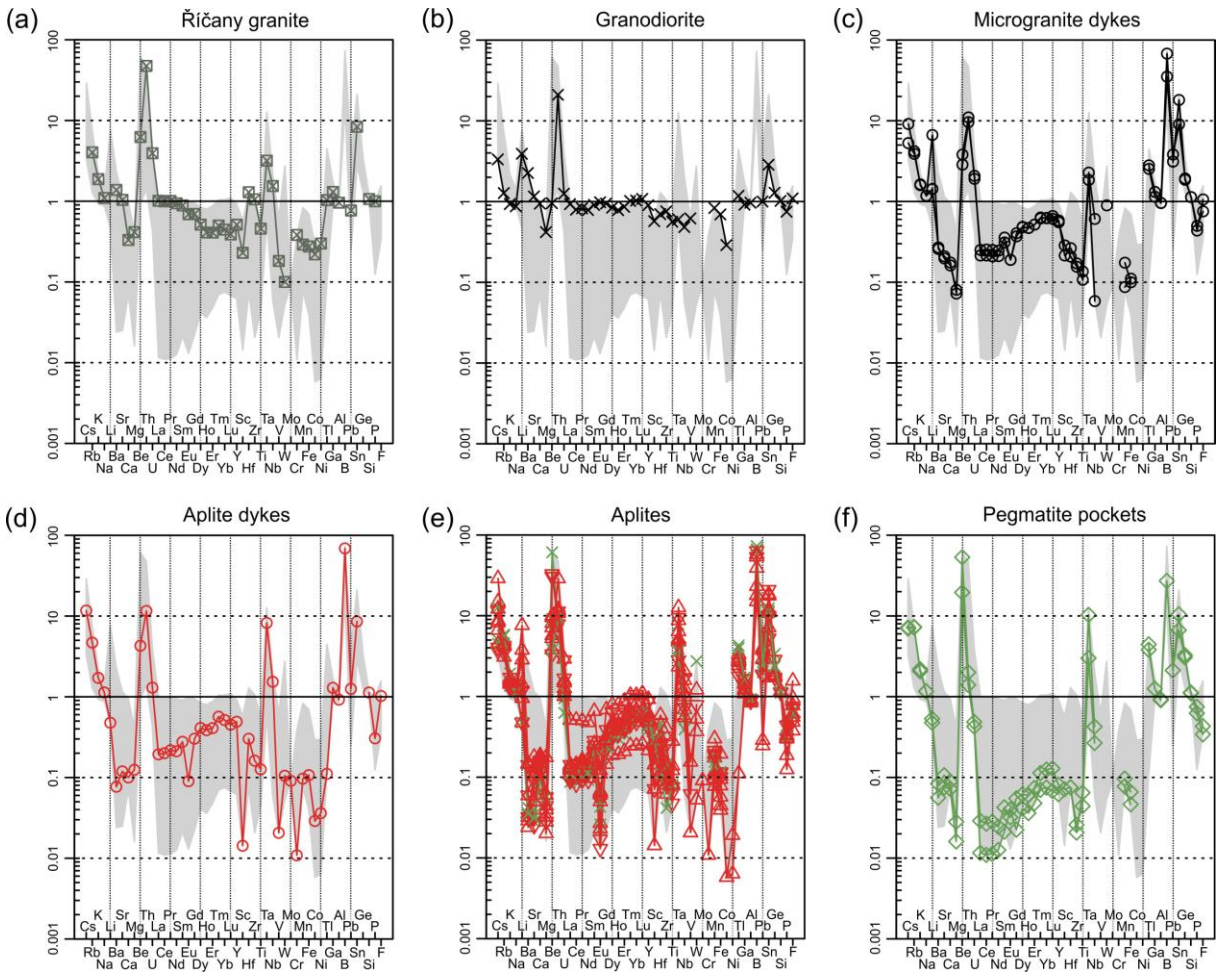

Fig. 5.5 Spidergrams of selected element concentrations in the analysed samples normalized to the bulk upper continental crust composition (UCC) (Rudnick & Gao, 2003) with coherent ordering (Nesbitt et al., 2009). (a) Říčany granite samples (b) biotite granodiorite sample (c) microgranite dykes samples (d) aplite dyke sample (e) massive aplites, layered aplites and megacryst zones (with aplites around them) samples (f) pegmatite pockets samples. The grey area is the total range of all the analysed samples.

All the rare earth elements are enriched relatively to the chondrite concentrations in the Říčany granite (~5-100x) as well as in the rocks from the aplite-pegmatite belt (~3-50x) with

the exception of Eu (up to ~9x depleted), only pegmatites are depleted (up to ~7x) in more rare earth elements than only in Eu. In the Říčany granite, LREE (light rare earth elements) are more enriched than HREE (heavy rare earth elements) with a smooth trend from La, which is the most enriched, to Lu, which is the least enriched (La_N/Yb_N = 15.7-31.2 in the Říčany granite). There is a similar parallel trend in the rocks from the aplite-pegmatite belt and pegmatites from La to Sm, but from Gd to Lu the enrichment does not further descend and stays on the same value or even increase in the case of pegmatites (La_N/Yb_N = 1.4-5.1 in the rocks from the aplite-pegmatite belt) (diagram of La/Yb vs. SiO_2 in Fig. 5.2). The consequence is, that values of enrichment in the Říčany granite and in the rocks from the aplite-pegmatite belt (except pegmatites) approach and are similar for the HREE. The unit of marginal biotite granodiorite resembles the Říčany granite, but adapts the stagnating trend of the rocks from the aplite-pegmatite belt for HREE at the end.

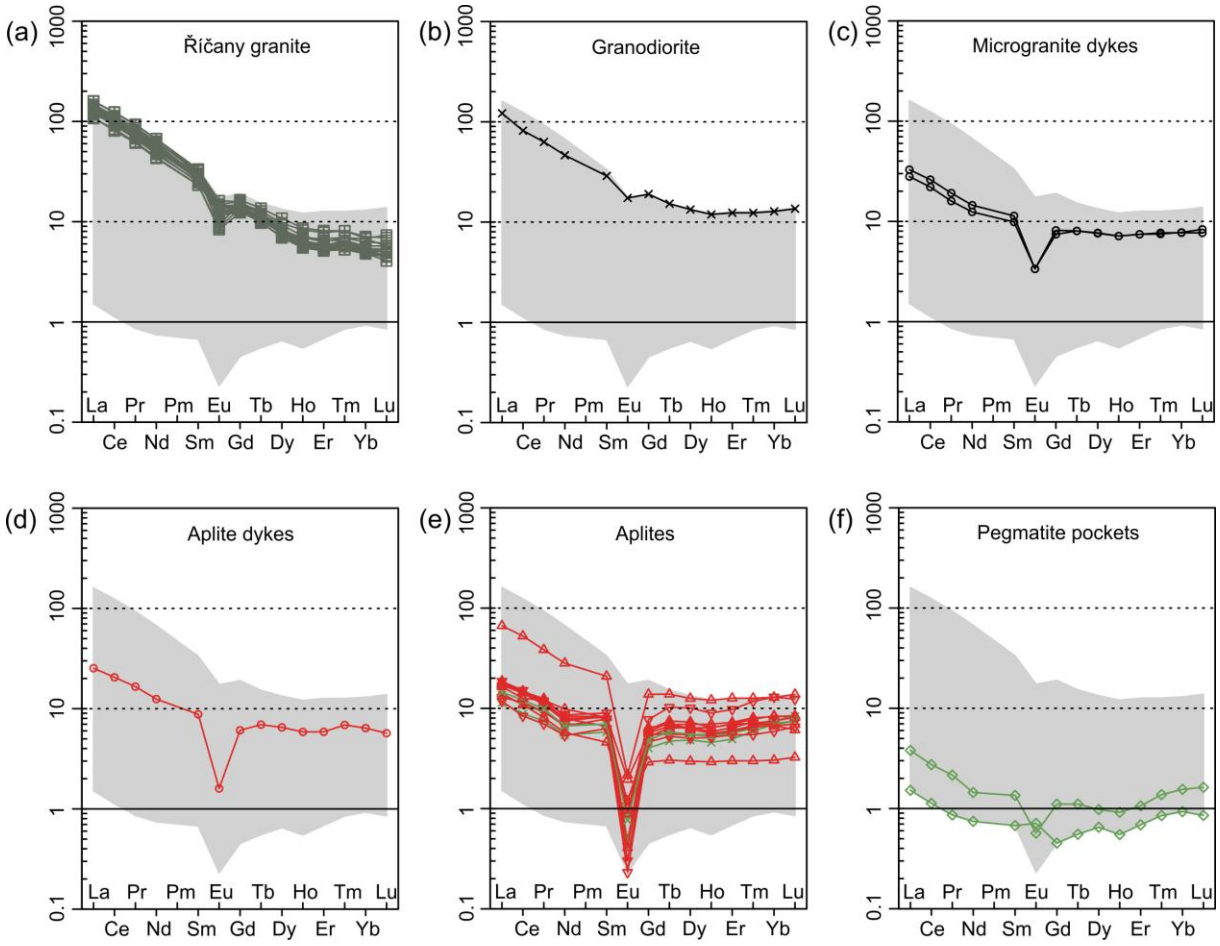

Fig. 5.6 Spidergrams of REE (rare earth elements) concentrations in the analysed samples normalized to the chondrite composition (McDonough and Sun, 1995). (a) Říčany granite samples; (b) biotite granodiorite sample; (c) microgranite dykes samples; (d) aplite dyke sample; (e) massive aplites, layered aplites and megacryst zones (with aplites around them) samples; (f) pegmatite pockets samples. The grey area is the total range of all the analysed samples.

6 Interpretation and discussion

6.1 Origin of granite-aplite-pegmatite suite

We address the origin of the granite-aplite-pegmatite melts by using whole-rock geochemical data, mineral chemistry, textural evolution, and geothermometry. The Říčany granite pluton melt is a peraluminous, high-K calc-alkaline to shoshonitic, magnesian and alkali-calcic (MALI = 6.8-8.3) granite, whose composition is characteristic of the group of post-tectonic Caledonian granitoids (Frost et al., 2001) or late- to post-orogenic granitoids (Batchelor & Bowden, 1985; Maniar & Piccoli, 1989; Trubač, 2008) (Fig. 6.1). Its lithophile and high-field strength concetrations are consistent with the post- or syn-collision geodynamic setting (Pearce et al., 1984; Fig. 6.1). This is in agreement with its peraluminous nature and the presence of biotite as the only mafic phase.

Its transitional A-type vs. fractionated I/S-type signature (highly fractionated I- or S-type granites can overlap the signature of A-type granites) (Whalen et al., 1987; Fig. 6.1) is a reflection of a strong negative correlation between Zr + Ce + Y and Rb/Ba (Fig. 6.1), which is likely a product of fractionation of accessory phases and feldspars. The Říčany granite has thus some features of A- and S-type granites (Jakeš, 1977; Janoušek, 1991; Trubač, 2008). The peraluminious nature and the Mg enrichment of the Říčany granite are some of the untypical features of the A-type granites. The small volume of this hypothetical A-type granite melt, in contrast, to other types of granitoids (I- and S-types) in the Central Bohemian Plutonic Complex indirectly supports the hypothesis that the Říčany granite is a fractionated I/S-type granite with an A-type signature. The radiogenic isotopic signature implies that the source-rock were probably metasediments of the Moldanubian unit mixed with various other units (Janoušek et al., 1995b). The degree of fractionation increases from the center to the margin of the pluton, which indicates a reversed chemical zoning, produced during an emplacement along a steep-sided conduit from an underlying, stratified magma chamber to a hypothetical volcanic feeder at the surface (Janoušek et al., 1997; Trubač, 2008). The two varieties of the Říčany granite may represent two closely-related magma batches.

The aplite-pegmatite belt was emplaced along the roof of the Říčany pluton (as revealed by field relationships, macroscopic and magnetic magmatic fabric). Decreasing normative An/Ab ratio, increasing values of SiO2, MALI, Fe^* (weight proportion of FeO_{tot} / (FeO_{tot} + MgO), Rb-Sr ratio, pronounced negative Eu anomaly, point to a more evolved or fractionated nature of the aplite-pegmatite suite. The genetic connection between the Říčany granite and the aplite-pegmatite belt is indicated by their similar although discontinuous geochemical signatures (for example the units have similar ASI value – it is representative mainly of the source composition and nature of melting process; or indicative is only the fact, that the Říčany granite is relatively rich in Sn, W, B, and Be, Němec, 1978, which are extremely enriched in the aplite-pegmatite belt) (e.g. Fig. 5.2; Fig. 5.3; Fig. 5.4; Fig. 5.5; Fig. 6.2). Furthermore, the differentiation path from the Říčany granite to the aplite and pegmatites

follows a common alkali-lime trends in the MALI *vs.* SiO_2 diagram (Fig. 5.4) (Frost et al., 2001).

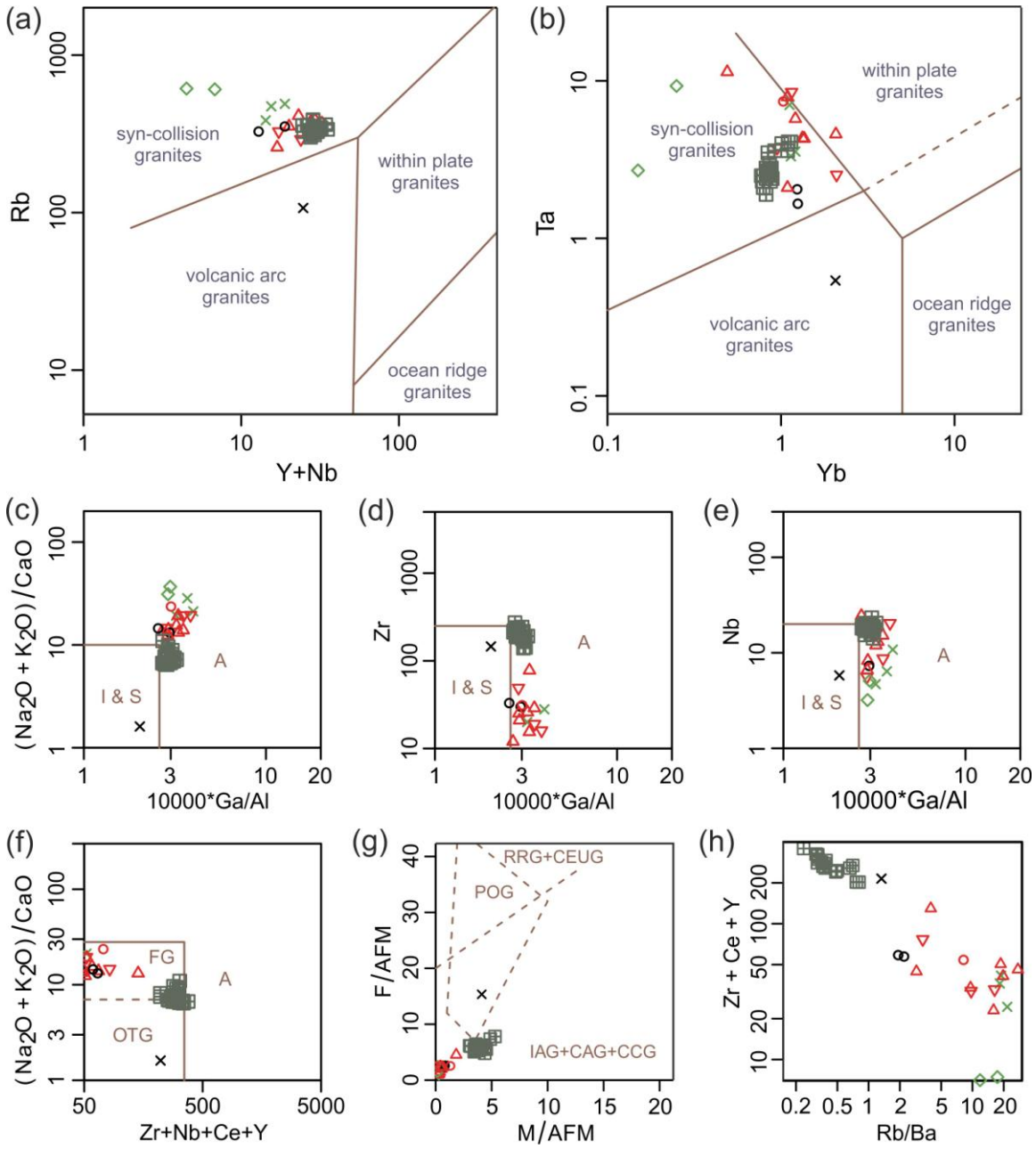

Fig. 6.1 Geotectonic discimination diagrams for silicic rocks: (a) Rb vs. Y + Nb diagram (Pearce et al., 1984); (b) Ta vs. Yb diagram (Pearce et al., 1984); (c) $(Na_2O + K_2O)/CaO$ vs. 1000*Ga/Al diagram. Abbreviations: A – A-type granites, I & S – I- and S-type granites (Whalen et al., 1987); (d) Zr vs. 1000*Ga/Al diagram (Whalen et al., 1987); (e) Nb vs. 1000*Ga/Al diagram (Whalen et al., 1987); (f) $(Na_2O + K_2O)/CaO$ vs. Zr + Nb + Ce + Y diagram. Abbreviations: A – A-type granites, OTG – ordinary I- and S-type granites, FG – fractionated I- and S-type granites (Whalen et al., 1987); (g) F/AFM vs. M/AFM diagram where F/AFM = $(100*FeO_{tot}/(Al_2O_3 + Na_2O + K_2O + FeO_{tot} + MgO))$ and M/AFM = $(100*MgO/(Al_2O_3 + Na_2O + K_2O + FeO_{tot} + MgO))$. Abbreviations: RRG – rift-related granitoids, CEUG - continental epeirogenic uplift granitoids, IAG – island arc granitoids, CAG

– continental arc granitoids, CCG – continental collision granitoids, POG – post-orogenic granitoids (Maniar and Piccoli, 1989); (h) Zr + Ce + Y vs. Rb/Ba diagram (Whalen et al., 1987).

The geochemical discontinuity between the Říčany granite and the aplite-pegmatite suite, apparent from a number of variation diagrams (Fig. 5.2; Fig. 5.3), suggests that the aplite-pegmatite series represents a separate magma batch of a magma from (large) parental magma chamber and it has no direct (continuous) transition to the Říčany granite at the present exposure level. It may have formed by melt percolation through the semi-solidified crystal mush of the Říčany granite and its differentiation occurred by a mechanism possibly analogous to solidification front instability (Marsh, 1996, 2002).

The more compatible major elements (e.g., Ca, Fe, Mg, Ti) are slightly depleted in the aplite-pegmatite suite while more incompatible ones (e.g., Si, Na, B and K) are enriched (Fig. 6.2). The solidified crystal mush would thus appear to be enriched in anorthite-bearing plagioclase, mafic silicates, rutile and apatite. Most of the H2O and B content in the melt are probably not preserved during crystallization but lost to hydrothermal fluids.

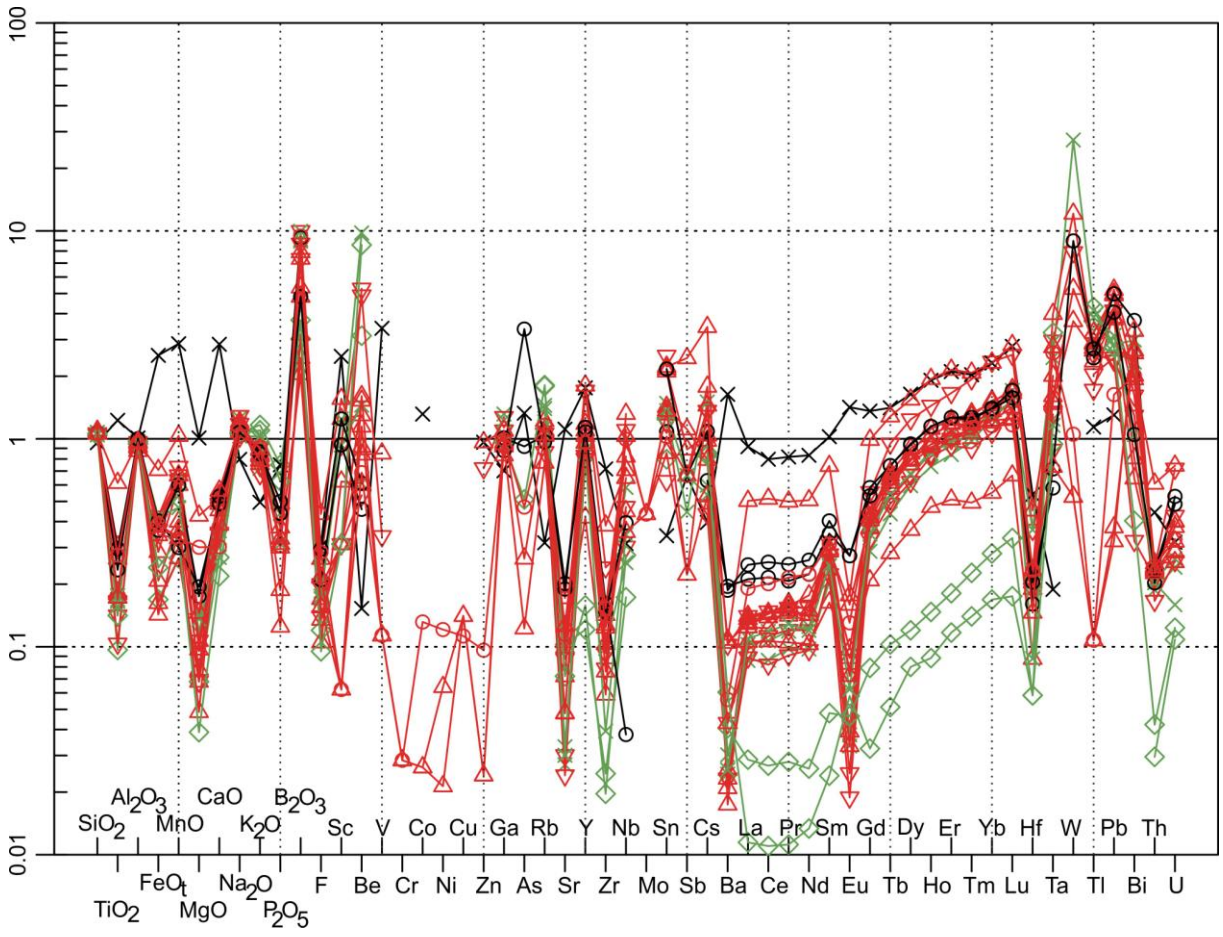

Fig. 6.2 Trace-element spidergraph illustrating the aplites and pegmatites normalized to the average Říčany granite (Trubač, 2008).

The aplites and pegmatites are strongly enriched in Sn, W, Ta, Pb, B and Be and depleted in Sr and Ba (and most of the studied trace elements) when compared to the average

Říčany granite (Fig. 6.2). Ratios of incompatible-compatible element pairs such as Rb/Sr increase from 1.02 in the average Říčany granite to 5.19-47.3 in aplites and pegmatites. The aplites and pegmatites show greater fractionation of LREE as well as more pronounced negative Eu anomaly (Fig. 5.6). Flat REE patterns with pronounced negative Eu anomalies like in our case are generally typical for fractionated granitic melts coexisting with a fluid phase (Raith et al., 2004). This is especially true in the aplite-pegmatite belt case – La_N/Yb_N = 1.4-5.1 in the aplites and pegmatites, whereas in the Říčany granite La_N/Yb_N = 15.7-31.2.

Although there is an indication in the whole-rock geochemical patterns for a further evolutionary trend between the analysed rock-samples from the aplite-pegmatite belt, only the pegmatite samples differ systematically, mainly in the Eu anomaly (it is smaller again in them), K, P and Rb contents (bigger in them) and MALI value (they have the biggest). The pegmatites are also depleted the most in the majority of trace elements. The marginal biotite granodiorite has a completely different geochemical signature than both the Říčany granite and the rocks from the aplite-pegmatite belt, therefore it presents probably some other, extraneous melt.

Lowering proportion of anorthite component in plagioclase, lowering of *mg#* (molar Mg/[Fe+Mg]) in tourmaline (Fig. 4.10), muscovite or biotite (when present), increasing of *mn#* (molar Mn/[Fe+Mn]) in garnet (Fig. 4.9), differing compositions of accessory minerals (e.g. bigger content of volatiles), or occurrence of minerals like topaz and beryl are the main factors indicating further fractionation within the aplite-pegmatite belt. Massive aplites together with megacryst zones are the less evolved rock types within the aplite-pegmatite belt. They are followed by layered aplites, pegmatite layers, and pegmatite dykes, which are the most evolved melts within the aplite-pegmatite belt. Pegmatite pockets, microgranite and aplite dykes have usually big dispersion of values or bimodal or trimodal distributions, which suggests that they crystallized successively during approximately first half of the aplite-pegmatite belt solidification time.

6.2 Thermometry of magmatic crystallization

The liquidus temperature of the aplite-pegmatite magma can be evaluated by using zircon, monazite or apatite saturation thermometry (calculated with the help of Saturnin script of Janoušek, 2006). The equation of Watson & Harrison (1983) was used for estimating the zircon saturation temperature:

$$T(K) = \frac{12900}{\ln\left(\frac{497644}{Zr}\right) + 3.8 + 0.85 * (M - 1)}, \qquad (6\text{-}1)$$

where T is absolute temperature (K), Zr represents the observed Zr concentration in the whole rock (ppm), and M is a cation ratio representing the composition of the melt:

$$M = \frac{Na + K + 2Ca}{Al * Si}. \tag{6-2}$$

The temperature estatimes based on zircon saturation are more sensitive to accuracy of Zr determination at temperatures below ~700 °C and *M* values lower than ~1.5. Inheritance or presence of cumulus zircons would increase the estimated temperature (Miller et al., 2003).

The equation of Montel (1993) was used for monazite saturation thermometry:

$$T(K) = \frac{13318}{9.5 + 2.34D + 0.3879\sqrt{H_2O} - \ln(REE_t)}, \tag{6-3}$$

where *T* is absolute temperature (K), H_2O is the assumed water content in the magma, *D* is a cation ratio representing the composition of the melt:

$$D = 100\frac{Na + K + Li + 2Ca}{Al}\frac{1}{Al + Si}, \tag{6-4}$$

$REE_t = \sum(REE_i/at.weight_i)/X_{mz}$ for La, Ce, Pr, Nd, Sm, and Gd concentrations in the whole rock (ppm), and X_{mz} is a mole fraction of the REE in monazite. Monazite saturation thermometry is sensitive to the assumed water content in the magma (which is uncertain) and determination of REE.

We used the equation of Harrison & Watson (1984) in combination with the relationship by Pichavant et al. (1992) for calculating the apatite saturation temperature:

$$P_2O_5 = \frac{42}{\exp\left(\frac{8400 + 26400 * (SiO_2 - 0.5)}{T}\right) - 3.1 - 12.4 * (SiO_2 - 0.5)} + \\ + (A/CNK - 1)\exp\left(\frac{-5900}{T} - 3.22 * SiO_2 + 9.31\right), \tag{6-5}$$

where P_2O_5 represents saturation level of P_2O_5 in the melt, *T* is absolute temperature (K), SiO_2 is weight fraction of silica in the melt (wt. % SiO_2/100), and *A/CNK* is the molecular $Al_2O_3/(CaO + Na_2O + K_2O)$.

The results are listed in Tab 6.1. The convergence of monazite and zircon thermometries is shown in Fig. 6.3. Crystallization temperatures of the Říčany granite vary from 782 to 825 °C (average is near 800 °C) according to the zircon saturation thermometry. The monazite saturation temperatures are similar, about 30 °C lower, from 766 to 800 °C and there is a good correspondence between two approaches. The apatite saturation is considered to be unreliable due to a very large dispersion of values, which is related to scattered P_2O_5 concentrations, probably due to local accumulation of phosphate minerals.

The biotite granodiorite marginal facies yields very consistent zircon and monazite saturation temperatures, 781 and 774 °C, respectively. Aplite and microgranite dykes yield temperatures 670-673 °C according to the zircon saturation thermometry, and 687-704 °C according to the monazite saturation thermometry. Massive aplites zircon and monazite saturation temperatures are also consistent, 604-664 °C and 626-655 °C, respectively, but there is one anomalous result for a biotite aplite (zircon and monazite saturation temperatures 740 and 752 °C, respectively). Zircon and monazite saturation temperatures of layered aplites are similar to massive aplites temperatures (627-701 °C and 627-659 °C, respectively). Megacryst zones zircon and monazite saturation temperatures have a similar range like massive and layered aplites temperatures, but can be occasionally lower (584-663 °C and 632-646 °C, respectively). Pegmatite pockets zircon and monazite saturation temperatures are the lowest ones in the aplite-pegmatite belt (543-553 °C and 509-553 °C, respectively). The majority of apatite saturation temperatures of the rocks from the aplite-pegmatite belt falls only between 450-550 °C (total range 443-664 °C with the highest temperatures for pegmatite pockets and 590 °C for the biotite granodiorite).

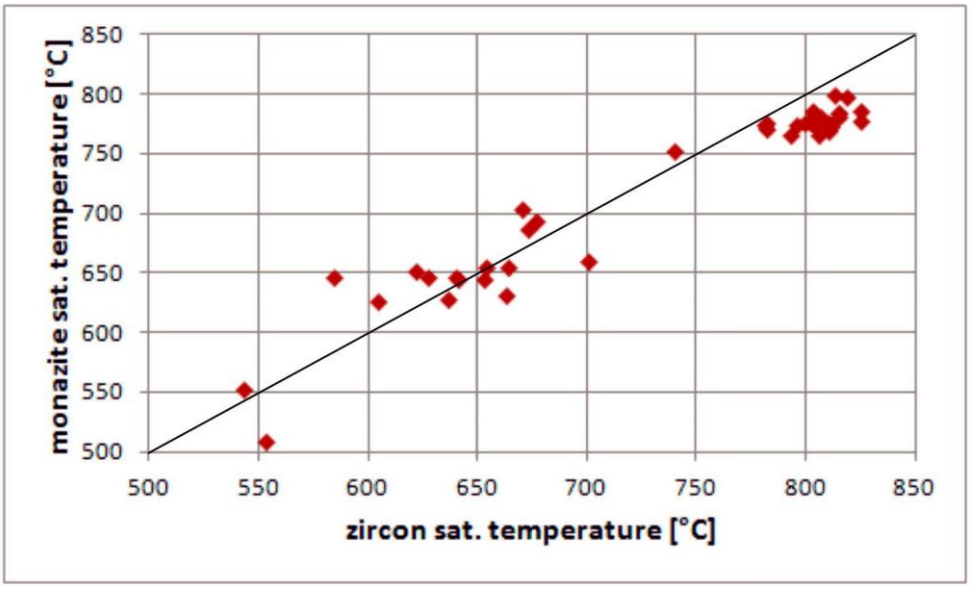

Fig. 6.3 Results of the zircon and monazite saturation thermometries and their convergence.

Apatite saturation thermometry is apparently not well suited for peraluminous silicic melts, because the temperature estimate is extremely sensitive to rather small variations in P_2O_5, hence any mechanical and chemical interactions involving phosphates. In addition, feldspars can incorporate large amounts of phosphorus *via* the berlinite substitution (e.g. London et al., 1990). Therefore, the results of the zircon and monazite saturation thermometry are considered superior as also supported by their close convergence (Fig. 6.3). Zircon and monazite grains do not have inheritance or are not cumulus in our rocks, and should have been saturated during the entire solidification time of the aplite-pegmatite belt (indicated for example by linear trend in the diagram Zr vs. Ti – Fig. 5.3). The results of zircon and monazite saturation thermometries confirm the approximate temperature estimates according

to the Ti-content in muscovite (Auzanneau et al., 2010), which are up to ~700 °C (in average ~650 °C).

Tab. 6.1 Results of the saturation thermometry.

Sample	Rock group	T zircon	T monazite	T apatite
DT27B	MG	670.1	703.9	473.6
DT30	MG	677.0	693.3	483.5
TR5	AD	672.8	687.1	443.5
OAP1	MA	663.9	655.5	515.6
JT72	MA	652.9	644.8	479.1
DT7B/1	MA	604.3	625.8	518.4
DT7B/2	MA	739.8	752.3	451.1
DT14	MA	639.9	646.6	545.7
TR1	MA	654.0	655.2	493.0
TR2	MA	622.1	651.5	485.3
OAP2	LA	700.8	659.3	514.8
TD1	LA	636.7	627.5	519.0
TJ7B	LA	627.4	647.1	488.2
TJ13A/1	MZ	641.0	644.3	501.2
TJ13A/2	MZ	584.1	645.7	465.9
DT20	MZ	663.2	631.6	489.3
OAP3	PP	553.0	509.2	663.8
PEG	PP	543.1	552.7	618.1
OAP6	GR	781.4	774.3	589.6
RI1	G	825.0	786.0	665.7
RI2	G	815.2	780.8	894.9
RI3	G	815.4	783.5	845.0
RI7	G	825.4	777.7	883.9
RI8	G	806.0	765.6	800.9
RI9	G	810.1	772.7	795.0
RI10	G	806.4	781.6	553.8
RI11	G	802.7	785.6	634.0
RI12	G	813.0	799.3	541.8
RI13	G	799.5	776.4	670.7
RI14	G	803.7	774.0	719.9
RI15	G	818.8	797.3	618.4
RI16	G	815.2	783.4	643.1
RI17	G	811.5	772.1	661.4
RI18	G	796.0	773.7	638.6
RI19	G	792.8	766.4	683.1
RI21	G	781.8	775.8	564.8
RI22	G	781.7	770.8	582.0
TR4	G	810.6	775.0	776.1
TR16	G	810.1	769.1	767.6
TR6	G	803.5	780.8	705.3
TR7	G	801.7	775.5	666.6

All temperatures are in °C. T zircon = temperature according to zircon saturation thermometry; T monazite = temperature according to monazite saturation thermometry; T apatite = temperature according to apatite saturation thermometry; G – Říčany granite; GR – granodiorite; MG – microgranite dykes; AD – aplite dykes; MA – massive aplites; LA – layered aplites; MZ – megacryst zones; PP – pegmatite pockets.

The results show that the aplites and pegmatites crystallized at significantly lower temperatures than the Říčany granite. This is in agreement with crystallization temperatures postulated for pegmatites (e.g. London et al., 2012). When the aplite-pegmatite belt formed a very thin, possibly sheet-like igneous body, such a unit would have crystallized in days to

years (e.g. Morgan and London, 1999; Webber et al., 1999). The undercooled conditions of crystallization are furthermore indicated by various crystallization textures.

6.3 Origin of modal and textural variations

6.3.1 Theoretical considerations

Various types of compositional (modal) or textural layering are observed in igneous rocks and these result from flow processes (subject to appropriate rheology including viscosity of the magma), density currents, compaction of crystal mush with an expelled melt and/or crystal settling (Barbey, 2009). These mechanisms frequently cause a megascopic or pluton-scale layering, which can result from more different magma pulses (in the case of granitic suites often connected with mafic batches of magma or mafic enclaves), their mingling, magmatic deformation etc. In the case of pegmatite crystallization, an alternative model has been proposed based on static crystallization under the conditions of limited difussion, which assist the formation of chemically distinct boundary layers in the melt. However, there are some indications like sharply defined dykes of residual melt, rare cross-bedding and other erosional structures (Fig. 2.9) that some multiple injection and flow processes occurred.

The static layering mechanisms can be linked to the variation of intensive parameters (for example repeated abrupt pressure decreases due to release of volatiles termed swinging eutectic; Jahns, 1982), or simply to the properties of the melt and conditions of emplacement. A popular theory is a diffusion-controlled oscillatory nucleation in an evolved boundary layer (e.g. Webber et al., 1997; London, 2005, 2008, 2009).

The theory of diffusion-controlled oscillatory nucleation is applied to layered aplites (line rocks) commonly found in the footwall portions of composite pegmatite-aplite dykes. They are interpreted to have crystallized from a highly viscous and highly undercooled melt, which promotes localized nucleation on a plane parallel to the chilled dyke margin and rapid crystallization in a dense solidification front (parallel to the dyke margin; e.g. London, 2009). The high viscosity of the melt inhibits the diffusion of components but the chemical potential to drive crystallization (thus the rate of crystallization) remains high. The components which are not incorporated into the growing minerals (such as feldspars and quartz) do not have sufficient time to diffuse away from the advancing crystallization front and continue to build up ahead of the front, thus forming a chemically distinct boundary layer. The compositional departure causes the current minerals to become undersaturated, whereas other ones become saturated and may crystallize until the accumulated components are consumed. The process repeats until any condition is changed. To apply this layering mechanism to interpretation of aplite and pegmatites in the Říčany pluton, several conditions must be fulfilled: (1) the melt must be undercooled so that the driving force for crystallization is high; (2) nucleation must be highly localized so that the solidification proceeds in a dense crystallization front; (3) the melt must be highly viscous or the diffusion of relevant components must be slow or inhibited

in some way; (4) all the components needed for the mineral forming bands must be present in the melt and the conditions needed for the nucleation and growth of the mineral must be fulfilled; (5) the diffusivities of the components needed must be in the melt comparable or slower than the growth rates of the main matrix minerals.

6.3.2 Undercooling and crystal nucleation

Undercooling in a steadily cooling magma body can be promoted by a nucleation delay, rapid pressure decrease or rapid cooling of the melt. Assuming that the Říčany pluton has been emplaced near ~2 kbar (Kachlík, 1992; Eliška Žáčková personal communication, 2013), probably at conditions close to water-saturated (~6 wt. % H_2O at 2 kbar; Zhang et al., 2007) and with significant amounts of boron (exceeding 2 wt. % B_2O_3 in the melt; Wolf and London, 1997). These volatiles act to decrease the liquidus temperature, which is expected to lie at ~700 °C but becomes lowered to ~660 °C (Pichavant, 1987). The solidus temperatures of H_2O-saturated haplogranite melt are at 680-720 °C (Tuttle and Bowen, 1958) but decrease in the presence of boron to 630-660 °C (Chorlton and Martin, 1978). The results of the zircon and monazite geothermometry are well in line with the fundamental assumption of these approaches, that is, the cessation of the crystal-melt separation. From that point on, the melt (magma) must have crystallized in a chemically closed system. Many textures found, like skeletal and elongated crystals, graphic intergrowths, comb and unidirectional solidification textures, provide evidence for undercooling imposed on the estimated equilibrium temperatures (e.g. Fenn, 1986; Lofgren, 1975).

The highly localized nucleation along the margins of the body and formation of a dense solidification front are the expected results of undercooling of the body (London, 2009). If the nucleation were not highly localized on the tip of the crystallization front and this diffusion-controlled nucleation would operate, the boundary layer would form around scattered early crystals in the solidification front and an orbicular texture would result. Therefore, the layering itself (except for the unidirectional solidification textures) is the evidence for a dense solidification front and a localized formation of crystal nuclei.

A crucial condition for the diffusion-controlled oscillatory nucleation to occur is the sufficiently rapid growth rate of the solidification front and the sufficiently slow diffusion of the components in the melt. Considering the undercooled state of the melt, the growth rates in aplite-pegmatite melts could have been very high, on the order of 10^{-7}-10^{-8} m s^{-1} (e.g. Swanson, 1977; Webber et al., 1999). For the slowest permissible rates (~10^{-12} m s^{-1}), they would be at most approximately the same as the diffusion coefficient of boron in haplogranitic melt (~10^{-12} m^2 s^{-1}; London, 2009). This implies that the evolved boundary layer form because the diffusion of components in the melt is always slower than the growth rate of the solidification front.

The growth rates probably did not change as much as the nucleation densities, which must have changed rapidly by several orders of magnitude. Some abrupt changes in

nucleation density can be caused by abrupt changes in undercooling imposed by sudden exsolution of volatiles. Release of boron-rich fluids is demonstrated by hydrothermal quartz-tourmaline veins near Tehov and elsewhere in the vicinity. It is probable that the system underwent second boiling due to the concentration of water in the residual melt after some period of early crystallization. The majority of tourmalines disseminated in massive and layered aplites has two sharp pleochroic zones (darker rims and lighter cores), which differ chemically as well, possibly reflecting the sudden change in oxygen fugacity due to hydrogen partitioning into the fluid phase.

6.3.3 Melt viscosity and diffusion

As discussed previously, the viscosity of granitic melts is generally very high and it is further increased when the melt is undercooled but, on the other hand, it is significantly reduced by the presence of H_2O or other volatiles in the melt. A water-rich fluid probably saturated and escaped from our melt during the solidification, taking significant amounts of boron from the melt, because boron has a high affinity toward a water-rich fluid (e.g. Thomas et al., 2003), therefore the initial H_2O and boron contents of the melt were probably very high, allowing the viscosity to be low during the ascent and emplacement of the melt (e.g. Dingwell et al., 1992; Veksler and Thomas, 2002). If we assume H_2O-saturated conditions at the pressure of ~2 kbar and lower, the viscosity could have been still very high (~10^5-10^9 Pa.s; Hess and Dingwell, 1996; Nabelek et al. 2010). Therefore the chemical diffusion should be efficiently inhibited.

6.3.4 Tourmaline modal layering

Crystallization of tourmaline from evolved granitic melt requires sufficient concentrations of B, Fe or Mg, and Al under appropriate pressure and temperature conditions. Since temperature and pressure are not the critical factors governing tourmaline stability (e.g. Benard et al., 1985; Ertl et al., 2010). Low activities of ferromagnesian components tend to severely limit the amount of crystallized tourmaline (e.g., London and Manning, 1995) but it continues to form in small quantities even when the ferromagnesian content of the melt is exceedingly low provided that the activities of B and Al are sufficiently high (Wolf and London, 1997). The aplites and pegmatites are strongly peraluminous (ASI = 1.43-1.68) (minimum ASI = 1.2), and the strong predominance of tourmaline over biotite throughout the aplite-pegmatite suite documents sufficient enrichment in boron because tourmaline and biotite tend to show an antipathetic trend in granitic systems (Pesquera et al., 2013; Wolf and London, 1997). However, the B_2O_3 content in the bulk melt could be very low because only its abundance in the boundary layer is decisive for the crystallization process. This also applies to Fe and Mg contents, which are generally low in the bulk rock but could have been concentrated in the boundary melt layer. The same scenario is likely to apply to narrow bands of garnet where Mn, Fe and Al were enriched in the boundary layer melt, but the local boron concentrations did not reach the level necessary to exceed the garnet-tourmaline peritectic equilibrium.

6.3.5 Crystal growth and textural variations

The textural variations in our rocks are significant, abrupt and small-scale, and comparable to a situation of melt solidification in a fluid-mediated setting. The giant crystals, known from pegmatites forming thin dykes that cooled rapidly (e.g., Webber et al., 1999; Morgan and London, 1999), are absent here and this documents that the highest growth rates have not been reached. However, our rock-forming processes must have been comparable to pegmatite-forming processes, where volatiles play an important role (evidenced for example by the completely different nature of volcanic rocks, which differ from pegmatites often only in the fact, that they could lose the volatiles easily before crystallization commenced). Volatile- and H_2O-rich compositions are necessary at least for the emplacement of the pegmatitic melts into the dykes (Nabelek et al., 2010).

Several features of the aplites and pegmatites are consistent with the theory of constitutional zone refining, which is usually applied to pegmatites (e.g. London, 1999, 2005, 2008, 2009). This process links build-up of an evolved boundary melt layer ahead of the solidification front in a highly viscous undercooled melt with rapid unidirectional crystallization. Volatile components enriched in a boundary layer (such as H_2O and B; also reffered to as "fluxes") tend to lower the liquidus and solidus temperatures of the system, enhance solubility (miscibility) of water in melt, lower the melt viscosity and inhibit nucleation. By lowering the viscosity of the melt, fluxes enhance the lateral diffusivity of essential structural components in the boundary layer melt, therefore giant crystals can quickly grow without being limited by the pile-up of their excluded components in the direction of their growth, while suppressed nucleation contributes to the effect.

The accumulation of volatile components in the boundary melt layer ahead of the solidification front is probably the reason for increasing crystal size in pegmatites of this study. Tourmaline layering is usually associated with crystal-size variations in various combinations (modally but not texturally banded samples are rare), which means, that boron already exerted some fluxing effect before it reached the concentration high-enough to saturate the melt in tourmaline. The coarser bands usually terminate with a fine-grained tourmaline-rich band. However, not every coarse-grained band is closely associated with a tourmaline-rich band, and tourmaline is very rarely found inside the coarse-grained bands. The very coarse-grained bands must have formed by a high accumulation of boron possibly in combination with H_2O in the boundary layer, yet the tourmaline saturation has not occurred probably due to the low concentration of ferromagnesian components in the melt. The coarser-grained bands associated with tourmaline-rich bands from the both sides could have developed, where the concentration of ferromagnesian components was so high, that the melt saturated in tourmaline early, before boron exerted fluxing effect. Than the melt ran out of the ferromagnesian components until they were concentrated enough again at the end of the coarser-grained band. The cessation of the coarser-grained band growth could be associated also with saturation and escape of a H_2O- and boron-rich fluid or melt (by liquid

immiscibility; Veksler and Thomas, 2002). Some coarse grained bands are associated with cassiterite-rich layers, and this may support the case for local enrichment in melt-incompatible elements.

The texture of the coarse-grained parts of our rocks is not blocky, like in the cores of pegmatites, where the constitutional zone refining is expected to operate, but it shows usually unidirectional solidification textures such as comb layers. The minerals are elongated in the direction perpendicular to the layering, which is the proof of crystallization under undercooled conditions. This phenomenon generally represents the transition between layered aplites and blocky cores of pegmatites in the case of constitutional zone refining. The rates of nucleation and growth are not the same for all phases, and the result are the occasional flaring megacrysts of K-feldspar and rare megacrysts of tourmaline extending and intruding several textural zones.

7 Petrogenetic model

The melt of the aplite-pegmatite belt evolved during the solidification of the Říčany granite (crystallization of the main rock-forming minerals enriched the residual melt in incompatible elements), or it represent another magma-batch from the big magmatic chamber underneath the Říčany pluton, which was probably source of the Říčany granites. If the melt was formed in the semi-solidified crystal mush of the Říčany granite, its differentiation occurred by a mechanism possibly analogous to solidification front instability.

The suite of highly evolved aplites and pegmatites was emplaced along the roof of the Říčany granite pluton probably as a thin and subhorizontal body. The aplite-pegmatite melt must have been volatile-rich and occassionally fluid saturation occurred (possibly due to first boiling) as documented by the occurrences of pegmatite pockets or layers in several textural varieties. The loss of volatiles and rapid cooling both contributed to an increase of melt viscosity. The solidification must have proceeded rapidly, at undercooled conditions, with no convection possible due to the high viscosity of the melt and short time scales of solidification. Crystallization of the body probably began with the formation of massive aplites, whereas the megacryst zones could record fluid exsolution from the melt. Additional loss of H_2O due to the second boiling would have caused additional viscosity increase and sudden change in nucleation and growth rates.

Crystallization continued with the formation of layered aplites where the boundary layers formed periodically due to the high viscosity of the melt, inhibited diffusion of the components, and rapid growth rates. The formation of layered aplites and pegmatite interlayers were probably interrelated and the constitutional refining may have contributed to the extreme element fractionation recorded in mineral chemistry. The progressive change in the melt composition is documented by a decrease in anorthite content of plagioclase, decreasing *mg#* values and increasing *fe#* and *mn#* values in tourmaline, biotite and garnet. as well as appearance of accessory minerals such cassiterite, columbite and tantalite. According to these indicators as well as the whole-rock geochemistry, pegmatite dykes represent the most evolved fractions of melt, which were expelled during the last stages of solidification, or could represent samples of extracted boundary-layer melt. Bimodal distribution of some elements in rock-forming minerals of aplite and microgranite dykes or pegmatite pockets indicates local mixing of melts with distinct degree of evolution.

The role of other mechanisms such as crystal settling or density currents should have been very limited due to the high viscosity of the melt and probably short solidification time, although there are few exceptions and these processes could have acted on local scale. Large solitary megacrysts in a fine-grained matrix adjacent to a coarse-grained zone could be result of crystal motion or settling and some flow fabric like preferred orientation of the tourmaline grains in a massive matrix, cross-bedding structures and dykes of residual melt probably resulted from local flow of the boundary layer melt strongly enriched in boron and other

fluxing components. These fractions of a more mobile melt could flow parallel to the solidification front or be expelled by compaction and crosscut the (semi)solidifed crystal mush. These flow mechanisms, however, do not explain some textural features like unidirectional growth textures. Other possible static mechanisms for the formation of layering (e.g. swinging eutectic producing albite-rich and quartz-rich bands; Jahns and Tuttle, 1963) are unlikely because their variations would not promote over- or undersaturation in tourmaline, and furthermore the intensive variables would have to change too often and suddenly like in a hydrothermal system. The formation of tourmaline by secondary hydrothermal processes appears unlikely, also because their composition (and pleochroic coloration) shows khaki-brown colours typical of magmatic crystallization as opposed to blue-green pleochroism and fine optical zonation found in hydrothermal systems (London and Manning, 1995). The tourmaline in bands is usually euhedral with brown pleochroic colours and appears to be an early-stage phase. The cause of sudden changes in tourmaline chemistry may result from the late-stage appearance of immiscible, boron-rich aqueous fluids or hydrous melts (*cf*. Veksler and Thomas, 2002), which are characterized by low viscosity and tendency to wet mineral surfaces and grain boundaries, hence are also very mobile. The tourmalines with blue pleochroism, anhedral appearance and found mainly in the interstitial space could have formed by this process. The “alteration veins” indicated by blue pleochroism cross-cutting large euhedral tourmalines with overall brown colouration may provide evidence for these late-stage fluids or liquids.

8 Acknowledgements

This master thesis was financially supported by the Czech Science Foundation Project No. P210/12/0986 to David Dolejš and No. P210/11/1168 to Jiří Žák.

I would like to thank my supervisor, David Dolejš, for his advice, useful comments and ideas, and corrections during the two years, when this work has been done. I am grateful to my consultant, Jakub Trubač, for his support during the entire time. I thank Martin Racek for his help at the electron microscope, Helena Klápová for joint optical microscopy work, and Ondřej Šebek for the boron whole-rock geochemistry analyses.

I owe a big thanks to my family, my boyfriend and friends who supported me and with whom I shared a lot of joyful moments, which were the source of strength for me. I am grateful for all the years spent at the Faculty of Science at the Charles University in Prague, which are reflected in this work, and I thank all the people who contributed to these years becoming a valuable, instructive, marvellous and unforgettable part of my life.

9 References

Acosta-Vigil A., London D., Morgan VI G. B., 2005. Contrasting interactions of sodium and potassium with H_2O in haplogranitic liquids and glasses at 200 MPa from hydration-diffusion experiments. Contributions to Mineralogy and Petrology 149, 276-287.

Acosta-Vigil A., London D., Morgan G. B., VI & Dewers T.A., 2006. Dissolution of quartz, albite, and orthoclase in H2O-saturated haplogranitic melt at 800 °C and 200 MPa: diffusive transport properties of granitic melts at crustal anatectic conditions. Journal of Petrology 47, 231-254.

Auzanneau E., Schmidt M. W., Vielzeuf D., Connolly J. A. D., 2010. Titanium in phengite: a geobarometer for high temperature eclogites. Contributions to Mineralogy and Petrology 159, 1-24.

Barbarin B., 1990. Granitoids: main petrogenetic classifications in relation to origin and tectonic setting. Geological Journal 25, 227–238.

Barbey P., 2009. Layering and schlieren in granitoids: A record of interactions between magma emplacement, crystallization and deformation in growing plutons. Geologica Belgica 12, 109-133.

Batchelor R. A. & Bowden P., 1985. Petrogenetic interpretation of granitoid rock series using multicationic parameters. Chemical Geology 48, 43-55.

Behrens H., Nowak M., 2003. Quantification of H_2O speciation in silicate glasses and melts by IR spectroscopy - in situ versus quench techniques. Phase Transitions 76, 45-61.

Benard F., Moutou P., Pichavant M., 1985. Phase relations of tourmaline leucogranites and the significance of tourmaline in silicic magmas. Journal of Geology 93, 271-291.

Botis S. M., Pan Y., Ewing R. C., 2013. Hydrogen incorporation in crystalline zircon: Insight from ab initio calculations. American Mineralogist 98, 745-751.

Brandeis G., Jaupart C., 1987a. The kinetics of nucleation and crystal growth and scaling laws for magmatic crystallization. Contributions to Mineralogy and Petrology 96, 24-34.

Brandeis G., Jaupart C., 1987b. Crystal sizes in intrusions of different sizes: constraints on the cooling regime and crystallization kinetics. In: Mysen B. O. (ed.) Magmatic Processes: Physicochemical Principles, 307-318.

Breiter K., Müller A., Leichmann J., Gabašová A., 2005. Textural and chemical evolution of a fractionated granitic system: the Podlesi stock, Czech Republic. Lithos 80, 323-345.

Burnham C. W., Jahns R. H., 1962. Method for determining the solubility of water in silicate melts. American Journal of Science 260, 721-45.

Chorlton L. B., Martin R. F., 1978. The effect of boron on the granite solidus. Canadian Mineralogist 16, 239-244.

Dingwell D. B., Knoche R., Webb S. L., Pichavant M., 1992. The effects of boron oxide on the viscosity of haplogranitic liquids. American Mineralogist 77, 457-461.

Dolejs D., Baker D. R., 2007. Liquidus equilibria in the system K_2O-Na_2O-Al_2O_3-SiO_2-F_2O_{-1}-H_2O to 100 MPa: II. Differentiation paths of fluorosilicic magmas in hydrous systems. Journal of Petrology 48, 807-828.

Einstein A., 1905. On the movement of small particles suspended in stationary liquids required by the molecular-kinetic theory of heat. Annalen der Physik 17, 549-560.

Ertl A., Marschall H. R., Giester G., Henry D. J., Schertl H. P., Ntaflos T., Luviozotto G. L., Nasdala L. & Tillmanns E., 2010. Metamorphic ultrahigh-pressure tourmaline: Structure, chemistry, and correlations to P-T conditions. American Mineralogist 95, 1-10.

Fenn P. M., 1977. The nucleation and growth of alkali feldspars from hydrous melts. The Canadian Mineralogist 15, 135-161.

Fenn P. M., 1986. On the origin of graphic granite. American Mineralogist 71, 325-330.

Fiala J., Vejnar Z., Kučerová D., 1976. Composition of the biotites and the coexisting biotite-hornblende pairs in granitic rock sof the Central Bohemian Pluton. Krystalinikum 12, 79-111.

Flemmings M. C., 1974. Solidification processing. McGraw-Hill, New York, 273 pgs.

Frindt S., Haapala I., 2004. Anorogenic Gross Spitzkoppe granite stock in central western Namibia: Part II. Structures and textures indicating crystallization from undercooled melt. American Mineralogist 89, 857-866.

Frost B. R., Barnes C. G., Collins W. J., Arculus R. J., Ellis D. J. & Frost C. D., 2001. A geochemical classification for granitic rocks. Journal of Petrology 42, 2033-2048.

Fulcher G. S., 1925. Analysis of recent measurements of the viscosity of glasses. Journal of the American Ceramic Society 8, 339-355.

Furukawa T., Fox K. E., White W. B., 1981. Raman spectroscopic investigation of the structure of silicate glasses. III. Raman intensities and structural units in sodium silicate glasses. Journal of Chemical Physics 153, 3226-3237.

Giordano D., Russell J. K., Dingwell D. B., 2008. Viscosity of magmatic liquids: A model. Earth and Planetary Science Letters 271, 123-134.

Goranson R. W., 1931. The solubility of water in granite magmas. American Journal of Science 22, 481-502.

Harrison T. M. & Watson E. B., 1984. The behavior of apatite during crustal anatexis: equilibrium and kinetic considerations. Geochimica et Cosmochimica Acta 48, 1467-1477.

Henderson C. E., 2011. Protocols and pitfalls of electron microprobe analysis of apatite. M.Sc. thesis, University of Michigan, 68 pgs.

Henry D. J., Novák M., Hawthorne F. C., Ertl A., Dutrow B. L., Uher P., Pezzotta F., 2011. Nomenclature of the tourmaline-supergroup minerals. American Mineralogist 96, 895-913.

Hess K. U., Dingwell D. B., 1996. Viscosities of hydrous leucogranitic melts: a non-Arrhenian model. American Mineralogist 81, 1297-1300.

Holečková H., Šmejkalová M., 1958. Petrochemistry of the Říčany granite (in Czech). Sborník Vysoké školy chemicko-technologické 2, 303-318.

Holtz F., Johannes W., Tamic N., Behrens H., 2001. Maximum and minimum water contents of granitic melts generated in the crust: a reevaluation and implications. Lithos 56, 1-14.

Holub F. V., Cocherie A., Rossi P., 1997a. Radiometric dating of granitic rocks from the Central Bohemian Plutonic Complex (Czech Republic): constraints on the chronology of thermal and tectonic events along the Moldanubian-Barrandian boundary. Comptes Rendus de l'Académie des Sciences - Series IIA - Earth and Planetary Science 325, 19-26.

Holub F. V., Machart J., Manová M., 1997b. The Central Bohemian Plutonic Complex: geology, chemical composition and genetic interpretation. Sborník geologických Věd, Ložisková geologie a mineralogie 31, 27-50.

Hönig S., Leichmann J., Novák M., 2010. Unidirectional solidification textures and garnet layering in Y-enriched garnet-bearing aplite-pegmatites in the Cadomian Brno Batholith, Czech Republic. Journal of Geosciences 55, 113-129.

Hutchison C. S., 1974. Laboratory Handbook of Petrographic Techniques. John Wiley & Sons, New York, 527 pgs.

Hutchison C. S., 1975. The norm, its variations, their calculation and relationships. Schweizer Mineralogische und Petrographische Mitteilungen 55, 243-256.

Jahns R. H., 1982. Internal evolution of pegmatite bodies. Granitic Pegmatites in Science and Industry (P. Černý, ed.). Mineralogical Association of Canada, Short Course Handbook 8, 293-327.

Jahns R. H., Tuttle F. O., 1963. Layered pegmatite-aplite intrusives. Mineralogical Society of America, Special Paper 1, 78-92.

Jakeš P., 1977. Geochemická charakteristika horninových typů středočeského plutonu. Czech Geological Survey Report P117.1977, 16 pgs.

Janoušek V., 1991. Izotopy stroncia v říčanské žule. Diploma thesis, Charles University in Prague, 87 pgs.

Janoušek V., 2006. Saturnin, R language script for application of accessory-mineral saturation models in igneous geochemistry. Geologica Carpathica 57, 131-142.

Janoušek V., Rogers G., Bowes D.R. & Vaňková V., 1995a. The generation and emplacement of the reversely-zoned Ricany granitoid intrusion in the Hercynian Central Bohemian Pluton, Czech Republic. Journal of the Czech Geological Society 40, 68.

Janoušek V., Rogers G., Bowes D.R., 1995b. Sr-Nd isotopic constraints on the petrogenesis of the Central Bohemian Pluton, Czech Republic. Geologische Rundschau 84, 520-534.

Janoušek V., Rogers G., Bowes D.R. & Vaňková V., 1997. Cryptic trace-element variation as an indicator of reverse zoning in a granitic pluton: the Říčany granite, Czech Republic. Journal of the Geological Society, London 154, 807-815.

Janoušek V., Braithwaite C.J.R., Bowes D.R. & Gerdes A., 2004. Magma-mixing in the genesis of Hercynian calc-alkaline granitoids: an integrated petrographic and geochemical study of the Sázava intrusion, Central Bohemian Pluton, Czech Republic. Lithos 78, 67-99.

Janousek V., Farrow C. M., Erban V., 2006. Interpretation of whole-rock geochemical data in igneous geochemistry: introducing Geochemical Data Toolkit (GCDkit). Journal of Petrology 47, 1255-1259.

Kachlík V., 1992. Litostratigraphy, paleogeography and metamorphism of roof pendants in the NE part of the Central Bohemian Pluton. PhD Thesis, Charles University in Prague, 240 pgs.

Kirkpatrick R. J., 1975. Crystal growth from the melt: a review. American Mineralogist 60, 798-814.

Kodym O., 1925. Remarks on the geology of the Říčany granite (in Czech). Věštník Ústředního Ústavu geologického 1, 77-81.

Kubicki J. D., Lasaga A. C., 1987. Molecular dynamics simulation of Mg_2SiO_4 and $MgSiO_3$ melts: Structural and diffusivity changes with pressure. EOS, Transactions American Geophysical Union 68, 436.

Lee S. K., Stebbins J. F., 2003. Nature of cation mixing and ordering in Na-Ca silicate glasses and melts. Journal of Physical Chemistry B 107, 3141-3148.

Lee S. K., Stebbins J. F., Mysen B. O., Cody G. D., 2002. The nature of polymerization in silicate glasses and melts: Solid state NMR, modeling and quantum chemical calculations. EOS, Transactions American Geophysical Union 83, 47.

Levien L., Prewitt C. T., Weidner D. J., 1980. Structure and elastic properties of quartz at high pressure. American Mineralogist 65, 920-930.

Lofgren G. E., Donaldson C. H., 1975. Curved branching crystals and differentiation in comb-layered rocks. Contributions to Mineralogy and Petrology 49, 309-319.

London D., 1999. Stability of tourmaline in peraluminous granite system. The boron cycle from anatextis to hydrothermal aureoles. European Journal of Mineralogy 11, 253-262.

London D., 2005. Granitic pegmatites: an assessment of current concepts and directions for the future. Lithos 80, 281-303.

London D., 2008. Pegmatites. The Canadian Mineralogist, Special Publication 10, 347 pgs.

London D., 2009. The origin of primary textures in granitic pegmatites. Canadian Mineralogist 47, 697-724.

London D., Manning D. A. C., 1995. Chemical variation and significance of tourmaline from southwest England. Economic Geology 90, 495-519.

London D., Morgan G. B., Hervig R. L., 1989. Vapor-undersaturated experiments with Macusani glass + H_2O at 200 MPa, and the internal differentiation of granitic pegmatites. Contributions to Mineralogy and Petrology 102, 1-17.

London D., Černý P., Loomis J. L. & Pan J. J., 1990. Phosphorus in alkali feldspars of rare-element granitic pegmatites. Canadian Mineralogist 28, 771-786.

London D., Morgan G. B., Babb H. A., Loomis J. L., 1993. Behavior and effects of phosphorus in the system $Na_2O–K_2O–Al_2O_3–SiO_2–P_2O_5–H_2O$ at 200 MPa (H_2O). Contributions to Mineralogy and Petrology 113, 450-65.

London D., Morgan G. B., Paul K. A., Guttery B. M., 2012. Internal evolution of miarolitic granitic pegmatites at the Little Three Mine, Ramona, California, USA. Canadian Mineralogist 50, 1025-1054.

Maniar P. D. & Piccoli P. M., 1989. Tectonic discriminations of granitoids. Geological Society of America Bulletin 101, 635-643.

Marsh B. D., 1996. Solidification fronts and magmatic evolution. Mineralogical Magazine 60, 5-40.

Marsh B. D., 2002. On bimodal differentiation by solidification from instability in basaltic magmas, part 1: Basic mechanics. Geochimica et Cosmochimica Acta 66, 2211-2229.

McDonough W. F. and Sun S. S., 1995. The composition of the Earth. Chemical Geology 120, 223-53.

Meagher E. P., Swanson D. K., Gibbs G. V., 1980. The calculation of tetrahedral Si-O and Al-O bridging bond lengths and angles. EOS, Transactions American Geophysical Union 61, 408.

Mielke P. and Winkler H. G. F., 1979. Eine bessere Berechnung der Mesonorm für granitische Gesteine. Neues Jahrbuch für Mineralogie Abhandlungen, Monatshefte, 471-480.

Miller C. F., McDowell S. M. & Mapes R. W., 2003. Hot and cold granites? Implications of zircon saturation temperatures and preservation of inheritance. Geology 31, 529-532.

Montel J. M., 1993. A model for monazite/melt equilibrium and application to the generation of granitic magmas. Chemical Geology 110, 127-146.

Moore G., 2008. Interpreting H_2O and CO_2 contents in melt inclusions: constraints from solubility experiments and modeling. Reviews in Mineralogy & Geochemistry 69, 333-361.

Morgan VI G. B., London D., 1999. Crystallization of the Little Three layered pegmatite-aplite dike, Ramona District, California. Contributions to Mineralogy and Petrology 136, 310-330.

Moulson A. J., Roberts J. P., 1961. Water in silica glass. Transactions of the Faraday Society 57, 1208-1216.

Muncill G. E., Lasaga A. C., 1988. Crystal-growth kinetics of plagioclase in igneous systems: Isothermal H_2O-saturated experiments and extension of a growth model to complex silicate melts. American Mineralogist 73, 982-992.

Mysen B. O., 2002. Water in peralkaline aluminosilicate melts to 2 GPa and 1400°C. Geochimica et Cosmochimica Acta 66, 2915-2928.

Mysen B. O., Richet P., 2005. Silicate glasses and melts, properties and structure. Elsevier, Amsterdam, 544 pgs.

Nabelek P.I., Whittington A.G., Sirbescu M. C., 2010. The role of H_2O in rapid emplacement and crystallization of granite pegmatites: resolving the paradox of large crystals in highly undercooled melts. Contributions to Mineralogy and Petrology 160, 313-325.

Němec D., 1978. Genesis of aplite in the Říčany massif, Central Bohemia. Neues Jahrbuch für Mineralogie Abhandlungen 132, 322-339.

Nesbitt H. W., Young G. M. & Bosman S. A., 2009. Major and trace element geochemistry and genesis of supracrustal rocks of the North Spirit Lake Greenstone belt, NW Ontario, Canada. Precambrian Research 174, 16-34.

Newman S., Stolper S., Epstein S., 1986. Measurements of water in rhyolitic glasses: Calibration of an infrared spectroscopic technique. American Mineralogist 71, 1627-1641.

Nowak M., Behrens H., 1995. The speciation of water in haplogranitic glasses and melts determined by *in-situ* near-infrared spectroscopy. Geochimica et Cosmochimica Acta 59, 3445-3450.

O'Connor J. T., 1965. A classification for quartz-rich igneous rocks based on feldspar ratios. US Geological Survey Professional Paper B525. USGS, 79-84.

Orel P., 1975. Metallogenetic and prognostic consequences of establishing the Říčany–Kutná Hora Batholith (in Czech). Sborník Nerostné surovinové zdroje, vědecká konference – sekce 2: geologie, VŠB Ostrava, 1-118.

Pauling L., 1960. The nature of the chemical bond. Cornell University Press. Ithaca, NY.

Pearce J. A., Harris N. W. & Tindle A. G., 1984. Trace element discrimination diagrams for the tectonic interpretation of granitic rocks. Journal of Petrology 25, 956-983.

Peccerillo A. & Taylor S. R., 1976. Geochemistry of Eocene calc-alkaline volcanic rocks from the Kastamonu area, Northern Turkey. Contributions to Mineralogy and Petrology 58, 63-81.

Pesquera A., Torres-Ruiz J., García-Casco A. and Gil-Crespo P. P., 2013. Evaluating the controls on tourmaline formation in granitic systems: a case study on peraluminous

granites from the Central Iberian Zone (CIZ), western Spain. Journal of Petrology 54, 609-634.

Pichavant M., 1987. Effects of boron and water on liquidus phase relations in the haplogranite system at 1 kbar. American Mineralogist 72, 1056-1070.

Pichavant M., Montel J. M. & Richard L. R., 1992. Apatite solubility in peraluminous liquids: experimental data and extension of the Harrison-Watson model. Geochimica et Cosmochimica Acta 56, 3855-3861.

Raith J. G., Riemer-Schöner N., Meisel T., 2004. Boron metasomatism and behaviour of rare earth elements during formation of tourmaline rocks in the eastern Arunta Inlier, central Australia. Contributions to Mineralogy and Petrology 147, 91-109.

Romano C., Dingwell D. B., Hess K. U., 1995. The effect of boron on the speciation of water in granitic melts. Periodico di Mineralogia 64, 413-431.

Ross N. L., Meagher E. P., 1984. A molecular orbital study of $H_6Si_2O_7$ under simulated compression. American Mineralogist 69, 1145-1149.

Rudnick R. L., & Gao S., 2003. Composition of the continental crust. Treatise on geochemistry 3, 1-64.

Scaillet B., Pichavant M., Roux J., 1995. Experimental crystallization of leucogranite magmas. Journal of Petrology 36, 663-705.

Scholze H., 1956. Der Einbau des Wassers in Glasern. 4th International Congress on Glass, 424-429.

Seifert F. A., Mysen B. O., Virgo D., 1983. Raman study of densified vitreous silica. Physics and Chemistry of Glasses 24, 141-145.

Shand S. J., 1943. Eruptive rocks: Their genesis, composition, classification, and their relation to ore-deposits with a chapter on meteorite. John Wiley & Sons, New York, 444 pgs.

Silver L., Ihinger P. D., Stolper E., 1990. The influence of bulk composition on the speciation of water in silicate glasses. Contributions to mineralogy and petrology 104, 142-162.

Smyth J. R., Bish D. L., 1988. Crystal structures and cation sites of the rock-forming minerals. Allen & Unwin, London, 332 pgs.

Soules T. F., 1979. A molecular dynamics calculation of the structure of sodium silicate glasses. Journal of Chemical Physics 71, 4570-4578.

Stolper E., 1982. The speciation of water in silicate melts. Geochimica et Cosmochimica Acta 46, 2609-2620.

Streckeisen A. & Le Maitre R. W., 1979. A chemical approximation to the modal QAPF classification of the igneous rocks. Neues Jahrbuch für Mineralogie, Abhandlungen 136, 169-206.

Swanson S. E., 1977. Relation of nucleation and crystal-growth rate to the development of granitic textures. American Mineralogist 62, 966-978.

Swanson S. E., Fenn P. M., 1986. Quartz crystallization in igneous rocks. American Mineralogist 71, 331-342.

Šmejkalová M., 1960. Petrochemistry of the Jevany granite (in Czech). Sborník Vysoké školy chemicko-technologické 4 I, 383-390.

Thomas R., Förster H. J., Heinrich W., 2003. The behaviour of boron in a peraluminous granite-pegmatite systém and associated hydrothermal solutions: a melt and fluid-inclusion study. Contributions to mineralogy and petrology 144, 457-472.

Tomek Č., 1974. The inverse gravimetric task and its application on morphology of the Central Bohemian Pluton. Časopis pro mineralogii a geologii 19, 217.

Tomlinson J. W., 1956. A note on the solubility of water in molten sodium silicate. Journal of the Society of Glass Technology 4, 25T-31T.

Trubač J., 2008. Magnetická stavba říčanského granitu: záznam helikoidálního magmatického toku? Diploma Thesis, Charles University in Prague, 85 pgs.

Trubač J., Žák J., Chlupáčová M., Janoušek V., 2009. Magnetic fabric of the Říčany granite, Bohemian Massif: A record of helical magma flow? Journal of Volcanology and Geothermal Research 181, 25-34.

Tuttle O. F., Bowen N. L., 1958. Origin of granite in the light of experimental studies in the system $NaAlSi_3O_8$- $KAlSi_3O_8$-SiO_2-H_2O. Geological Society of America Memoir 74, 153 pgs.

Vejnar Z., 1973. Petrochemistry of the Central Bohemian Pluton. Věštník Ústředního Ústavu geologického 49, 159-165.

Veksler I. V., Thomas R., 2002. An experimental study of B-, P- and F-rich synthetic granite pegmatite at 0.1 and 0.2 GPa. Contributions to mineralogy and petrology 143, 673-683.

Villaseca C., Barbero L., Herreros V., 1998. A re-examination of the typology of peraluminous granite types in intracontinental orogenic belts. Transactions of the Royal Society of Edinburgh: Earth Sciences 89, 113-119.

Vogel D. H., 1921. Temperaturabhängigkeitsgesetz der Viskosität von Flüssigkeiten. Physikalische Zeitschrift 22, 645-646.

Watson E. B. & Harrison T. M., 1983. Zircon saturation revisited: temperature and composition effects in a variety of crustal magma types. Earth and Planetary Science Letters 64, 295-304.

Webber K. L., Falster A. U., Simmons W. B., Foord E. E., 1997. The role of diffusion-controlled oscillatory nucleation in the formation of line rock in pegmatite-aplite dikes. Journal of Petrology 38, 1777-1791.

Webber K. L., Simmons W. B., Falster A. U., Foord E. E., 1999. Cooling rates and crystallization dynamics of shallow level pegmatite-aplite dikes, San Diego County, California. American Mineralogist 84, 708-717.

Whalen J. B., Currie K. L. & Chappell B. W., 1987. A-type granites: geochemical characteristics, discrimination and petrogenesis. Contributions to mineralogy and petrology 95, 407-419.

Whittington A. G., Bouhifd M. A., Richet P., 2009. The viscosity of hydrous $NaAlSi_3O_8$ and granitic melts: configurational entropy models. American Mineralogist 94, 1-16.

Wolf M. B., London D., 1997. Boron in granitic magmas: stability of tourmaline in equilibrium with biotite and cordierite. Contributions to Mineralogy and Petrology 130, 12-30.

Zhang L., Jahanshahi S., 1998. Review and modeling of viscosity of silicate melts: part I. viscosity of binary and ternary silicates containing CaO, MgO, and MnO. Metallurgical and Materials Transactions 29B, 177-186.

Zhang Y., Xu Z., Zhu M., Wang H., 2007. Silicate melt properties and volcanic eruptions. Reviews of Geophysics 45, 216-235.